
**Understanding the life of evolved stars
using modern astronomical tools and
techniques**

**Case study of pulsating GW Vir, hot subdwarf B
stars and their progenitors**

MURAT UZUNDAG

Instituto de Física y Astronomía
Facultad de Ciencias



Universidad de Valparaíso
Doctorado en Astrofísica

August 2022
Valparaíso, Chile

Thesis Committee

Maja Vučković

supervisor

Instituto de Física y Astronomía,
Universidad de Valparaíso

Matías I. Jones

co-supervisor

European Southern Observatory

Claus Tappert

Instituto de Física y Astronomía,
Universidad de Valparaíso

Alejandro H. Córscico

Facultad de Ciencias Astronómicas y Geofísicas,
Universidad Nacional de La Plata

Declaration

I, Murat Uzundag, declare that this thesis titled, "Understanding the life of evolved stars using modern astronomical tools and techniques: Case study of pulsating GW Vir, hot subdwarf B stars and their progenitors" and the work presented in it are my own.

I confirm that:

- This work was done wholly or mainly while in candidature for a research degree at this University.
- Where any part of this thesis has previously been submitted for a degree or any other qualification at this University or any other institution, this has been clearly stated.
- Where I have consulted the published work of others, this is always clearly attributed.
- Where I have quoted from the work of others, the source is always given. With the exception of such quotations, this thesis is entirely my own work.
- I have acknowledged all main sources of help.
- Where the thesis is based on work done by myself jointly with others, I have made clear exactly what was done by others and what I have contributed myself.

Murat Uzundag
August 2022
Valparaíso, Chile

Acknowledgements

These four years have been filled with immense experiences, both as part of my research and with friends, and many people have helped to make this a truly unique and wonderful journey. I have had a lot of company and guidance on this journey, and they have all helped to make it successful and truly memorable. I want to express my gratitude to these people.

First and foremost, I want to thank my thesis supervisor Maja Vučković, without whom this journey would never have taken place and this thesis would not have been possible without her guidance. Thank you not only for giving me the opportunity to explore and grow as a scientist, but also for teaching me how to be well prepared for unexpected life events. Your advice assisted me in sharpening my point as well as presenting and defending my ideas. Thank you for your guidance in many aspects and preparing me for the life of an independent researcher.

I would like to thank my co-supervisors, Matias Jones and Claudia Paladini, for their encouragement to pursue a studentship at ESO. I would like to thank Matias in particular, who has always been supportive of my ideas and plans. Additionally, I want to thank the entire ESO crew for their enthusiasm for science, particularly during the COVID pandemic.

I would like to thank Claus for taking the time to teach me stellar spectroscopy. Without his assistance, it would be impossible to reduce and enjoy a massive amount of data from various instruments. The crew at The Institute of Physics and Astronomy (IFA), particularly Edo, Michel, Jara, Veronica, Patricia, Rudi, Cristian, Javier, Nico, Alex, Rosa, Mohsen, Mona, Elena, Ana, Larissa, Daniela, and Catalina, are also to be thanked for their help and spontaneous Spanish lessons. Muchas gracias!

Alejandro, I appreciate your time and detailed comments on my paper drafts,

which stimulated my curiosity in working on pulsating white dwarfs. I am grateful for his introduction to the field, as well as his thoughts and advice as we attempted to interpret several exotic objects. Above all, I am grateful for the opportunity to learn from his philosophy and approach to science. Thank you so much for your excellent review articles, which have inspired me to improve my writing skills.

I am also very thankful for the work and assistance of my other colleagues in Instituto de Astrofísica de La Plata in Argentina: Marcelo, Leandro, Fran, Tiara and Leila. They have been great company and scientists, broadening my horizons in stellar astrophysics. During my time in La Plata I have grown scientifically, and I have you to thank for that. It has been a pleasure working with all of you. I hope to visit you in La Plata in future and share a matecito while discussing your amazing ideas.

I would also like to thank Roberto, who supervised my internship at the Osservatorio Astrofisico di Torino. I want to thank him for being such an excellent mentor and role model. Furthermore, I would like to thank Andy and Özgür for supervising my master theses during my time in Krakow and Ankara. Thank you for your encouragement and for inspiring me to pursue a PhD.

All of the data presented in this dissertation comes from several Telescopes located in Chile, the NTT, DuPont, SOAR and VLT. I am particularly thankful to the telescope operators, day crew, and staff for their work and assistance through many nights of observing. Moreover, I would like to thank the TESS Asteroseismic Science Consortium, TASOC, for providing a great opportunity to work with such a great data.

To the members of my jury, thank you for providing me with constructive comments and suggestions to improve this manuscript.

To all the passionate scientists I have spoken with or have worked with, thank you. To all those other people I have met during my journey, thank you for making it together.

Formé una segunda familia durante mis viajes por Sudamérica y quiero expresar mi agradecimiento a Juan, Cris, Cami, Simon y Viki por su amabilidad y cálida bienvenida.

Her zaman yanımda olan ve beni destekleyen aileme (Fatma, Eyyüp, Dilek ve Süleyman) en içten dileklerle teşekkür ederim.

Last but not least, many thanks to my wife Mariana for always being there. Your love has aided in the completion of this work.

Sunday August 7, 2022, Valparaíso
Murat Uzundag

Abstract

With the advance of high precision and high duty cycle photometric monitoring from the Transiting Exoplanet Survey Satellite (TESS) mission, unprecedented asteroseismic measurements and tools have become available for pulsating hot subdwarf B (sdB), white dwarf (WD) and pre-white dwarf stars. In this thesis, we present a detailed asteroseismic and spectroscopic analysis of long-period pulsating sdB and GW Vir WD stars observed with TESS in order to compare the observations with model predictions based on stellar evolution computations coupled with adiabatic pulsation computations.

A small percentage of the sdB population (about 10%) was discovered to be pulsating, allowing us to provide observational constraints for stellar models. Pulsating long-period sdB stars constitute a well-established class of variable stars that exhibit brightness variations with periods of up to a few hours and have amplitudes smaller than 0.1 percent of their mean brightness. The oscillation frequencies are associated with low degree ($l < 3$) medium to high-order ($10 < n < 60$) gravity(g)-modes, allowing us to investigate the deep interior of these stars. SdB asteroseismology has undergone substantial progress, thanks to the availability of space missions such as Kepler/K2 and TESS. We applied standard seismic tools for mode identification, including asymptotic period spacings and rotational frequency multiplets. For the dipole ($l = 1$) and quadrupole ($l = 2$) modes, we looked for a constant period spacing based on the results of the Kolmogorov-Smirnov and Inverse Variance tests. We computed stellar evolution models using the LPCODE stellar evolution code and computed dipole g-mode frequencies with the adiabatic nonradial pulsation code LP-PUL. Derived observational mean period spacings were then compared to the mean period spacings from detailed stellar evolution computations coupled with the adia-

batic pulsation computations of g-modes. We find that the mean period spacings obtained for models with small convective cores, as predicted by a pure Schwarzschild criterion, are incompatible with the observations. The models with a standard, modest convective boundary mixing at the boundary of the convective core are in better agreement with the observed mean period spacings and are therefore more realistic.

In the second and third part of the thesis, we aimed at searching for the hydrogen(H)-deficient pulsating pre-white dwarf stars called GW Vir stars that exhibit atmospheres rich in carbon, oxygen and helium. We processed and analyzed the high-precision TESS photometric light curves of the four target stars, and derived their oscillation frequencies. For each of these TESS targets, we obtained low-resolution spectra and fitted model atmospheres in order to derive their fundamental atmospheric parameters. We performed an asteroseismological analysis of these stars on the basis of GW Vir white dwarf evolutionary models that take into account the complete evolution of the progenitor stars. We searched for patterns of uniform period spacings in order to constrain the stellar mass of the stars, and employed a detailed model by best-matching all the observed frequencies with those computed from models. Using the high-quality data collected by the TESS space mission and follow-up spectroscopy, we discovered and characterized four new GW Vir stars.

In the final part, we focused on the volume limited sample of low mass red giant stars, the progenitor systems of wide orbit hot sdB + main sequence (MS) binaries that are the product of a stable roche-lobe-overflow mechanism. With a homogeneously created list from *Gaia*, we aim at performing a spectroscopic survey to find binary systems that include low-mass red giants near the tip of the Red Giant Branch, which are predicted to be the direct progenitors of hot subdwarf B stars. We obtained high-resolution spectra for 88 stars out of which 38 stars were observed in two epochs in order to determine the binary fraction. Combining these measurements with DR2 radial velocity and astrometric excess noise from early Data Release 3 (eDR3), we found 41 binary candidates. We presented 33 low-mass red giant stars that are in binary systems with orbital period between 100 and 900 days from both the ground base surveys and *Gaia* Data Release 3 (DR3). Using high-quality astrometric measurements provided by the *Gaia* mission coupled with high-resolution spectroscopy from the ground, we provided a powerful method to search for low-mass red giant stars in binary systems.

Contents

1	Introduction	1
1.1	Low-to-intermediate mass stars evolution in a nutshell	2
1.1.1	Evolution of low-to-intermediate mass stars	2
1.2	Subdwarf B stars	4
1.2.1	General properties of subdwarf B stars	4
1.2.2	Formation and evolution of sdB stars	5
1.2.3	The progenitors of wide binary hot subdwarf B stars	7
1.3	Asteroseismology of evolved compact stars	9
1.3.1	Pulsating hot subdwarf B stars	10
1.3.2	Pulsating white dwarfs	13
1.3.3	GW Vir type pulsating white dwarfs	14
1.4	Data used in this thesis	14
1.4.1	Space based data	14
1.4.2	Ground based data	16
1.5	Outline of this thesis	18
2	Pulsating hot subdwarf B stars	21
2.1	Introduction	22
2.2	Observations	25
2.2.1	Photometric observations — TESS	25
2.2.2	Spectroscopic observations	26
2.2.3	The targets	27
2.3	Analysis of TESS data	29
2.3.1	Frequency analysis	30
2.3.2	Rotational multiplets	38
2.3.3	Frequency and amplitude variations	40
2.3.4	Asymptotic g-mode period spacing	42

CONTENTS

2.4	Analysis of spectroscopic data	54
2.5	Spectral analysis with XTGRID	56
2.6	Asteroseismic models	57
2.7	Summary and conclusions	60
3	Pulsating hydrogen-deficient white dwarfs: Discovery of two new GW Vir stars TIC333432673 and TIC095332541	63
3.1	Introduction	64
3.2	Spectroscopy	65
3.3	Spectral fitting	66
3.4	Photometric observations — TESS	67
3.5	Asteroseismology	74
3.5.1	Spectroscopic mass	74
3.5.2	Mean period spacing of TIC 333432673	75
3.5.3	Period-to-period fits for TIC 333432673	79
3.5.4	The asteroseismological distance of TIC 333432673	83
3.5.5	Mean period spacing of TIC 095332541	84
3.5.6	Period-to-period fits for TIC 095332541	86
3.6	Summary and conclusions	89
4	Pulsating hydrogen-deficient white dwarfs: Discovery of two new GW Vir stars TIC0403800675 and TIC1989122424	91
4.1	Introduction	92
4.2	Spectroscopy	93
4.3	Spectral fitting	94
4.4	SED fitting	95
4.5	Photometric observations — TESS	98
4.5.1	Frequency solution	101
4.6	Conclusions	102
5	Volume limited sample of low mass red giant stars, the progenitors of hot subdwarf stars	105
5.1	Introduction	106
5.2	Target selection	108

5.2.1	Spectroscopic binaries from the literature	109
5.2.2	Binaries from DR3	109
5.3	Observations and data reduction	109
5.3.1	ESO archival data	112
5.4	Classification Method	112
5.4.1	Astrometric excess noise	112
5.4.2	The Renormalised Unit Weight Error (RUWE)	113
5.4.3	Radial velocities from CORALIE, FEROS, DR2 and DR3	113
5.4.4	Classification	114
5.5	Conclusion	115
6	Conclusions and future prospects	119
6.1	Summary and conclusions	119
6.2	Future prospects	121
A	Radial velocity measurements	123
B	Publication list	143

During various stages of their evolution, stars cross at least one phase of pulsational instability that converts them into variable stars. Stellar oscillations travel through the stellar interiors and carry with them information about the internal structure of the star, which can then be studied by observing the changes in the surface brightness of the stars. The interpretation of detected stellar oscillations, known as asteroseismology, provides a unique way to probe and calibrate stellar interiors. By comparing observational data to theoretical stellar model predictions, we can fine-tune the physical descriptions used for these models. Thanks to the advance of high precision and high duty cycle photometric monitoring from space, unprecedented asteroseismic measurements and tools have become available especially for pulsating stars that are in late-stage of stellar evolution.

Another important aspect of the final evolution of stars is the impact of binarity since a high percentage of stars reside in binary systems. Stars are mostly found in binary and multiple systems: at least half of all solar-like stars have companions, and for the most massive stars, that percentage increases up to 80%. A significant number of these systems will interact during their evolution, changing the structure and evolution of the components and resulting in the formation of exotic objects not predicted by standard stellar evolution models. However, some key details concerning binary interactions are still uncertain.

This dissertation describes the observational and theoretical efforts conducted over the last four years with the aim of increasing our knowledge about the late stages of stellar evolution. The stars studied in detail in this thesis are pulsating hot subdwarf B stars (hereafter sdBs) and pulsating hydrogen-deficient white dwarfs (WDs) specifically focusing on GW Vir pulsating stars. Furthermore, this thesis includes work on

the progenitor systems of wide orbit hot sdB + main sequence (MS) binaries that are the product of a stable Roche-lobe-overflow mechanism.

This chapter is organized as follows. In Sect. 1.1 we give a brief overview of how low- and intermediate-mass stars evolve from the main sequence to the white dwarf phase. In Sect. 1.2 we go over the basics of sdBs, including their general properties, formation, and evolution. In Sect. 1.3 we give an overview on asteroseismology of pulsating sdBs and WDs. In Sect. 1.4 we introduce the instruments used to obtain the data that are analysed throughout this thesis. We end this chapter with the general outline of this thesis.

1.1 Low-to-intermediate mass stars evolution in a nutshell

The evolution and fate of a star is inevitably determined by its initial mass. In brief, if the star has an initial low- or intermediate mass, i.e., between approximately $0.8M_{\odot}$ and $8M_{\odot}$, it will evolve until it becomes a white dwarf and eventually cool down. If the star's initial mass is greater than $8M_{\odot}$, it will have a short and hectic life before dying violently in the form of a supernova explosion. We will concentrate on the first group since they will be the subject of this thesis. In this chapter, we will confine ourselves to a brief overview of single-star evolution, focusing on a few key ingredients that are relevant to the research conducted in this thesis. This chapter is based on Althaus et al. (2005a); Herwig (2005); Kippenhahn et al. (2013), and we refer to those reviews for more information on this subject.

1.1.1 Evolution of low-to-intermediate mass stars

After the star forms in a molecular cloud, it will enter in the so-called main-sequence (MS) phase¹, where the star will spend most of its life. The star is in hydrostatic and thermal equilibrium because the gas pressure generated by hydrogen (H) fusion in the centre balances the gravitational pull. The MS phase is the longest and most stable burning stage of stellar evolution. Depending on their mass, the stars spend between 10^6 and 10^9 years in this phase. When all the fuel of H in the core is exhausted and transformed into helium (He), the core begins to contract, since there is no radiation

¹Note that objects with masses between ~ 0.01 and $\sim 0.08 M_{\odot}$ are called brown dwarfs and will never reach the main sequence phase.

pressure to support the gravitational collapse. To maintain thermal equilibrium, the core contracts and the envelope expands.

The phase in which the H fusion moves from the core to a shell is called the sub-giant phase and ends when the star is at the base of the Red Giant Branch (RGB). The transition from the end of the MS to the base of the RGB occurs on a very short time scale. Therefore, the likelihood of observing stars crossing the HR diagram is extremely low, which is why this region is known as the Hertzsprung gap. During the subgiant branch phase, the core slowly increases in mass and contracts further, while the envelope expands, and the H-burning shell gradually becomes thinner. As a consequence of the H-burning in the shell, the core grows in mass, the luminosity also grows and the star climbs up the RGB. During the RGB, mass loss via stellar winds becomes important (Reimers, 1975) since the envelope becomes more loosely bound, and stellar-wind-mass loss increases.

Low-mass stars ($M_{\star} \lesssim 2.25M_{\odot}$) ignite He differently than intermediate-mass stars ($2.25M_{\odot} \lesssim M_{\star} \lesssim 8M_{\odot}$). The He core of low-mass stars ignites under electron-degenerate conditions, resulting in a He core flash. This He core flash produces a luminosity of $10^{11}L_{\odot}$ in a $1M_{\odot}$ -star and a series of secondary flashes follows the He core flash. In the case of intermediate-mass stars with $2.25M_{\odot} \lesssim M_{\star} \lesssim 8M_{\odot}$, they do not have a degenerate core and He ignites quietly at the centre. In the HR diagram, core-He burning stars are located in the so-called horizontal branch (HB) (see Fig. 1.1). At this point, the metal content and the envelope mass of a star have a big impact on its location on the HB. Those with a high metallicity will fall into the "red clump" (RC), which is close to the RGB. When He is exhausted in the core, He fusion moves to a shell and the star will not have the required gravitational energy to trigger the fusion of carbon (C) and oxygen (O) in the core. As in the RGB phase, the contraction of the core causes the outer layers to expand, lowering the effective temperature and increasing the radius and luminosity of the star. The star moves upwards in the HR-diagram along the Asymptotic Giant Branch (AGB) as can be seen in Fig. 1.1. At this stage, the structure of the star consists (from the nucleus outwards) of an inert CO core, a He-burning concentric shell, an inert He layer, a H-burning shell, and finally, an outer H convective envelope. The AGB phase can be divided into two phases: the early-AGB (E-AGB) phase and the thermally-pulsing AGB (TP-AGB) phase. During the E-AGB phase, the H-burning shell is inactive, leaving the He-burning shell as the only energy source in the star. When the burning shells become thin enough, the star enters the TP-AGB phase, where the H and He shells intermittently burn, mixing material from

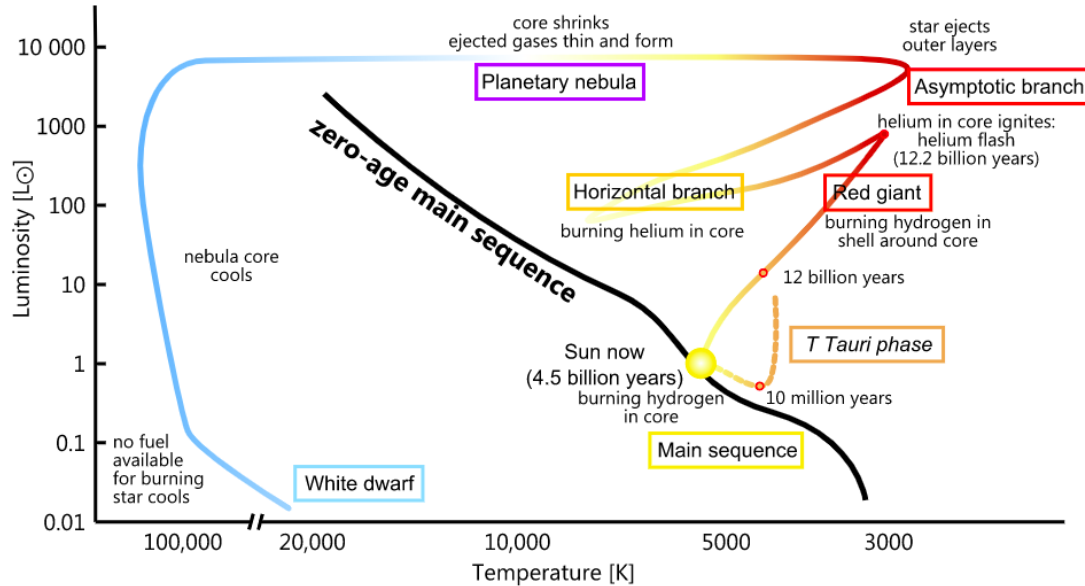


Figure 1.1: Hertzsprung-Russell diagram showing the evolution of a star with an initial mass of one solar mass (M_{\odot}). Credits: <https://www.cpp.edu/~pbsiegel/phy303/ch13.html>

the shells into the convective envelope.

As the star ascends the AGB, it develops a stellar wind outside its envelope, blowing the outer layers into space. This wind, when combined with strong thermal pulses, can cause mass loss of up to $10^{-4}M_{\odot} \text{ yr}^{-1}$. The envelope is removed after about 10,000 years, leaving only a hot degenerate CO core, which is nothing other than a CO white dwarf (WD), surrounded by the planetary nebula. This WD radiates energy and cools on the WD cooling track.

1.2 Subdwarf B stars

1.2.1 General properties of subdwarf B stars

Searching for subdwarf B (sdB) stars started nearly seventy years ago. The first sdB star was discovered by Humason & Zwicky (1947) who were looking for faint blue objects in the region of the North Galactic Pole and of the Hyades Cluster. Luyten (1953) listed 70 blue faint objects including the first discovery. The spectra of the stars in that list showed chemical abundance anomalies, hence they classified them as chemically peculiar stars. Since then many photometric surveys have been conducted by numerous observatories to search for these faint objects. Feige (1958) established a

catalogue including 114 faint blue stars in galactic polar regions as galactic halo stars. The magnitudes of these stars were brighter than 14 mag and they had relatively large radial velocities. Furthermore, he tried to classify the stars in terms of their spectral type as sdO and sdB (see table 1 Feige, 1958). Since these objects are faint and their magnitudes are low ranging from 11 to 17 mag, it is hard to identify subluminescent stars. The Palomar-Green survey (PG; Green et al., 1986) provided a more complete picture than had previously been obtained. The objects were well-separated according to their spectral types. During the survey, the authors catalogued 1874 objects in the northern Galactic hemisphere. With the improvements in telescopes and detector technology, more advanced surveys have been organized (e.g., Hagen et al., 1995; Wisotzki et al., 1996; Stobie et al., 1997; Mickaelian et al., 2007) and Østensen (2006) compiled a database including more than 2300 entries. In the following years, significant new discoveries of hot subdwarfs have been made, and quantitative spectroscopic analyses of large samples have been carried out as part of ongoing spectroscopic surveys such as SDSS (Kepler et al., 2019a) and LAMOST (Lei et al., 2018, 2019). The publication of Gaia Data Release 2 (DR2) was a major turning point for the identification of hot subdwarfs. By using colors, parallaxes, and proper motions from Gaia DR2 and several ground-based, multi-band photometry surveys, Geier et al. (2017) compiled a hot subdwarf star catalogue. The catalogue contains 39800 candidate sources and has a magnitude limit of $G < 19$ mag and it covers the entire sky with the exception of the Galactic plane and the direction of the Large and Small Magellanic Clouds (LMC/SMC). The catalogue is fairly complete up to 1.5 kpc, with only about 10% contamination from cooler stars (Geier et al., 2019). More recently, thanks to arrival of Gaia eDR3, Culpan et al. (2022) updated the DR2 catalogue of hot subluminescent stars using the improved accuracy of the Gaia EDR3 data set together with updated quality and selection criteria to produce the Gaia EDR3 catalogue of 61585 hot subluminescent candidates.

1.2.2 Formation and evolution of sdB stars

Hot subluminescent stars of spectral type B (sdB) have been identified as core helium-burning stars (Heber, 2016). They are located between the Horizontal Branch (HB) and white dwarf cooling track, on a narrow path on the so-called the Extreme Horizontal Branch (EHB, Heber, 2016). The location of hot subdwarfs on the Hertzsprung-Russell diagram is shown in Fig. 1.2. Their effective temperatures are spanning from 20,000

to 40,000 K. Their masses are typically around 0.47 solar masses and radii between 0.15 and 0.35 solar radii, making them compact objects. These stars are He-burning cores, which are surrounded by thin hydrogen envelopes ($M_{envelope} < 0.01M_{\odot}$). Such small mass of the hydrogen envelope does not allow sdB stars to climb up the Asymptotic Giant Branch (AGB). Therefore, after helium depletion in the core, sdB stars will evolve into subdwarf O (sdO) stars that burn helium in a shell surrounding the C/O core. Soon after, they move directly to the white dwarf cooling tracks.

Because the progenitor of sdBs must lose its entire hydrogen envelope before starting core helium fusion, their existence complicates stellar evolutionary theory. Previous research based on small and biased samples revealed that a high percentage of sdBs, ranging from 40 to 70% reside in binary systems (Maxted et al., 2001; Copperwheat et al., 2011a) and the current consensus is that sdB stars are formed solely by binary interaction (e.g. Han et al., 2002, 2003; Pelisoli et al., 2020).

Three main binary evolution scenarios have been described in detail by Han et al. (2002, 2003) as formation channels for sdB stars:

(i) common envelope ejection (CEE) (Paczynski, 1976), resulting in short-period binaries with periods ranging from 0.1 to 10 days, as well as an sdB star with a very thin hydrogen envelope and a mass distribution that sharply peaks at $0.46M_{\odot}$. The subchannels are referred to as the first CE ejection channel and the second CE ejection channel, depending on whether the secondary is a main-sequence star or a white dwarf.

(ii) stable Roche lobe overflow (RLOF) (Han et al., 2002), producing binaries composed of an sdB and a MS star, with orbital periods of up to 1600 days (Chen et al., 2013; Vos et al., 2019). This channel produces sdBs with similar masses as in CEE, but with a rather thick H-rich envelope.

(iii) double helium-rich atmosphere white dwarf merger channel (Webbink, 1984; Zhang & Jeffery, 2012), resulting in single sdB stars with a wider mass distribution.

More evidence for various types of merger formation channels has recently been discovered. For instance, Vos et al. (2021) discovered a hydrogen-rich sdB star surrounded by a gas disc indicative of a young merger product, while Dorsch et al. (2022) presented a magnetic He-sdO consistent with the predictions of the He-WD merger channel. Most recently, Werner et al. (2022) discovered a new class of helium-rich sdOs with extreme carbon and oxygen enrichments, which they explain as the result of the merger of CO and He-WDs (Miller Bertolami et al., 2022).

Other viable binary channels are proposed in addition to the double white dwarf

merger channel. For instance, a low mass star or brown dwarf may merge with a red-giant core to form an sdB star (Soker, 1998; Politano et al., 2008).

Alternative formation scenarios based on the evolution of a single star have also been proposed. Without any binary interactions, hot subdwarf stars could form by mixing processes within a single star. For instance, strong stellar wind mass loss during the RGB phase has been proposed by D’Cruz et al. (1996) as a reason for some objects being placed on the EHB. Internal processes may reduce the hydrogen content of the envelope, for example, by delaying the helium core flash (the so-called hot-flasher scenario) (Sweigart, 1997; Miller Bertolami et al., 2008), during which surface hydrogen is burned after mixing into deeper layers, resulting in hot subdwarf stars. These theories could explain how single hot subdwarf stars formed, and a summary of them can be found in the review of Heber (2016).

While the past evolution of sdB stars is unknown, the future evolution of these stars is assumed to be straightforward. Hot subdwarf B stars will not go through the Asymptotic Giant Branch and Planetary Nebula phases because the hydrogen envelope is too thin to sustain nuclear burning (Dorman & Rood, 1993). They will spend about 10^8 yr burning He in their cores. Once the He has been exhausted in their core, they will start burning He in a shell surrounding a carbon and oxygen (C/O) core as subdwarf O (sdO) stars, and will eventually end their lives as white dwarfs.

1.2.3 The progenitors of wide binary hot subdwarf B stars

Thanks to the data from the Gaia mission it is now possible to select complete all-sky samples of hot subdwarf stars (Geier et al., 2019) and cross-match them with the wealth of spectroscopic data provided in the literature (Geier et al., 2017, 2019). This is the first step towards the compilation of all-sky, volume-complete samples with minimal selection effects, which can be directly compared to quantitative models. Currently, the volume-limited spectroscopic survey of all sdBs within 500 pc has been completed (Dawson et al., in prep.).

The orbital periods of the sdB+MS binaries produced by the stable RLOF channel range from 500 days to more than 1600 days (e.g. Vos et al., 2019). Long-term observational campaigns have been conducted in an effort to find these systems over the past few decades and the orbital parameters of 26 systems for stable RLOF sdB binaries with periods between 500 and 1500 days have recently been solved. (Vos et al., 2019; Otani et al., 2021; Németh et al., 2021; Molina et al., 2021). These systems are

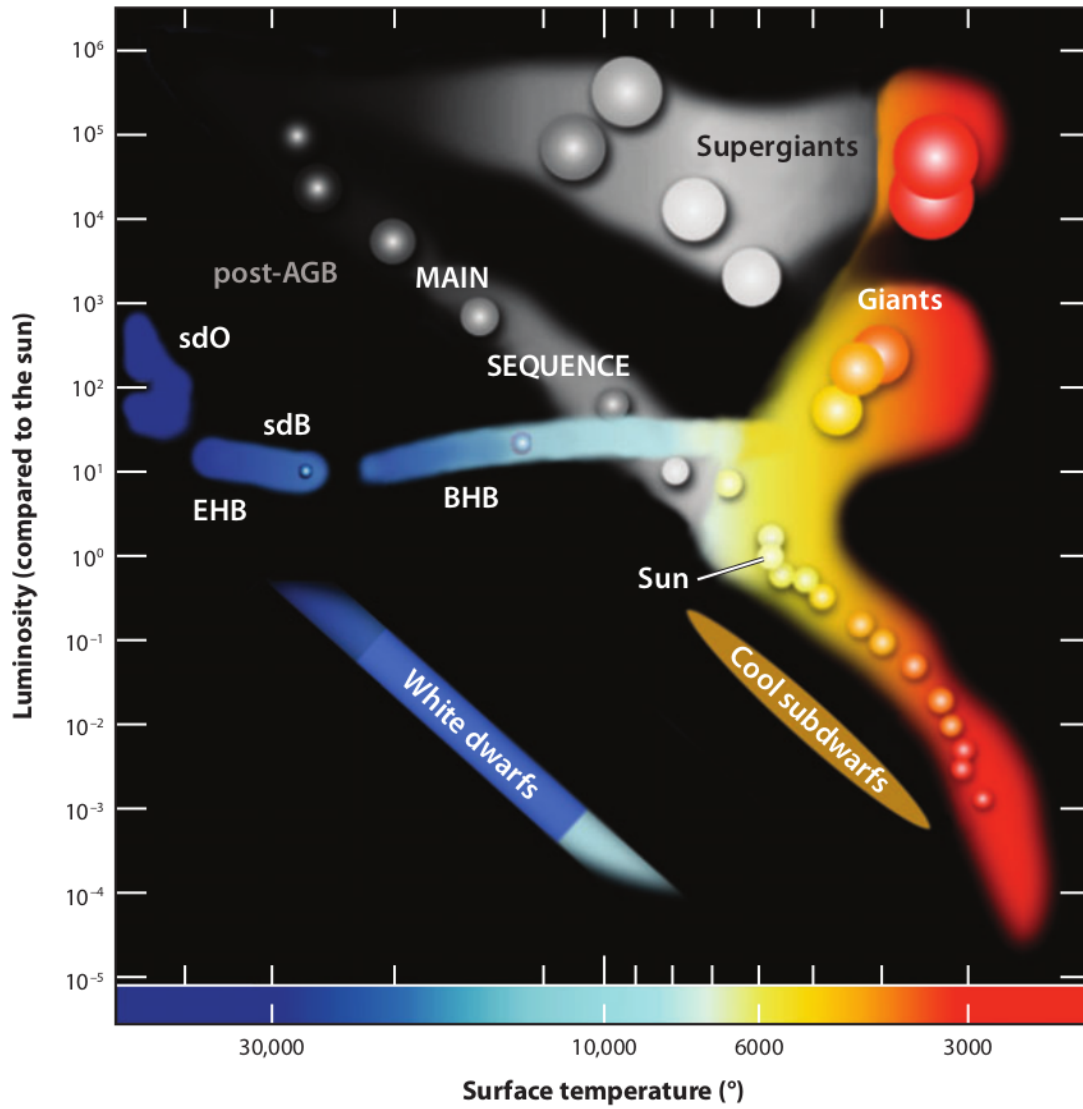


Figure 1.2: Hertzsprung-Russell diagram showing the location of the hot subdwarf stars (sdB and sdO) at the extreme end (EHB) of the blue-horizontal branch (BHB). Figure courtesy of Heber (2016).

referred to as “composite” binaries since both stars can be seen in the spectrum, and they account for 30-40% of all sdBs.

In this thesis, we aim at compiling a homogeneous volume limited sample of pre (low-mass RGB + MS) and post (sdB + MS) RLOF interaction systems that will enable us to constrain the physics of stable mass transfer and will give the observational evidence for correlation between the key parameters governing the formation of hot sdB stars. We are interested in the initial condition of the progenitor population of sdB stars (before they have started binary interactions), we focus on the lower luminosity RGBs as those stars are clearly the H-shell burning around an inert He-core and have not yet undergone binary interaction. We assembled a sample of low-mass red giant candidates using data from the *Gaia* mission and several ground-based spectroscopic surveys. The candidates were chosen based on the color, absolute magnitude, and proper motion cuts of their *Gaia* DR2. In order to find RGB + MS binary systems within 200 pc, we focused on targets in the southern hemisphere and performed a spectroscopic survey of 88 red giant stars (Chapter 5).

1.3 Asteroseismology of evolved compact stars

Compact pulsating stars show brightness fluctuations with periods in the range of $\sim 100 - 14\,000$ s for sdBs (Østensen, 2010; Lynas-Gray, 2021) and $\sim 100 - 7\,000$ s for WDs (Córscico et al., 2019). The typical amplitudes for both types can amount to up to 0.4 mag. In order to detect and characterize these small fluctuations, uninterrupted high-cadence time-series photometry is the most suited method. Over the last decade, space missions like Kepler/K2 and now TESS have accumulated a unique data set. Such a data set has greatly improved our knowledge of stellar structure and evolution via the application of asteroseismology.

In pulsating sdBs and WDs, the oscillations are excited by a driving mechanism related to the partial ionization of the dominant chemical species in the driving zone, which is located at the outer regions of these stars (Winget & Kepler, 2008; Althaus et al., 2010a; Córscico et al., 2019; Charpinet et al., 1996; Fontaine et al., 2003). Fig. 1.3 shows the regions of stellar instability across the H-R diagram, with the extreme horizontal branch and white dwarf cooling highlighted as a grey shaded region. As can be seen in Fig. 1.3, pulsations have been discovered in a variety of groups of stars of all masses and across the Hertzsprung-Russell diagram as telescopes and detectors have become more sensitive.

The non-radial oscillations are classified using three quantized numbers n , l and m , representing the radial overtone, the surface degree and azimuthal order, respectively. In order to identify these quantities, there are two commonly used methods called the asymptotic period spacings and rotational multiplets (see Chapter 2). We make use of these seismic methods in order to identify common patterns in the pulsation spectrum in pulsating sdBs and WDs. In the case of GW Vir pulsating stars, the comparison between the asymptotic period spacing computed from a grid of models corresponding to different masses and effective temperatures and the asymptotic period spacing derived from the observations will provide the value of the WDs mass (Córscico et al., 2019). Another way to infer the WDs mass, along with the effective temperature and also many details of the internal structure of pulsating WDs, is through their individual pulsation periods. In this approach, we seek a pulsation WD model that best matches the pulsation periods of the target star (e.g. Córscico et al., 2021b).

In the case of sdBs, the models are not straightforward to derive the masses from the asymptotic period spacing. All current seismic models of sdBs are based on frequency matching (e.g. Van Grootel et al., 2013). Based on TESS observations, (Charpinet et al., 2019) identified the pulsation modes and determined the global parameters and structural configuration of EC 21494-7018, one of the long period sdB pulsators, by best-matching all observed frequencies with those computed from models. The authors derive the total mass, the H-rich envelope mass, radius and luminosity.

When a pulsating star is rotating, the frequencies of non-radial pulsation modes split into $2l + 1$ components, and their separation is proportional to the velocity of rotation of the star. In this way, when a pulsating sdBs and WDs exhibit rotational splitting, it is possible to constrain their rotation period. This method is known as rotational multiplets. It is covered in detail in Chapters 2 and 3.

1.3.1 Pulsating hot subdwarf B stars

Kilkenny et al. (1997) pioneered one of the most significant advances in our understanding of sdB stars when they discovered rapid pulsations in hot sdBs known as V361 Hya stars (often referred to as short-period sdBV stars). Multiperiodic pulsations with periods ranging from 100 to 800 seconds are detected in the V361 Hya stars. The pulsational modes in this region correspond to low-degree, low-order pressure (p)-modes with photometric amplitudes as small as a few percent of their mean

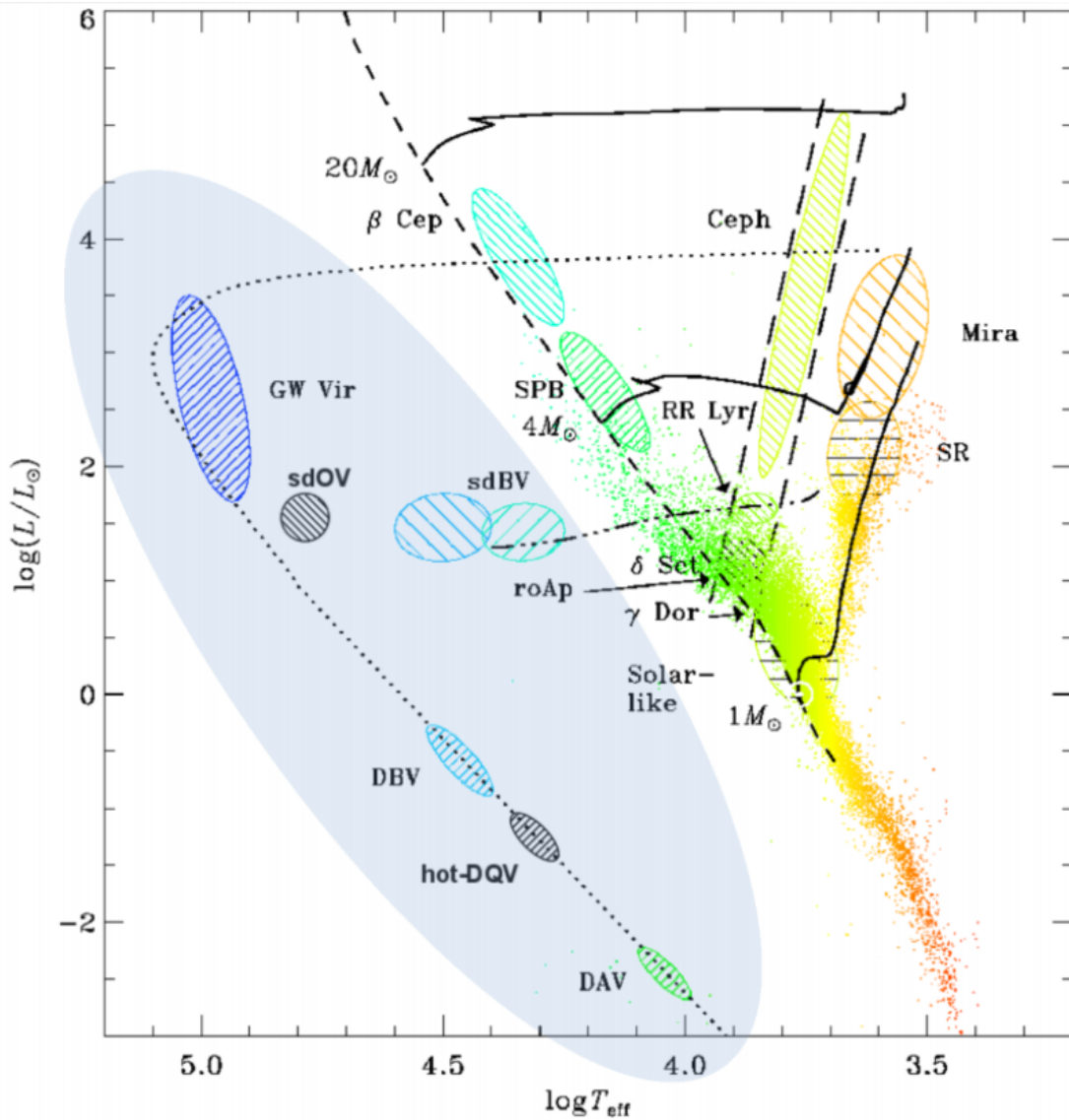


Figure 1.3: Stellar pulsations across the H-R Diagram. The instability regions, where the main classes of pulsating variables are indicated. The shaded region shows the region of compact pulsating stars including hot subdwarf O/B and hydrogen-poor (DOV and DBV) and hydrogen-rich (DAV) pulsating white dwarf stars. Figure taken from <https://tasoc.dk/wg8/?action=download&upname=WG8-session-talk.pdf>

brightness (Østensen, 2010). The p-mode sdB pulsators are found in a temperature range between 28 000 K and 35 000 K and with the surface gravity $\log g$ in the interval of 5-6 dex. The iron group elements (mostly iron itself) accumulating in the Z-bump region cause a classical κ -mechanism to excite the pulsations (Charpinet et al., 1996, 1997; Fontaine et al., 2003). In order to increase the abundances of iron group elements, which are necessary to be able to excite the pulsational modes, the authors also demonstrated that radiative levitation is a crucial physical process.

Green et al. (2003) discovered the long-period sdB pulsators known as V1093 Her stars. These stars show brightness variations with periods of up to a few hours and have amplitudes smaller than 0.1 per cent of their mean brightness (Reed et al., 2011). The oscillation frequencies are associated with low-degree ($l \leq 2$) (Reed et al., 2011) medium- to high-order ($10 < n < 60$) g-modes, which are driven by the same mechanism as in the hotter V361 Hya stars (Fontaine et al., 2003; Charpinet et al., 2011). In few cases, a high-degree modes ($l \leq 8$) were reported based on Kepler and K2 observations (Telting et al., 2012; Silvotti et al., 2019). The g-mode sdB pulsators are somewhat cooler, with temperatures ranging from 22 000 K to 30 000 K and $\log g$ from 5 dex to 5.5 dex.

Some sdB pulsators showing both g- and p-modes have been discovered among the two described families of pulsating sdB stars. These stars are referred to as hybrid sdB pulsating stars with temperatures ranging from 28 000 K to 32 000 K (Green et al., 2011). These objects are especially significant because they allow us to study both the core structure and the outer layers of the sdBVs using asteroseismology.

Space photometry from the Kepler mission (Borucki et al., 2010a) and from the TESS mission (Ricker et al., 2014) has been a major source of new candidates for V1093 Her and V361 Hya classes of variables. The majority of the sdB stars observed by Kepler are V1093 Her variables (16 stars), with one hybrid and two V361 Hya stars (Østensen et al., 2011b; Østensen & Van Winckel, 2012; Reed et al., 2011; Kawaler et al., 2010; Baran et al., 2011). Analysis of data from the extended Kepler K2 mission resulted in the discovery of 15 pulsating sdB variables, two of which belong to the V361 Hya class (Reed et al., 2018). Holdsworth et al. (2017) give a table of 110 pulsating subdwarfs known at the time. Lynas-Gray (2021) provides an excellent review that includes a list of 56 known pulsating sdB stars. More recently, Van Grootel et al. (2021) has presented a list of 1398 sdBs observed by the TESS mission. From that list, Krzesinski & Balona (2022) found in total 63 pulsating hot subdwarfs, out of which 25 are previously unknown pulsating hot subdwarf candidates.

1.3.2 Pulsating white dwarfs

White dwarf (WD) stars are the end evolutionary state of all stars formed with initial masses below around $8M_{\odot}$, which comprise more than 95% of all stars in our galaxy (Althaus et al., 2010a). They play a unique and fundamental role for our understanding of the formation and evolution of stars and planetary systems. An important subset of WDs present photometric variability caused by a range of phenomena, including pulsations, binarity, and more recently transits by both planets and planetary debris. Therefore, studying photometric variations in WDs provides an invaluable source of information concerning the end stages of stars and planets.

In the course of their evolution, WDs cross at least one phase of pulsational instability that converts them into pulsating stars. Stellar pulsations propagate throughout the star and carry with them information about the condition within the deep stellar interior. This information is crucial for fine-tuning models of stars and allows us to test the current theory of WD structure and evolution (Winget & Kepler, 2008; Althaus et al., 2010a; Córscico et al., 2019).

The majority (around 80%) of spectroscopically identified WDs are characterized by Hydrogen(H)-rich (DA) atmospheres (Kepler et al., 2019b). The most populous class of pulsating WDs are DAV or ZZ Ceti stars with $T_{\text{eff}} \sim 10\,500 - 13\,000$ K and $7.5 < \log g < 9.2$. These stars have been studied extensively thanks to Kepler/K2 and TESS observations and recently, the number of known DAVs has been increased to 500 objects (Hermes et al., 2017a; Romero et al., 2022).

The remaining pulsating WDs ($\sim 20\%$), characterized by H-deficient (spectral types of DO, DB, DQ, and DC) atmospheres (Koester & Kepler, 2015), are not as abundant as DA WDs and their evolutionary path is still not completely clear (Córscico et al., 2019). For instance, DBVs might be either a descendent of the GW Vir stars (oxygen/carbon/He-rich atmospheres) after going through the DO WD (very hot He-rich atmospheres) stage, or the result of merger of two WDs. In Fig. 1.3, all known pulsating WDs are depicted including GW Vir stars, DBVs and DAVs. However, the pulsation nature of two types of pulsating WDs, hot DAV and DQV WDs, remains elusive and further observations are needed to confirm the nature of their variability. One of the main issues of H-deficient pulsating WD stars is that the boundaries of the theoretical instability strip are not well established and, in most cases, they do not match with the empirical ones. Therefore, discoveries of new H-deficient pulsating WD stars will also allow testing the theoretical instability strips and the asteroseismic

analysis of these new pulsators will help us to understand of their origin, evolution, and internal structure.

1.3.3 GW Vir type pulsating white dwarfs

GW Vir stars are pulsating PG 1159 stars, that is, pulsating hot hydrogen (H)-deficient, carbon (C)-, oxygen (O)-, helium (He)-rich WD, and pre-WD stars. PG 1159 stars represent the evolutionary link between post-asymptotic giant branch (AGB) stars and most of the H-deficient WDs, including DO and DB WDs (Werner & Herwig, 2006). These stars likely have their origin in a born-again episode induced by a post-AGB He thermal pulse (see Herwig, 2001; Blöcker, 2001; Althaus et al., 2005b; Miller Bertolami et al., 2006, for references). The category of GW Vir stars includes variable central stars of planetary nebulae (PNNV) and DOV stars, which lack a nebulae (Winget et al., 1991), and also the pulsating Wolf-Rayet central stars of planetary nebula ([WC] stars) and Early-[WC] = [WCE] stars, because they share the same pulsation properties of pulsating PG 1159 stars (Quirion et al., 2007). GW Vir stars exhibit multiperiodic luminosity variations with periods in the range of 300–6 000 sec, and they originated from *g*-mode pulsations excited by the κ -mechanism due to partial ionization of C and O in the outer layers (Starrfield et al., 1983, 1984; Stanghellini et al., 1991; Saio, 1996; Gautschy, 1997; Gautschy et al., 2005; Córscico et al., 2006; Quirion et al., 2007).

1.4 Data used in this thesis

The telescope is the most important instrument in nearly all modern observational astronomy. In this thesis, we used optical spectroscopy and photometry obtained with a variety of instruments and telescopes from both ground and space. We made extensive use of spectroscopic data obtained in several observatories in Chile as well as photometric data obtained with the TESS and Gaia space telescopes. The instruments that have been used in this thesis are introduced as below.

1.4.1 Space based data

Transiting Exoplanet Survey Satellite (TESS)

The Transiting Exoplanet Survey Satellite (TESS; Ricker et al., 2014) is a set of four 100-mm aperture cameras mounted on a spacecraft in a lunar-resonance Earth orbit.

Because of the orbit, the pointing of the telescope must be changed roughly every lunar month (~ 27 days). The spatial resolution of TESS is roughly 21 arcseconds per pixel. At effectively 1048×1048 usable pixels on each of the four cameras, the entire system can view $24^\circ \times 96^\circ$. The bandpass of TESS covers a redder part of the electromagnetic spectrum from ~ 6000 to 10000 \AA . The primary goal of TESS is to search for exoplanets around bright and nearby stars via the transit technique (Ricker et al., 2015a). The high cadence (20-seconds or 2-minutes) and high duty cycle observations provided by TESS have been one of the benefits. In addition to short and ultra short cadence observations, TESS delivers a nearly continuous series of full frame images (FFI) with an exposure time of 30 minute. Because a large patch of the sky is sampled at a resolution of 30 minutes in FFI mode, it provides a significant source of time series data. Recently, using FFI data, several new sdB pulsators, eclipsing binaries (detached and semidetached), non-eclipsing binaries, novae and HW Vir types of variables have been reported by Sahoo et al. (2020b); Baran et al. (2021).

The TESS Asteroseismic Science Consortium (TASC) is an international group of scientists who are interested in using TESS data for asteroseimology research. It is divided into several working groups that deal with different types of stars. TESS observations of evolved compact stars with photometric variability, such as hot subdwarfs, white dwarf stars, and pre-white dwarfs, are the focus of the TASC Working Group 8 (WG8). WG8 has proposed that all known and likely compact stars with TESS magnitudes of brighter than $\lesssim 17$ be observed with 20-seconds or 2-minute cadences.

This thesis mainly focused on analyzing the compact pulsators including sdB (see Chapter 2) and WD stars (see Chapters 3 and 4) based on short and ultra-short-cadence observations obtained with TESS.

Gaia

The Gaia satellite was successfully launched at the end of 2013 and started taking scientific data in mid-2014 as an astrophysical space mission of the European Space Agency (Gaia Collaboration et al., 2016a). Its primary scientific goal is to create precise 3-D maps of the Galaxy (Udalski et al., 2016). To accomplish this objective, the satellite is continuously scanning the entire sky for a period of at least five years with its astrometric, photometric and spectroscopic instruments.

Gaia's G passband extends from the near ultraviolet (approximately 3300 \AA) to the near infrared (roughly 10500 \AA). The other two passbands, denoted G_{BP} and G_{RP} , cover shorter wavelength ranges, 3300 to 6800 \AA and 6300 to 10500 \AA , respectively.

A number of crucial parameters are provided by the high astrometric precision currently made possible by *Gaia* since its first public data was released on September 2016 (DR1, Gaia Collaboration et al., 2016b). The Gaia mission is now at its third data release (Gaia DR3, Gaia Collaboration et al., 2022). Gaia DR3 complements the early installment of the third Gaia data release (eDR3, Gaia Collaboration et al., 2021a) and brings additional data products including the high-resolution Radial Velocity Spectrometer (RVS) spectra.

In this thesis, we made use of *Gaia* measurements extensively. In the case of pulsating sdBs and WDs, in order to refine the distance measurements and investigate the contamination of the field of view of TESS, the precise parallax measurements from Gaia were used. Since each TESS pixel comprises 21 arcsec and we mainly focus on intrinsically faint targets, Gaia measurements become extremely useful (see Chapters 2, 3 and 4 for details).

In the case of volume-limited sample of low-mass RGBs, we made use of colors (G_{BP} and G_{RP}) and absolute magnitudes as well as astrometric excess noise and the Renormalised Unit Weight Error (RUWE) (see Chapter 5 for more details). Moreover, *Gaia* provided Non-single stars catalog (I/357²) from *Gaia* DR3, which enable us to detect more binary stars. Using a homogeneously created list from *Gaia*, we performed a spectroscopic survey to find binary systems that include low-mass red giants near the tip of the Red Giant Branch, which are predicted to be the direct progenitors of wide binary hot subdwarf B stars (Chapter 5).

1.4.2 Ground based data

EFOSC2 spectrograph at the New Technology Telescope (NTT)

The European Southern Observatory (ESO) Faint Object Spectrograph and Camera (v.2) (EFOSC2) (Buzzoni et al., 1984) is mounted at the Nasmyth B focus of the 3.58 m NTT at La Silla Observatory in Chile³. The wavelength range that NTT offers is spanning from 3 050 to 11 000 Å. For the EFOSC2 setup, we used grism #7 providing a wavelength range from 3 700 to 5 200 Å, and a 1 arcsec slit which resulted in a resolution ($\Delta\lambda$) between 3.1 and 5.4 Å (see Chapter 2).

²<https://cdsarc.cds.unistra.fr/viz-bin/cat/I/357>

³For a description of instrumentation, see: https://www.eso.org/sci/facilities/lasilla/instruments/efosc/doc/manual/EFOSC2manual_v3.1.pdf

GOODMAN spectrograph at the Southern Astrophysical Research (SOAR) Telescope

The Southern Astrophysical Research (SOAR) Telescope is a 4.1 meter aperture optical and near-infrared telescope (Clemens et al., 2004) designed to work from the atmospheric cut-off in the blue to the near infrared. SOAR was created to produce the most detailed images possible with any ground-based telescope at the time. SOAR is situated at Cerro Pachón, Chile. The Goodman spectrograph with a setup of 4001/mm grating with the blaze wavelength at 5 500 Å (M1: 3 000-7 050 Å). This setup provides a resolution of about 5.6 Å.

Boller and Chivens (B&C) spectrograph at the Irène du Pont telescope

The Boller and Chivens (B&C) spectrograph is mounted at the 2.5-meter (100-inch) Irène du Pont telescope⁴ at Las Campanas Observatory in Chile⁵. The detector in the B&C spectrograph is a Marconi CCD mated to a Bowen Schmidt camera. The resolution is about 3 Å with a wavelength coverage of 3 100 Å. The B&C spectra were obtained using the 600 lines/mm grating corresponding to the central wavelength of 5 000 Å, covering a wavelength range from 3 427 to 6 573 Å.

CORALIE echelle spectrograph at the Swiss 1.2-metre Leonhard Euler Telescope

The CORALIE échelle spectrograph was installed on the Swiss 1.2-metre Leonhard Euler Telescope at ESO-La Silla (Chile) in 1998. Its goal was to look for exoplanets, which prompted a high level of radial-velocity stability in order to detect a planet's small dynamical influence on the host star. CORALIE was fed two types of fibers to accomplish this: a science fibre and a reference fibre. The spectral resolution was $R = \lambda/\Delta\lambda \sim 50\,000$ at 5500 Å. The spectrograph covered the wavelength range from 3900 Å to 6800 Å.

⁴For a description of background, see: <https://obs.carnegiescience.edu/dupont>

⁵For a description of instrumentation, see: http://www.lco.cl/?epkb_post_type_1=boller-and-chivens-specs

Intermediate Dispersion Spectrograph (IDS) at the Isaac Newton Telescope (INT)

In addition to the spectrographs abovementioned, this thesis includes the data from the Isaac Newton Telescope (INT), a 2.54 m optical telescope run by the Isaac Newton Group of Telescopes at Roque de los Muchachos Observatory in Spain. We showed the result based on the data taken from the Intermediate Dispersion Spectrograph (IDS) long-slit spectrograph with the grating R400V ($R = 1452$) and a 1.5 arcsec slit with a resolution of about 3.5 \AA in Chapter 3.

1.5 Outline of this thesis

The dissertation is organized as follows :

In Chapter 2 the analysis of data collected for five pulsating hot subdwarf B stars, observed with the TESS mission is presented. Four of the five analyzed stars are new discoveries of long-period pulsating sdB (V1093 Her) stars. Combining with all the analyzed stars that were observed with Kepler and K2, we compare the observed mean period spacing of around 50 sdBV stars with the mean period spacings from detailed stellar evolution computations coupled with the adiabatic pulsation computations of g-modes. From TESS observations, the main asteroseismic conclusion is that modest convective boundary mixing at the boundary of the convective core agrees well with observed mean period spacings.

In Chapter 3 the discovery of two new GW Vir stars, TIC 333432673 and TIC 095332541, are presented. By fitting synthetic spectra to newly obtained low to intermediate resolution spectra, we derived atmospheric parameters for both stars. We processed and analyzed TESS observations of both targets, and carried out a detailed asteroseismological analysis of these stars on the basis of PG 1159 evolutionary models that take into account the complete evolution of the progenitor stars. We constrained the stellar mass by comparing the observed period spacing with the average of the computed period spacings, and employed the individual observed periods to search for a representative seismological model only for TIC 333432673. We found an excellent agreement between the seismological distance and that measured with Gaia for TIC 333432673. On the basis of PG 1159 evolutionary tracks and a possible period spacing value obtained from TESS, we derived the stellar mass for TIC 095332541. However, we did not find an asteroseismological model for TIC 095332541.

In Chapter 4 the discovery of two other new GW Vir-type pulsating white dwarf stars, TIC 0403800675 and TIC 1989122424 are presented based on the photometric data from TESS. We derived atmospheric parameters for both stars by fitting synthetic spectra to the newly obtained low-resolution SOAR/GOODMAN spectra. We used the TESS 120-second data for both objects, while we made use of 20-second cadence data only for TIC 0403800675. Both stars exhibit just two periodicities in their amplitude spectra preventing us to make use of the seismic tool of asymptotic period spacing. Examining sliding Fourier transform of each target, we showed potential doublets caused by stellar rotation. Using these rotationally splitting candidates, we constrained the rotation periods of cores for both targets. We derived the stellar masses for both targets using linear interpolation among the PG 1159 evolutionary tracks.

In Chapter 5 a volume-limited sample of low-mass red giant stars using data from the *Gaia* DR2 and eDR3 is presented. We conducted a spectroscopic survey with Euler/CORALIE to find binary systems containing low-mass red giants near the tip of the Red Giant Branch, which are thought to be the direct progenitors of wide binary hot subdwarf B stars. From the available radial velocity surveys and *Gaia*'s non-binary catalog, we found 33 low-mass RGB in binary systems with orbital periods between 100 and 900 days. We obtained high-resolution spectra of 82 stars, 38 of which were observed in two different epochs to determine the binary fraction. Combining these measurements with DR2 radial velocity and astrometric excess noise and RUWE from EDR3, and known binaries from the literature, we found 41 new binary candidates.

In Chapter 6 all results are summarized, and future work is discussed.

Pulsating hot subdwarf B stars


This chapter was originally published as:

A&A 651, A121 (2021)
<https://doi.org/10.1051/0004-6361/202140961>
 © ESO 2021

**Astronomy
&
Astrophysics**

Asteroseismic analysis of variable hot subdwarf stars observed with TESS

I. The mean g -mode period spacings in hot subdwarf B stars^{*}

Murat Uzundag^{1,2} , Maja Vučković¹, Péter Németh^{3,4}, M. Miller Bertolami⁵, Roberto Silvotti⁶, Andrzej S. Baran^{7,8,11}, John H. Telting^{9,10}, Mike Reed¹¹, K. A. Shoaf¹¹, Roy H. Østensen¹¹, and Sumanta K. Sahoo^{7,12}

Author contributions: Murat Uzundag initiated this project and did a majority of the work for this chapter. Maja Vučković provided guidance, discussion, and feedback as the analyses were developed and the manuscript was written. The spectroscopic observations and the data reduction were made by Murat Uzundag. Péter Németh produced the model atmosphere models using the spectral analysis tool XTGRID. M. Miller Bertolami computed stellar evolution models using the LPCODE stellar evolution code. Andrzej S. Baran, K. A. Shoaf and Sumanta K. Sahoo provided frequency solution for all targets. Roberto Silvotti, John H. Telting, Mike Reed and Roy H. Østensen contributed with useful discussions throughout the project. The text was written by M.U. and all co-authors provided useful feedback.

ABSTRACT

Context. We present photometric and spectroscopic analyses of gravity (g -mode) long-period pulsating hot subdwarf B (sdB) stars, also called V1093 Her stars, observed by the TESS space telescope in both 120 s short-cadence and 20 s ultra-short-cadence mode during the survey observation and the extended mission of the southern ecliptic hemisphere.

Aims. We performed a detailed asteroseismic and spectroscopic analysis of five pulsating sdB stars observed with TESS in order to compare the observations with model predictions based on our stellar evolution computations coupled with adiabatic pulsation computations.

Methods. We processed and analyzed TESS observations of long-period pulsating hot subdwarf B stars. We used standard pre-whitening techniques on the datasets to extract the pulsation periods from the TESS light curves. We applied standard seismic tools for mode identification, including asymptotic period spacings and rotational frequency multiplets. Based on the values obtained from Kolmogorov-Smirnov and Inverse Variance tests, we searched for a constant period spacing for dipole ($l = 1$) and quadrupole ($l = 2$) modes. We calculated the mean period spacing for $l = 1$ and $l = 2$ modes and estimated the errors by means of a statistical resampling analysis. For all stars, atmospheric parameters were derived by fitting synthetic spectra to the newly obtained low-resolution spectra. We computed stellar evolution models using the LPCODE stellar evolution code, and computed $l = 1$ g-mode frequencies with the adiabatic nonradial pulsation code LP-PUL. Derived observational mean period spacings were then compared to the mean period spacings from detailed stellar evolution computations coupled with the adiabatic pulsation computations of g-modes.

Results. We detect 73 frequencies, most of which are identified as dipole and quadrupole g-modes with periods spanning from $\sim 3\,000$ s to $\sim 14\,500$ s. The derived mean period spacing of dipole modes is concentrated in a narrow region ranging from 251 s to 256 s, while the mean period spacing for quadrupole modes spans from 145 s to 154 s. The atmospheric parameters derived from spectroscopic data are typical of long-period pulsating sdB stars with an effective temperature ranging from 23 700 K to 27 600 K and surface gravity spanning from 5.3 dex to 5.5 dex. In agreement with the expectations from theoretical arguments and previous asteroseismological works, we find that the mean period spacings obtained for models with small convective cores, as predicted by a pure Schwarzschild criterion, are incompatible with the observations. We find that models with a standard, modest convective boundary mixing at the boundary of the convective core are in better agreement with the observed mean period spacings and are therefore more realistic.

Conclusion. Using high-quality space-based photometry collected by the TESS mission coupled with low-resolution spectroscopy from the ground, we provide a global comparison of the observations with model predictions by means of a robust indicator such as the mean period spacing. All five objects that we analyze in this work show remarkable homogeneity in both seismic and spectroscopic properties.

2.1 Introduction

Hot subdwarf stars (sdB) are core-helium burning stars with a very thin hydrogen (H) envelope ($M_{\text{env}} < 0.01 M_{\odot}$), and a mass close to the core-helium (He)-flash mass $\sim 0.47 M_{\odot}$. The sdB stars are evolved, compact ($\log g = 5.0 - 6.2$ dex), and hot ($T_{\text{eff}} = 20\,000 - 40\,000$ K) objects

with radii between $0.15 R_{\odot}$ and $0.35 R_{\odot}$, and are located on the so-called extreme horizontal branch (EHB; see Heber, 2016, for a review). They have experienced extreme mass-loss mostly due to binary interactions at the end of the red giant phase, where they lost almost the entire H-rich envelope, leaving a He burning core with an envelope too thin to sustain H-shell burning. Hot subdwarf B stars will spend about 10^8 yr burning He in their cores. Once the He has been exhausted in their core, they will start burning He in a shell surrounding a carbon and oxygen (C/O) core as subdwarf O (sdO) stars, and will eventually end their lives as white dwarfs (Heber, 2016).

One of the major advances in our understanding of sdB stars was initiated by Kilkenny et al. (1997), who discovered rapid pulsations in hot sdBs known as V361 Hya stars (often referred to as short-period sdBV stars). The V361 Hya stars show multiperiodic pulsations with periods spanning from 60 s to 800 s. In this region, the pulsational modes correspond to low-degree, low-order pressure p-modes with photometric amplitudes up to a few per cent of their mean brightness (e.g. Reed et al., 2007; Green et al., 2011). These modes are excited by a classical κ -mechanism due to the accumulation of the iron group elements (mostly iron itself), in the Z-bump region (Charpinet et al., 1996, 1997). These latter authors also showed that radiative levitation is a key physical process in enhancing the abundances of iron group elements, which is needed to be able to excite the pulsational modes. The p-mode sdB pulsators are found in a temperature range between 28 000 K and 35 000 K and with the surface gravity $\log g$ in the interval 5-6 dex. Subsequently, the long-period sdB pulsators known as V1093 Her stars were discovered by Green et al. (2003). These show brightness variations with periods of up to a few hours and have amplitudes smaller than 0.1 per cent of their mean brightness (Reed et al., 2011). The oscillation frequencies are associated with low-degree ($l < 3$) medium- to high-order ($10 < n < 60$) g-modes, which are driven by the same mechanism (Fontaine et al., 2003; Charpinet et al., 2011). The g-mode sdB pulsators are somewhat cooler, with temperatures ranging from 22 000 K to 30 000 K and $\log g$ from 5 dex to 5.5 dex. Between the two described families of pulsating sdB stars, some “hybrid” sdB pulsators have been found that simultaneously show g- and p-modes. These hybrid sdB pulsators are located in the middle of the region of the HR diagram between p- and g-mode sdB pulsators (Green et al., 2011, Figure 5). These objects are of particular importance as they enable us to study both the core structure and the outer layers of the sdBVs via asteroseismology. A few examples have been found from the ground (Oreiro et al., 2005; Baran et al., 2005; Schuh et al., 2006; Lutz et al., 2008).

During the nominal *Kepler* mission (Borucki et al., 2010a), 18 pulsating subdwarf B stars were monitored in one-minute short-cadence mode. The majority of the stars (16) were found to be long-period g-mode pulsators, while just two of them were short-period p-mode pulsators (Østensen et al., 2010, 2011b; Baran et al., 2011; Reed et al., 2011; Kawaler et al., 2010). Additionally, 3 known sdBs stars in the old open cluster NGC 6791 were found to pulsate (Pablo et al., 2011; Reed et al., 2012). The temperature of these sdBs ranges from 21 500 K to 37 000 K with a median of 27 400 K and surface gravities between $\log g$ of 4.67 dex and

5.82 dex, with a median of 5.42 dex. In 2013, the *Kepler* mission was reinitiated after the second reaction-wheel failure and it continued as the K2 mission observing along the ecliptic (Haas et al., 2014). During the K2 mission, more than 25 sdBs were found to pulsate and analyses are still ongoing. To date, 18 of these sdBVs have been published together with their atmospheric parameters (Reed et al., 2016; Ketzer et al., 2017; Bachulski et al., 2016; Reed et al., 2019; Baran et al., 2019; Silvotti et al., 2019; Reed et al., 2020b; Østensen et al., 2020). These stars have T_{eff} in between 22 300 K and 37 000 K and $\log g$ from 5.2 dex to 5.7 dex (Reed et al., 2018, for a review).

For many sdBVs observed with *Kepler*, the asymptotic period sequences for g-mode pulsations have been successfully applied, especially for dipole ($l = 1$) and quadrupole ($l = 2$) modes, as more than 60% of the periodicities are associated with these modes (Reed et al., 2018). The asymptotic approximation can be perfectly applied for homogeneous stars. The period separation of g-modes becomes approximately constant for high radial orders. This is called the asymptotic regime of pulsations, and is masterfully documented in Tassoul (1980). It is important to note that the asymptotic g-mode theory is strictly valid for completely radiative and chemically homogeneous stars. However, sdB stars are stratified, and diffusion processes (gravitational settling and radiative levitation) contribute significantly to compositional discontinuities, which disturb the pulsational modes and could break the sequences of periods with constant spacing. This effect has been found in several g-mode-dominated sdBV stars. Furthermore, when the compositional discontinuities become stronger in transition zones, some modes are trapped; this was also detected for a few sdBV stars observed with *Kepler* (Østensen et al., 2014; Uzundag et al., 2017; Baran et al., 2017; Kern et al., 2018). Mode trapping is characterized by strong departures from a constant period spacing. Trapped modes can be useful, in that they provide a test for stellar evolution models, and offer a unique opportunity to determine mixing processes due to convective overshooting beyond the boundary of the helium-burning core (Ghasemi et al., 2017).

Another important asteroseismic tool, rotational multiplets, became available for sdB stars thanks to the long baseline of *Kepler* data (Baran, 2012). During the nominal mission of *Kepler*, the rotation periods of sdBs were found to range from 10 d to 100 d (Reed et al., 2014). For the short-period sdB systems with WD companions ($P_{\text{orb}} < 15$ d), the rotational periods of the sdBs were found to be in the range from 28 d to 50 d (Baran et al., 2019, references therein). For the short-period sdB binary systems with M-dwarf companions ($P_{\text{orb}} < 0.8$ d), rotational periods in the range between 7 and 40 days have been identified (Baran et al., 2019). Moreover, detecting rotational multiplets in both g- and p-modes in hybrid sdB pulsators is of special importance as these provide a way to determine the rotation of both the core and the envelope of these stars. Also, rotational splittings allow us to assign a harmonic degree to a pulsation mode. These remarkable stars have been found to be either solid-body rotators (Baran, 2012; Ketzer et al., 2017) or radially differential rotators (Foster et al., 2015; Baran et al., 2017). The rotation properties of evolved stars are further discussed in a recent review of Charpinet et al. (2018).

The Transiting Exoplanet Survey Satellite (TESS) was launched successfully on 18 April 2018. The primary goal of this mission is to discover exoplanets around nearby and bright stars by means of the transit method (Ricker et al., 2014). The spacecraft has four identical 100 mm aperture cameras and is in a highly eccentric lunar-resonance Earth orbit. The orbit allows the telescope to observe the targets over ~ 27 days continuously, covering a huge area in the sky ($24^\circ \times 96^\circ$). During the first year, TESS surveyed 13 sectors in the southern hemisphere at both a short cadence (SC) of 2 mins and a long cadence (LC) of 30 mins. Results from LC observations of the first year were reported by Sahoo et al. (2020c).

During the first year, TESS observed 1702 compact objects including hot subdwarfs, pre-white dwarfs, and white dwarfs at two-minute cadence. The first results of asteroseismic analysis of hot sdB pulsating stars observed by TESS were reported in three papers (Charpinet et al., 2019; Reed et al., 2020a; Sahoo et al., 2020a). In the present paper, we analyze five pulsating sdB stars, which were observed in a single sector in SC mode by TESS during the survey phase of the southern ecliptic hemisphere. For each of these TESS targets, we obtained low-resolution spectra and fitted model atmospheres in order to derive their fundamental atmospheric parameters. We present the details of spectroscopic and photometric observations as well as the main characteristics of the studied sdBVs in Sect. 2.2. We discuss the analysis of the TESS data in Sect. 2.3 and give details on the frequency analysis along with detailed seismic mode identification. In Sects. 2.4 and 2.5, we present our analysis of the spectroscopic data and atmospheric parameters for each star, derived by fitting synthetic spectra to the newly obtained low-resolution spectra. We calculate asteroseismic models in Sect. 2.6 and compare them with the observations. Finally, we summarize our findings in Sect. 2.7.

2.2 Observations

2.2.1 Photometric observations — TESS

The TESS mission Cycle 1, covering most of the southern hemisphere, started on 25 July 2018 and ended on 18 July 2019. During this time, a total of 13 sectors were observed, where each sector covered ~ 27 days of continuous observations in SC mode. During Cycle 1, TESS observed 806 subdwarf (sd) candidates including sdB stars, sdO stars, and their He-rich counterparts. Among them, we have found several rich oscillators including short- and long-period sdB pulsators. By “rich”, we mean that there are sufficient pulsation frequencies present for asteroseismic methods (e.g., rotational multiplets and/or asymptotic period spacing) to be applicable. To date, five rich, long-period sdB pulsators have been reported. Four of these stars have been analyzed by Sahoo et al. (2020a) and Reed et al. (2020a), who applied the asymptotic period spacing. For one target, Charpinet et al. (2019) produced a detailed model by best-matching all the observed frequencies with those computed from models. In the present paper, we concentrate on five other long-period pulsating sdB stars, TIC 260795163, TIC 080290366,

TIC 020448010, TIC 138707823, and TIC 415339307, that were observed by TESS. During Cycle 2, the second year of the primary mission, TESS observed the northern hemisphere, sectors 14-26, after which it re-observed the southern hemisphere in what is referred to as the extended mission. During the extended TESS mission, three of the selected stars (TIC 260795163, TIC 080290366 and TIC 138707823) were observed with 20s ultra-short-cadence (USC) mode. While TIC 080290366 and TIC 138707823 were observed in USC mode over only one sector (29), TIC 260795163 was observed in USC mode over two consecutive sectors (27 and 28).

Among the stars analyzed in this paper, the only star for which photometric variability was discovered before TESS is TIC 080290366 (Koen & Green, 2010). The remaining four V1093 Her stars are new discoveries. The details of the photometric TESS observations are summarized in Table 2.1, where we also give the literature name of the targets, which are taken from SIMBAD¹, the TESS Input Catalog (TIC) number, right ascension, declination, and T -magnitude along with their corresponding observed sectors. Using available magnitude values from the literature, we calculated TESS magnitude of all targets as described by Stassun et al. (2018) using the tool of *ticgen*².

2.2.2 Spectroscopic observations

The spectroscopic follow-up observations of the sdB pulsators analyzed in this paper were obtained with two instruments, the Boller and Chivens (B&C) spectrograph mounted at the 2.5-meter (100-inch) Irène du Pont telescope at Las Campanas Observatory in Chile³, and the European Southern Observatory (ESO) Faint Object Spectrograph and Camera (v.2) (EFOSC2) (Buzzoni et al., 1984) mounted at the Nasmyth B focus of the New Technology Telescope (NTT) at La Silla Observatory in Chile.

We obtained low-resolution spectra in order to calculate the atmospheric parameters, such as effective temperature T_{eff} , surface gravity $\log g$, and He abundance. Although the atmospheric parameters for TIC 260795163, TIC 080290366, TIC 020448010, TIC 138707823 and TIC 415339307 are available in the literature (Heber et al., 1984; Heber, 1986; Kilkeny et al., 1995, 1988a; Németh et al., 2012; Lei et al., 2018), we reobserved them in order to ensure homogeneity in our analysis. The B&C spectra were obtained using the 600 lines/mm grating corresponding to the central wavelength of 5000 Å, covering a wavelength range from 3427 to 6573 Å. We used a 1 arcsec slit, which provided a resolution of 3.1 Å. Depending on the brightness of the targets, the exposure times were between 300 s and 480 s, which was enough to obtain an optimal signal-to-noise ratio (S/N) to measure T_{eff} and $\log g$ with 5% precision. For the EFOSC2 setup, we used grism #7 and a 1 arcsec slit and the exposure times were between 200 s and 300 s. This setup provided a wavelength coverage from 3270 to 5240 Å with a

¹<http://simbad.u-strasbg.fr/simbad/>

²<https://github.com/TESSgi/ticgen>

³For a description of instrumentation, see: http://www.lco.cl/?epkb_post_type_1=boller-and-chivens-specs

Table 2.1: Five sdB stars studied in this work, including the TESS input catalog number, the name of the star from the Simbad database, right ascension, declination, TESS magnitude, and TESS observed sectors (including USC observations) and distances from *Gaia*, respectively.

TIC	Name	RA (J2000)	Dec (J2000)	T_{mag}	Sectors (USC)	Distance (pc)
260795163	EC23073-6905	23:10:35.5	-68:49:30.2	11.73	1 (27-28)	499.6 ± 14
080290366	JL194	00:31:41.6	-47:25:20.1	11.85	2 (29)	502.1 ± 13
020448010	GALEXJ11143-2421	11:14:22.0	-24:21:29.0	12.18	9	509.1 ± 14
138707823	FB1	00:03:22.1	-23:38:58.0	12.70	2 (29)	695.9 ± 28
415339307	HS0352+1019	03:55:14.3	+10:28:12.6	14.24	5	771.3 ± 33

Table 2.2: Columns correspond to the *TESS* input catalog number, the spectrograph used for observations (with corresponding number of spectra obtained), the observing date, the exposure times, the spectroscopic data resolution, and S/N at 4200 \AA , respectively.

TIC	Spectrograph	Date (MM/YY)	T_{exp} sec.	R ($\Delta\lambda$ (\AA))	S/N (@4200 \AA)
260795163	B&C (2) - EFOSC2 (1)	08,10/19, 01/20	420 - 300 - 200	3.1 - 5.4	120 - 80
080290366	B&C (2) - EFOSC2 (1)	08,10,01/20	450 - 240 - 200	3.1 - 5.4	100 - 150
020448010	EFOSC2 (2)	01/20	240	5.2	150
138707823	B&C (1) - EFOSC2 (1)	01/20	480 - 300	3.1 - 5.4	100 - 150
415339307	B&C (1)	08/20	420	3.1	70

S/N of about 150. TIC 260795163, TIC 080290366, and TIC 138707823 were observed with 2x2 binning mode at a resolution of 5.4 \AA , while TIC 020448010 was observed using 1x2 binning, such that the spectral resolution slightly improved to 5.2 \AA . The details of the spectroscopic observations are given in Table 5.3 including, instrument, date, exposure time, resolution, and S/N ratio at 4200 \AA .

2.2.3 The targets

- TIC 260795163 (EC 23073-6905) was discovered during the Edinburgh-Cape survey-II (Kilkenny et al., 1995) and was classified as an sdB star with low-dispersion spectrograms and *UBV* photometry. Kilkenny et al. (1995) derived $T_{\text{eff}} \sim 27000 \text{ K}$ and $\log g \sim 5$ dex, respectively. These latter authors reported a radial velocity variation of about $\pm 26 \text{ km/s}$. Subsequently, Magee et al. (1998) and Copperwheat et al. (2011a) measured the radial velocity of the star and did not find significant variation. The *Gaia*

DR2 parallax and corresponding distance for this object are $\pi = 2.002 \pm 0.058$ mas and $d = 499.6 \pm 14.4$ pc.

- TIC 080290366 (alias JL 194, EC 00292-4741, CD-48 106) is a well-known relatively bright hot subdwarf star with a T -band magnitude of 11.85. The star was observed several times and can be found in many surveys, including Hill & Hill (1966); Jaidee & Lyngå (1969); Kilkenny & Hill (1975); Wegner (1980); Kilkenny et al. (1988b, 2016). The atmospheric parameters of TIC 080290366 were derived by Heber et al. (1984) and also given by Kilkenny et al. (1988a). The authors showed that the effective temperature and surface gravity of TIC 080290366 are $T_{\text{eff}} = 25\,200$ K and $\log g = 5.20$ dex. The evolutionary status of TIC 080290366 was discussed by (Newell, 1973). The presence of a potential weak magnetic field was investigated by Mathys et al. (2012); however, the detection limit was not enough to be conclusive. The parallax and corresponding distance for this star extracted from *Gaia* DR2 are $\pi = 1.992 \pm 0.05$ mas and $d = 502.1 \pm 12.6$ pc.
- TIC 020448010 (EC 11119-2405) was discovered during the Edinburgh-Cape Blue Object Survey as a hot sdB star with V -band magnitude of 12.72 (Kilkenny et al., 1997). The atmospheric parameters were obtained by Németh et al. (2012). The authors found $T_{\text{eff}} = 23\,430 \pm 900$ K, $\log g = 5.29 \pm 0.15$ dex and a low surface He abundance of $\log(\text{He}/\text{H}) = -2.52 \pm 0.25$. Kawka et al. (2015) included the target in their survey for hot subdwarf binaries, but did not detect significant velocity variations. From *Gaia* DR2, the parallax and distance of this object are $\pi = 1.964 \pm 0.055$ mas and $d = 509.1 \pm 14.2$ pc, respectively.
- The discovery of TIC 138707823 (alias EC 00008-2355, FB1, TonS 135, PHL 2580, MCT 0000-2355) was led by Haro & Luyten (1962) who searched for faint blue stars in the region near the south galactic pole. TIC 138707823 was confirmed by Lamontagne et al. (2000) as an sdB star. Estimations of the atmospheric parameters of TIC 138707823 have been provided in several papers (Greenstein & Sargent, 1974; Kilkenny et al., 1977; Kilkenny et al., 1988a): effective temperature of 23 000 to 27 000 K and surface gravity of 5.4 to 5.6 dex. Heber (1986) measured T_{eff} and $\log g$ as $25\,600 \pm 1\,250$ K and 5.60 ± 0.20 dex, respectively. Edelmann et al. (2005) found that TIC 138707823 is a binary system comprised of an sdB and a main sequence (MS) or a white dwarf (WD) companion with an orbital period of $P_{\text{orb}} = 4.122 \pm 0.008$ d. Geier & Heber (2012) calculated the atmospheric parameters of TIC 138707823 from UVES spectroscopy and found $T_{\text{eff}} = 27\,600 \pm 500$ K and $\log g = 5.43 \pm 0.05$ dex. From *Gaia* DR2, the parallax and distance of TIC 138707823 are $\pi = 1.437 \pm 0.057$ mas and $d = 695.9 \pm 27.7$ pc, respectively.
- TIC 415339307 (HS 0352+1019) was included in the KISO Survey and Hamburg Quasar Survey (Wegner & Boley, 1993; Edelmann et al., 2003). The atmospheric parameters were determined by Edelmann et al. (2003), who found $T_{\text{eff}} = 24\,900 \pm 600$ K, $\log g = 5.34 \pm 0.1$ dex, and $\log(n_{\text{He}}/n_{\text{H}}) = -2.7 \pm 0.2$. Recently, Lei et al. (2018) derived $26\,340 \pm$

150 K, 5.33 ± 0.01 dex and $\log(n_{\text{He}}/n_{\text{H}}) = -2.68 \pm 0.06$. From *Gaia* DR2, the parallax and distance of TIC 415339307 are $\pi = 1.296 \pm 0.056$ mas and $d = 771.36 \pm 33.04$ pc, respectively.

2.3 Analysis of TESS data

We analyzed *TESS* observations using the SC mode, which samples every 2 mins, allowing us to analyze the frequency range up to the Nyquist frequency at about 4 167 μHz . Given that the *TESS* USC data, with 20s sampling time, recently became available for three of the stars analyzed here, we include the analysis of the USC data when available. The Nyquist frequency of the USC data is at about 25 000 μHz which allows us to analyze the short period range of the pulsation spectra. The light curves were processed using the Science Processing Operations Center (SPOC) pipeline (Jenkins et al., 2016), which is based on the Kepler Mission science pipeline and made available by the NASA Ames SPOC center and at the MAST archive⁴.

We first downloaded the target pixel file (TPF) of interest from the MAST archive, which is maintained by the Lightkurve Collaboration (Lightkurve Collaboration et al., 2018). The TPFs include an 11x11 postage stamp of pixels from one of the four CCDs per camera that the target is located on. The TPFs are examined to determine the amount of crowding and other potential bright sources near the target. We used TPFs to optimize the aperture if needed. In most cases, we used the pipeline aperture as it gave the most optimal result with respect to S/N. Given that the pixel size of *TESS* is very large (21 arcsec) we need to pay special attention to possible contamination. The contamination factor is indicated with the keyword CROWDSAP, which gives the ratio of the target flux to the total flux in the *TESS* aperture. For the each target, we checked the contamination by looking at the CROWDSAP parameter which is listed in Table 2.3. For the three stars (TIC 260795163, TIC 080290366 and TIC 138707823) that were also observed during the extended mission, we give the relevant parameters in parentheses in Table 2.3. For four targets, TIC 080290366, TIC 020448010, TIC 138707823 and TIC 415339307, the CROWDSAP value is higher than 0.9, which implies that less than 10% of the total flux originally measured in the *TESS* aperture comes from other unresolved sources. For TIC 260795163, the CROWDSAP is smaller than 0.7 (for SC mode observations) and almost 40% of the flux comes from the other background sources. As the difference in magnitude between the target and nearby object is more than four, we can safely conclude that the flux variations indeed come from the sdB star. For the extended mission, the CROWDSAP is much better for TIC 260795163, with 0.81, and for TIC 080290366 and TIC 138707823 it is the same as for the SC data, i.e., greater than 0.9.

We generated the light curves by integrating the fluxes ('PDCSAP FLUX'⁵) within the aperture mask as a function of time in barycentric corrected Julian days ('BJD - 2457000'). After

⁴<http://archive.stsci.edu>

⁵The pre-search data conditioning (PDC) flux, which corrects the simple aperture photometry (SAP) to remove instrumental trends.

that, we removed the outliers that vary significantly from the local standard deviation (σ) by applying a running 5σ clipping mask. We then detrended the light curves to remove any additional low-frequency systematic error that may be present in the data. To do this, we applied a Savitzky–Golay filter with a three-day window length computed with the Python package `LIGHTKURVE`. Detrending with this method suppressed any spurious frequencies below $1 \mu\text{Hz}$, which is the typical region where spurious frequencies are seen in TESS data. We also examined the light curves before applying the low-frequency fitting in order to search for any potential binary signals that might be affected by detrending. However, we did not find binary signatures in the FT of any of the five stars. The fluxes were then normalized and transformed to amplitudes in parts-per-thousand (ppt) unit $((\Delta I/I - 1) \times 1000)$. For TIC 260795163, which was observed during two consecutive sectors in USC mode, we combined the light curves.

2.3.1 Frequency analysis

The Fourier transforms (FT) of the light curves were computed to examine the periodicities present in the data, aiming at identifying the frequency of all pulsation modes, along with their amplitude and phase.

We adopt a relatively conservative detection threshold of 0.1% false alarm probability (FAP), which means that if the amplitude reaches this limit, there is a 0.1% chance that it is simply the result of noise fluctuations. We calculated the 0.1% FAP threshold following the method described in Kepler (1993).

The temporal resolution of the data is around $0.6 \mu\text{Hz}$ ($1.5/T$, where T is the data length, which is between 24 and 27 d). In Table 2.3, we list all relevant information regarding the Fourier transform, including the number of data points and the 0.1% FAP level of each dataset.

For all the peaks that are above the accepted threshold and up to the frequency resolution of the particular dataset, we performed a nonlinear least square (NLLS) fit in the form of $A_i \sin(\omega_i t + \phi_i)$, with $\omega = 2\pi/P$, where P is the period. In this way, we determined the values of frequency (period), phase, and amplitude corresponding to each periodicity. Using the parameters of NLLS fit, we prewhitened the light curves until no signal above the 0.1% FAP level was left in the FT of each star unless there were unresolved peaks. For all frequencies that still had some signal left above the threshold after prewhitening we carefully checked if there was a close-by frequency within the frequency resolution and in such cases only the highest amplitude frequency was fitted and prewhitened, as shown in Figs. 2.3 and 2.5. All prewhitened frequencies for each of the five stars are given in Tables 2.4, 2.5, 2.6, 2.7, and 2.8, showing frequencies (periods) and amplitudes with their corresponding errors and the S/N ratio. The Fourier transforms of the prewhitened light curves of all five analyzed stars are shown in Figures 2.13, 2.14, 2.15, 2.16, and 2.17.

For all five stars analyzed in this paper, a total of 73 frequencies were extracted from their light curves. The detected frequencies are distributed in a narrow region between $68 \mu\text{Hz}$ and $315 \mu\text{Hz}$. This corresponds to the g-mode region seen in V1093 Her-type sdB pulsators

Table 2.3: Columns 1 to 7 correspond to the *TESS* input catalog number, *Gaia* magnitudes, duration of each dataset, the CROWDSAP keyword, the number of data points, data resolution, and the significance level, respectively. In parenthesis, the details from the extended mission observations are given. For more details, see the text.

TIC	G_{mag}	Obs. (day)	CROWDSAP	N.data	Resolution (μHz)	0.1% FAP (ppt)
260795163	12.56	27.88 (49.39)	0.61 (0.81)	18099 (192385)	0.623 (0.352)	0.467 (0.278)
080290366	12.38	27.40 (24.25)	0.93 (0.94)	18312 (88731)	0.634 (0.716)	0.36 (0.325)
020448010	12.77	24.20	0.96	15946	0.717	0.429
138707823	13.27	27.40 (23.85)	0.99 (0.99)	18317 (85563)	0.634 (0.728)	0.563 (0.66)
415339307	14.15	25.99	0.95	17660	0.668	1.270

(e.g., Reed et al., 2018). The amplitude spectra of all five stars are shown in Fig. 2.1, where we also give atmospheric parameters derived in Section 2.4 for each star. Reed et al. (2020a) recently reported a correlation between effective temperature and the frequency of the highest amplitude of g-modes detected in V1093 Her-type sdB pulsators observed by *Kepler* and K2. As can be seen in Fig. 2.1, the five g-mode sdB pulsators analyzed in this paper do not deviate from this finding.

TIC 260795163 ($T_{mag} = 11.73$) was observed in SC during sector 1 between July 25 and August 22 2018. The observations yielded 18 099 data points with the temporal resolution of $0.62 \mu\text{Hz}$ ($1.5/T$, where T is 27.87 d). From sector 1 data, we detected 12 frequencies above 0.1% FAP confidence level, which corresponds to 0.467 ppt. The median noise level including the entire FT is equal to 0.09 ppt. The S/N of detected frequencies ranges from 4.75 to 30.87.

TIC 260795163 was also observed during two consecutive sectors of the extended mission. These observations started on 22 September 2020 and ended on 17 December 2020. From this 84-day dataset, we calculate the FT of the USC data up to Nyquist frequency of $25\,000 \mu\text{Hz}$. The frequency resolution of USC data is $0.14 \mu\text{Hz}$. The average noise level of the entire FT of the USC dataset is 0.055 ppt and the 0.1% FAP threshold level is 0.26 ppt. All frequencies with amplitudes above this threshold are concentrated in a narrow region between 100 and $320 \mu\text{Hz}$, which is almost identical to what we detected from the SC observations. Beyond $320 \mu\text{Hz}$, there is no peak detected above the 0.1 % FAP threshold up to the Nyquist frequency. We find only one peak reaching the 4.5σ level at $23\,975.8 \mu\text{Hz}$. However, this frequency seems too high to be excited in an sdB pulsator.

Concerning the g-mode region, we extracted 23 significant frequencies from both sector 1 and the extended mission (sector 27 and 28) dataset. The 13 frequencies that are found in both sectors (sector 1 and sector 27+28) are provided in Table 2.4. We found seven frequencies in the extended mission dataset that were not detected in sector 1. These frequencies are also provided in Table 2.4. As can be seen in the Fig. 2.2, there are several frequencies above the

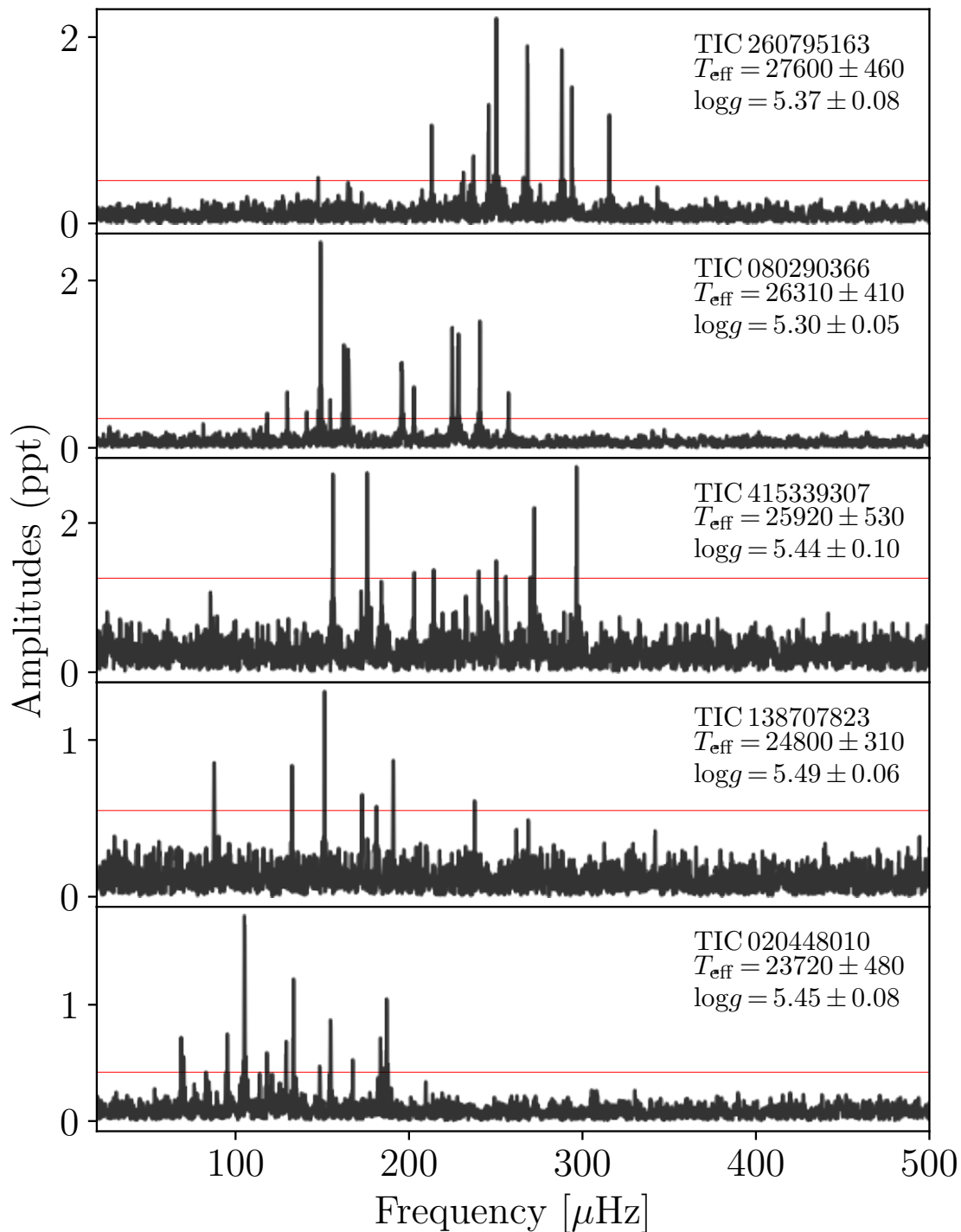


Figure 2.1: Fourier transform of all five sdB stars observed in single SC sectors, concentrating on the g-mode region of the frequency spectrum. The panels are sorted with decreasing effective temperature from top to bottom. In each panel, we give the *TESS* input catalog number, effective temperature (in Kelvin), and surface gravity (in dex), respectively. The horizontal red lines correspond to 0.1% FAP confidence level.

threshold level in the extended mission (sector 27 and 28) that are not detected in sector 1 (see Table 2.4 frequencies tagged with †).

The amplitude spectrum of this object is dominated by a number of frequencies between 100 and 315 μHz , as shown in Fig.2.2. The top panel presents the amplitude spectrum from sector 1, while the bottom panel shows the amplitude spectrum from sectors 27 and 28. In the lower frequency region, the four peaks (f_1 , f_2 , f_3 and f_8) were detected in sectors 27 and 28. The frequency f_5 is within 4.5σ level in 120-sec cadence data and in the USC data it is becoming a significant peak above 0.1% FAP level. However, there is a frequency, f_4 , that is detected only in sector 1, with a S/N of 4.75, while it is not detected in sectors 27 and 28. Also, there are residuals in the FT of the USC data after prewhitening. These residuals are shown in Fig. 2.3. The strong residuals at f_{13} and f_{23} could either be due to unresolved close-by frequencies or to amplitude, frequency, or phase variations over the length of the data. For these residuals, we did not prewhiten further. Overall, combining the nominal and extended mission dataset, we detect 23 g-modes spanning from 127 to 315 μHz .

TIC 080290366 was found to be a pulsating star by Koen & Green (2010), who detected five oscillation frequencies ranging from 127 μHz to 233 μHz . TIC 080290366 ($T_{mag} = 11.85$) was observed in SC mode during sector 2 (2018-Aug-22 to 2018-Sep-20) for 27.4 d, with a frequency resolution of 0.63 μHz . Other parameters such as the length of the observations, contamination, number of data points, and 0.1% FAP confidence level are given in Table 2.3. From sector 2, we detected 16 frequencies between 81 and 257 μHz .

TIC 080290366 was also observed during the extended mission in sector 29 (2020-Aug-26 to 2020-Sep-22). The data length of sector 29 is 24.3 d, implying a lower frequency resolution of 0.72 μHz . The FT average noise level is 0.067 ppt. The 0.1% FAP confidence level is 0.316 ppt. We did not detect any high-frequency p-mode from the USC observations, while we detected 17 g-mode frequencies, most of them being present already in sector 2. All the frequencies that were detected in both the nominal and extended mission are listed in Table 2.5. In total, we detected 18 frequencies spanning from 81.6 μHz ($\sim 12\,200$ s) to 257.4 μHz ($\sim 3\,900$ s) with amplitudes between 0.3 and 2.5 ppt. Fifteen frequencies are detected in both datasets, the frequency near 141.7 μHz was detected only in sector 2, while the three frequencies near 90.9, 114.7, and 168.0 μHz were found only in sector 29.

The FTs of sector 2 (upper panel) and sector 29 (lower panel) are shown in Fig. 2.4, where several frequencies clearly show differences. In Fig. 2.5, we show the amplitude spectrum of sector 29 in more detail around the regions in which a power excess is left after prewhitening compared with the window function.

TIC 020448010 ($T_{mag} = 12.18$) was observed in SC mode during sector 9 for a period of 24.2 d, which provides a frequency resolution of 0.717 μHz . The FT average noise level is 0.088 ppt. The rest of the parameters, including length of the observations, contamination, number of data points, and 0.1% FAP confidence level, are given in Table 2.3. The star was discovered by TESS as a g-mode sdB pulsator with 15 frequencies concentrated in a narrow region ranging

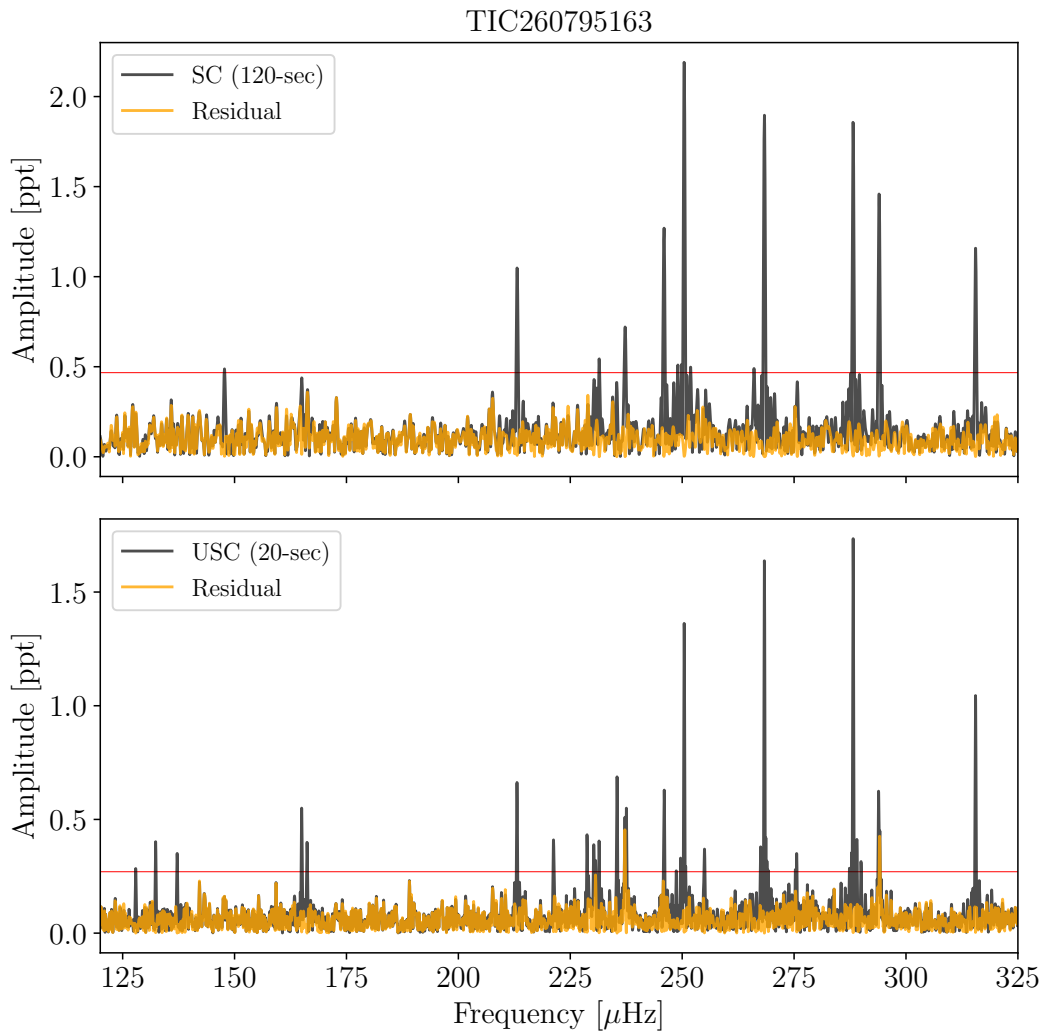


Figure 2.2: TOP: Fourier transform of sector 1 of TIC 260795163. The horizontal red line indicates the 0.1% FAP level. The orange line is the residual after extraction of the signals. BOTTOM: Fourier transform of sectors 27 and 28 of TIC 260795163. The horizontal red line indicates the 0.1% FAP level. The orange line is the FT of the prewhitened light curve.

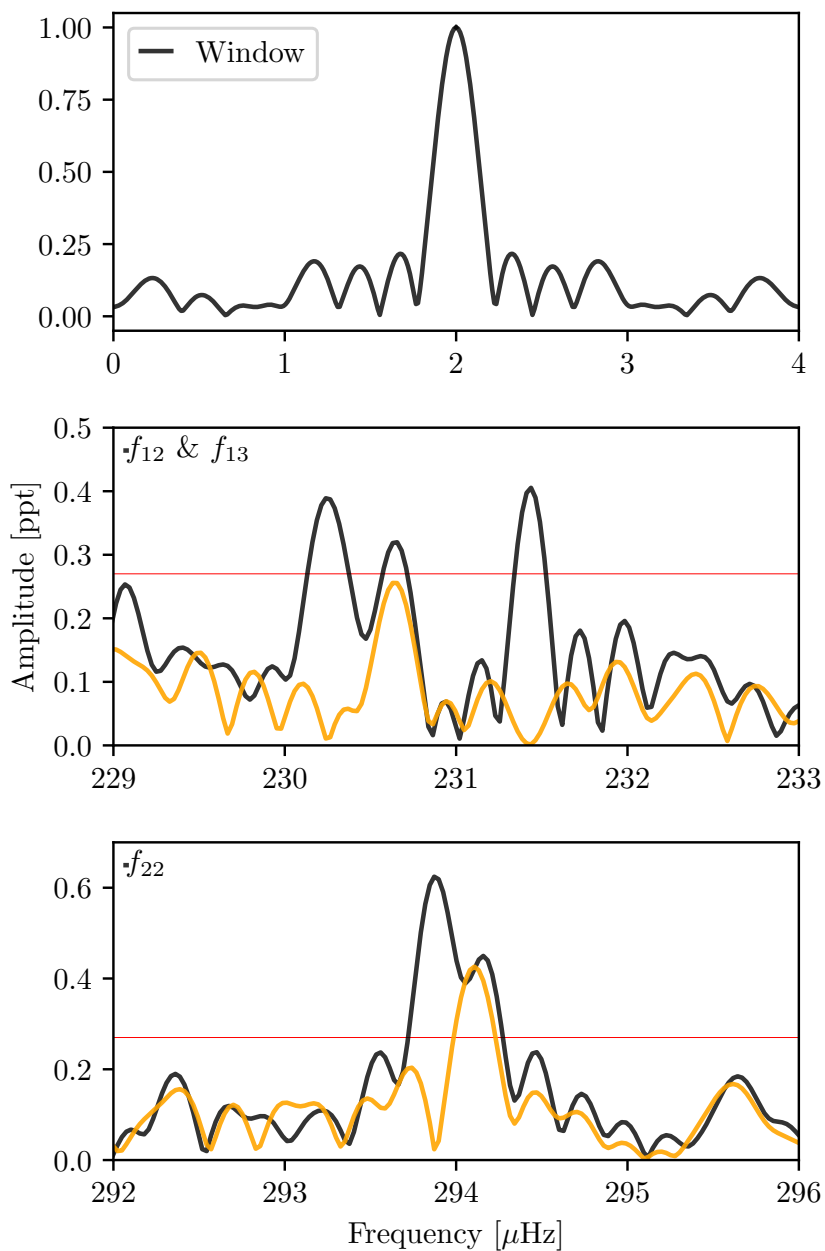


Figure 2.3: Fourier transform of USC data of TIC 260795163. The top panel shows the window function calculated from USC data. The second and third panels from the top display two different frequency regions in which the signals show strong residuals after the extraction. These frequencies are given in Table 2.4. The horizontal red line indicates the 0.1% FAP level. The orange line is the FT of the prewhitened light curve.

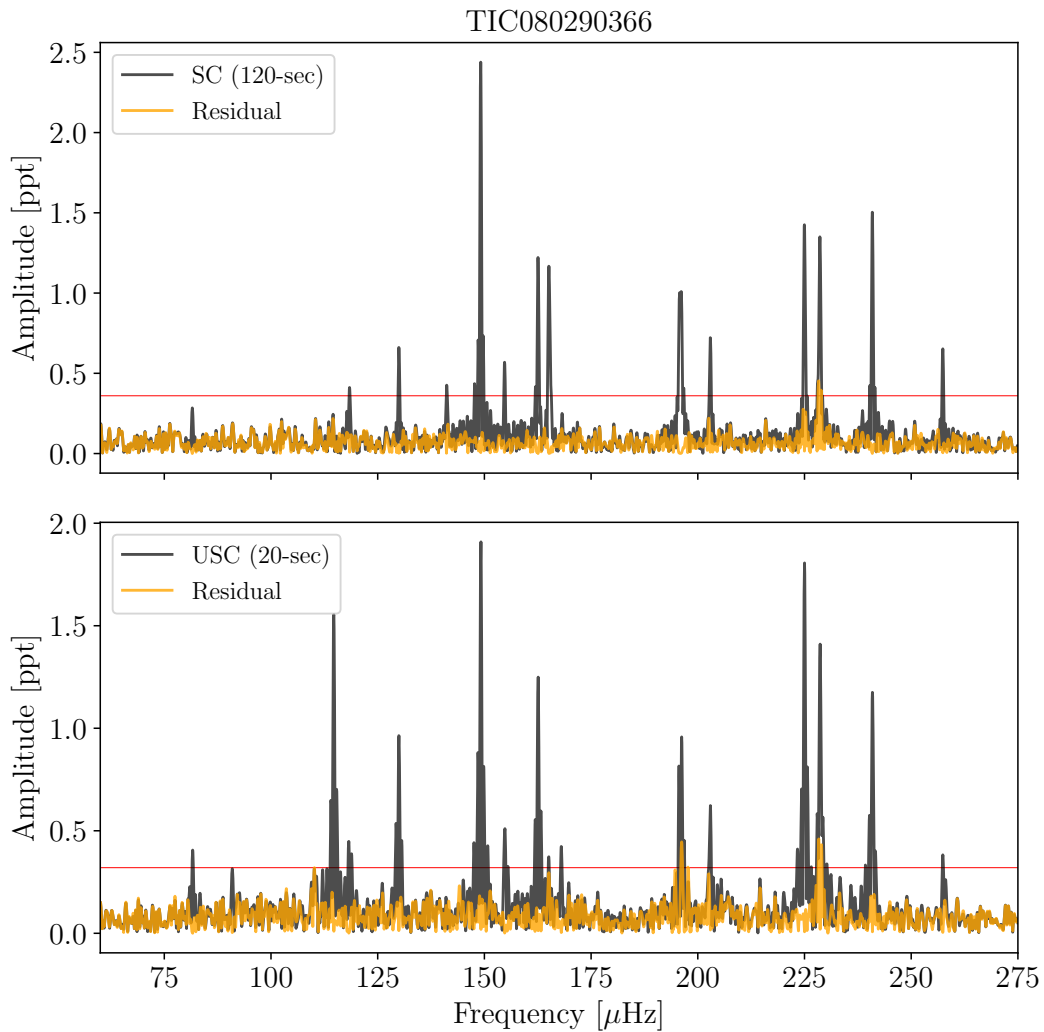


Figure 2.4: TOP: Fourier transform of data taken in sector 2 of TIC 080290366. The horizontal red line indicates the 0.1% FAP level. The orange line is the residual after extraction of the signals. BOTTOM: Fourier transform of data taken in sector 29 of TIC 080290366. The horizontal red line indicates the 0.1% FAP level. The orange line is the FT of the prewhitened light curve.

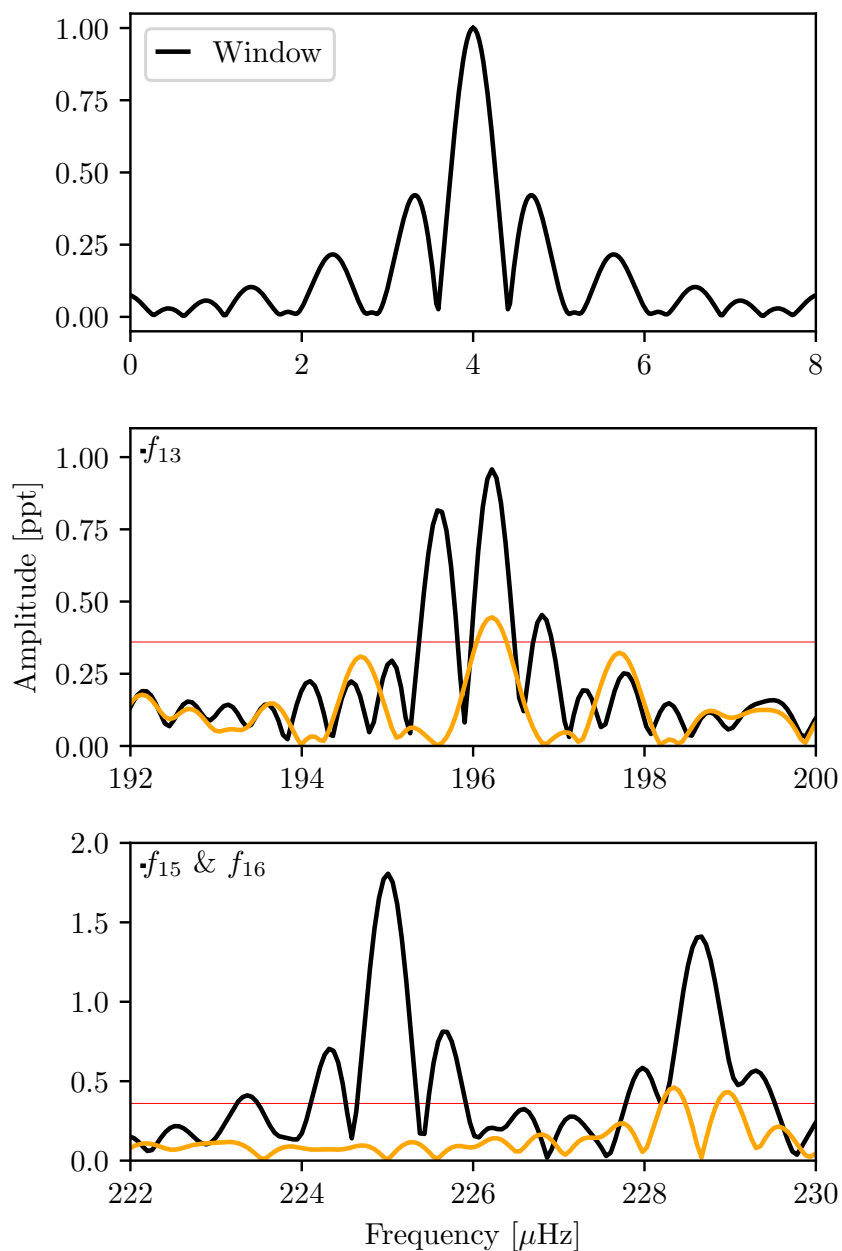


Figure 2.5: Fourier Transform of sector 29 of TIC 080290366, compared with the window function (top panel). The lower panels show an excess of power after prewhitening (orange line), see Section 2.3.3 for more details. The horizontal red line indicates the 0.1% FAP level.

from $68 \mu\text{Hz}$ to $187 \mu\text{Hz}$ and with amplitudes of between 0.36 ppt and 1.26 ppt. The extracted frequencies are listed in Table 2.6 with their associated errors and S/N. In Fig. 2.15, we show all detected frequencies (light gray) and residuals (orange) after prewhitening.

TIC 138707823 ($T_{mag}=12.7$) was observed in SC mode during sector 2 between August 22 and September 20, 2018, for 27.4 days. From these SC observations of TIC 138707823, we extracted seven periodicities from the light curve. All frequencies above 0.1% FAP significance level of 0.563 ppt are listed in Table 2.7. The frequencies are located in a narrow range from 87 to $237 \mu\text{Hz}$.

TIC 138707823 was also observed during Sector 29 (2020-Aug-26 to 2020-Sep-22) with USC mode. The length of these observations (23.85 d) is almost 4 days shorter than the sector 2 dataset, resulting in somewhat poorer frequency resolution ($0.728 \mu\text{Hz}$) than that obtained for the SC dataset ($0.634 \mu\text{Hz}$). The average noise level of the FT is 0.13 ppt. We extracted three significant frequencies above the threshold of 0.62 ppt. These three frequencies, which were also detected in sector 2, are marked with ++ in Table 2.7. The four frequencies at 87, 132, 181, and $191 \mu\text{Hz}$, which were not detected during the extended mission, are given without symbols in Table 2.7.

The amplitude spectrum of the sector 2 data for TIC 138707823 is relatively poor in comparison with that of the four stars presented in this work, displaying only seven frequencies above the threshold level. These seven frequencies can be seen in the upper panel of Fig. 2.16. The bottom panel of the same figure shows only three significant frequencies from sector 29. Combining the results from sector 2 and 29, we detect seven frequencies which are concentrated between $87 \mu\text{Hz}$ and $237 \mu\text{Hz}$.

TIC 415339307 ($T_{mag} = 14.2$) was observed by TESS in SC mode during sector 5 between 15 November 2018 and 11 December 2018, covering about 26 days. The amplitude spectrum of this object, shown in Fig. 2.17, contains nine frequencies above the 0.1% FAP significance level of 1.27 ppt. The average noise level of the FT is 0.26 ppt. We note that there is a frequency at $184.122 \mu\text{Hz}$ (f_3) just below the 0.1% FAP confidence level, albeit at 4.5σ , which we keep as a candidate frequency and discuss its nature in section 2.3.3.

The photometric and FT parameters, including average noise level, contamination factor, number of data points, and 0.1% FAP confidence level, are given in Table 2.3. In Table 2.8, we list all (10) frequencies (periods) and their amplitudes with corresponding errors and we show all detected frequencies in Fig.2.17.

2.3.2 Rotational multiplets

Our main goal is to identify modes of detected pulsations in order to constrain theoretical models of pulsating sdB stars. For rotating stars, the existence of nonradial oscillations allows identification of the pulsation modes via rotational multiplets (Aerts et al., 2010). The nonradial pulsations are described by three quantized numbers, n , l , and m , where n is the number of radial nodes between center and surface, l is the number of nodal lines on the surface, and

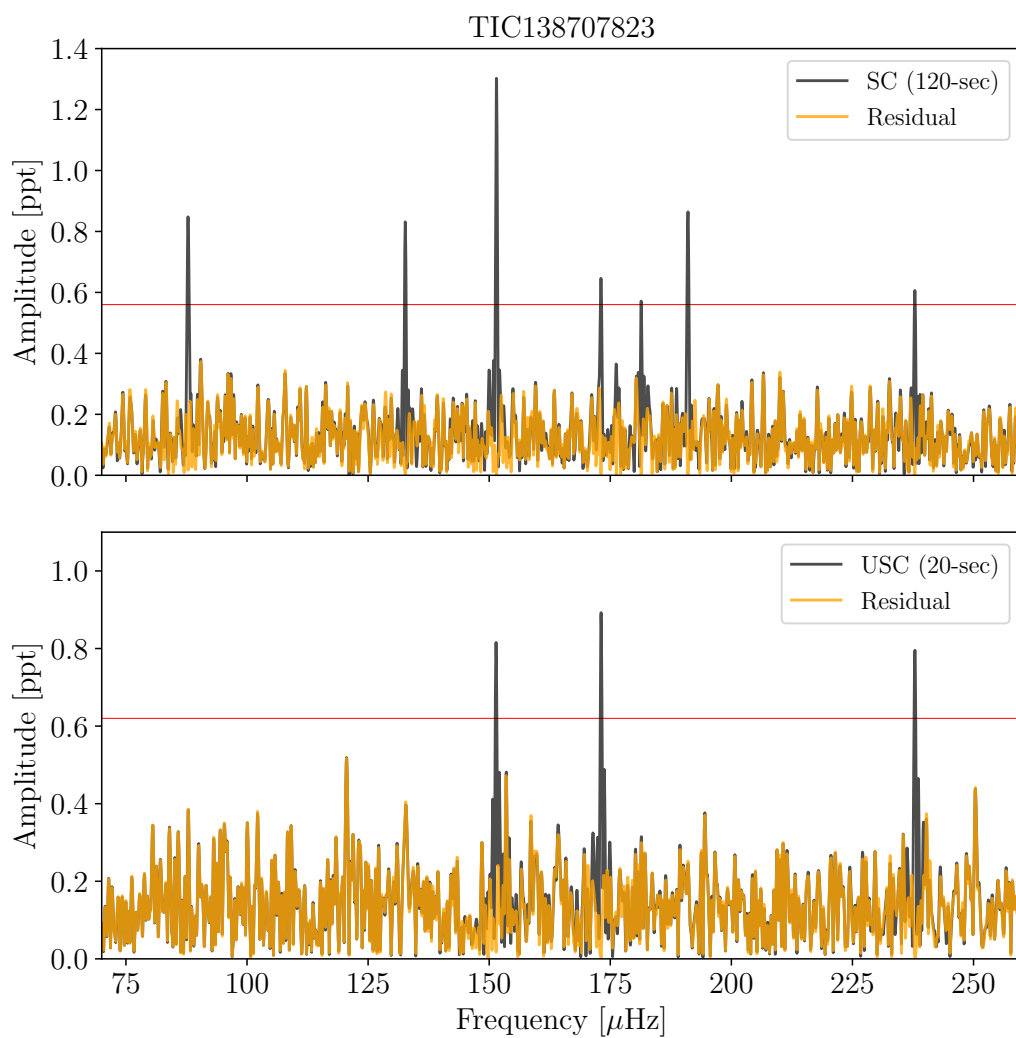


Figure 2.6: TOP: Fourier transform of sector 2 data of TIC 138707823. The horizontal red line indicates the 0.1% FAP level. The orange line is the residual after extraction of the signals. BOTTOM: Fourier transform of sector 29 data of TIC 138707823. The horizontal red line indicates the 0.1% FAP level. The orange line is the FT of the prewhitened light curve.

m is the azimuthal order, which denotes the number of nodal great circles that connect the pulsation poles of the star.

In rotating stars, the pulsation frequencies are split into $2l+1$ azimuthal components due to rotation, revealing an equally spaced cluster of $2l+1$ components. This $2l+1$ configuration can be resolved with high-precision photometry if the star has no strong magnetic field and the rotational period is not longer than the duration of the observation.

The detection of rotational splitting is important as it is one of the two methods used to identify the pulsational modes of a star and at the same time provides information about the rotation period of the star. In particular for the g-mode pulsators, such a detection unveils the rotation of the deep part of the radiative envelope close to the convective core.

Rotational multiplets have been detected in several sdBVs (Charpinet et al., 2018, references therein). Typical rotation periods detected in sdB stars are of the order of 40 d (Baran et al., 2019), unless the stars are in close binary systems. Even though TESS allows us to obtain uninterrupted time-series, especially for stars observed in multiple sectors, it is not ideally suited for the detection of rotationally split multiplets in sdBVs. For the stars that have been observed in just 1 sector (~ 27 d), which translates to a frequency resolution of $\sim 0.6 \mu\text{Hz}$, we are limited to the detection of rotational periods shorter than about 13 days. For each star, we searched for a coherent frequency splitting, $\Delta\nu$, in the g-mode region but did not find any consistent solution. Therefore, we conclude that it is not possible to perform mode identification for either of the sdBV stars analyzed in this paper, or to determine the rotational period based on rotational splitting. Given that four of the analyzed stars are not members of close binaries, we do not expect them to have short rotation periods such that they could be detected in a single sector TESS data. However, for TIC 138707823, which is a short-period binary system with an orbital period of about 4 d (Edelmann et al., 2005), we do not detect any significant signal that might be attributed to this orbital period.

2.3.3 Frequency and amplitude variations

From the continuous light curves produced by the space missions such as *Kepler* and K2, and now TESS, it has been observed that oscillation frequencies in compact stars, including pulsating sdB stars, and DBV and DOV pulsating white dwarfs, may not be stable (Silvotti et al., 2019; Zong et al., 2016; Córscico et al., 2020). It is known that the frequency and amplitude variations mostly occur because of beatings of unresolved peaks or unresolved multiplets. Recently, the complex patterns that have been observed were interpreted as evidence of frequency, amplitude, or phase modulations due to weak nonlinear mode interactions, as discussed in Zong et al. (2016). Furthermore, the variability may be due to the photon-count noise caused by contamination of the background light in the aperture.

The continuous photometric measurements of five stars allow us to construct sliding FTs (sFTs) to examine the temporal evolution of the detected frequencies over the course of the TESS observations. Therefore, we computed and examined the sFT of each target. As three

targets were observed in more than one sector, for these stars we selected the sectors in which we see the largest number of pulsation modes, i.e., sectors 27 and 28 for TIC 260795163, sector 29 for TIC 080290366, and sector 2 for TIC 138707823.

The sFTs are computed in a similar way as described in Silvotti et al. (2019): we run a five-day sliding window with a step size of 0.2 days. The amplitudes are illustrated by a color-scale in ppt units. We set a lower limit on the amplitudes by running the three-times-average noise level of the five-day window. Afterwards, we calculate the Fourier transform of each subset and trail them in time.

Figures 2.7, 2.8, 2.9, 2.10, and 2.11 show the sFTs for the g-mode region of each star. In most of the cases, the high-amplitude frequencies ($S/N \geq 10$) are stable in both frequency and amplitude over the length of the data for all stars. However, some pulsational frequencies are not stable throughout the TESS run and here we discuss each case.

In the case of TIC 260795163, the highest amplitude frequencies (at 250.447, 268.360, 288.186 and 315.537 μHz) are stable in frequency, although the one at 250 μHz shows a small wobble. A few frequencies, mostly lower than 250 μHz , are not stable, at least in amplitude. However, they have a low S/N and therefore are below the detection threshold throughout part of the run. In the case of the frequency at 293.996 μHz (f_{22}), it is quite stable up to day ~ 2050 and then becomes weaker in amplitude. Indeed, we can see this effect in the bottom panel of Fig. 2.3, in which we show the strong residual after prewhitening, implying that either the amplitude, phase, or frequency could be variable over the length of the data. In the case of TIC 080290366 (see Fig. 2.8), the amplitudes of the frequencies at 196.144 (f_{14}) and 228.658 μHz (f_{17}) are variable and it is exactly these two frequencies that show residuals after prewhitening in Fig. 2.5. The highest amplitude frequency at 105.313 μHz (f_5) of TIC 020448010 is relatively stable over the run, along with the frequency at 133.516 μHz (f_{10}) (Fig. 2.9). The low-amplitude frequencies are mostly unstable in amplitude; for example the frequency at 83.096 μHz is absent between days 1551 and 1555.

In the case of TIC 138707823 (Fig. 2.10), we safely extracted seven peaks from the SC observations and all the frequencies are visible in the sFT except for the frequency at 237.895 μHz , whose S/N is low. The highest amplitude frequency at 151.497 μHz is stable over the length of the data, while the rest of the frequencies (87.82, 132.67, 173.09, 181.38 and 191.02 μHz) are not stable in amplitude, while they seem to be stable in frequency.

In the case of TIC 415339307 (Fig. 2.11), the frequency at 175.929 μHz shows strong variability in amplitude, being at very low S/N in the first half of the run while in the second half it has the highest amplitude of about 4 ppt. In Fig. 2.17, this effect is seen as a significant residual at 5684 s. Frequencies at 203.126 and 214.359 μHz are not stable in either frequency or amplitude. The frequency at 184.122 μHz (f_3) ($S/N = 4.45$ in the entire FT) is definitely present in the sFT, however it is not stable in either frequency or amplitude during the first half of the run, while it appears more stable in frequency during the second half of the run. The frequency at 255.863 μHz is stable up to almost 1448 d, while it is absent beyond 1448 d.

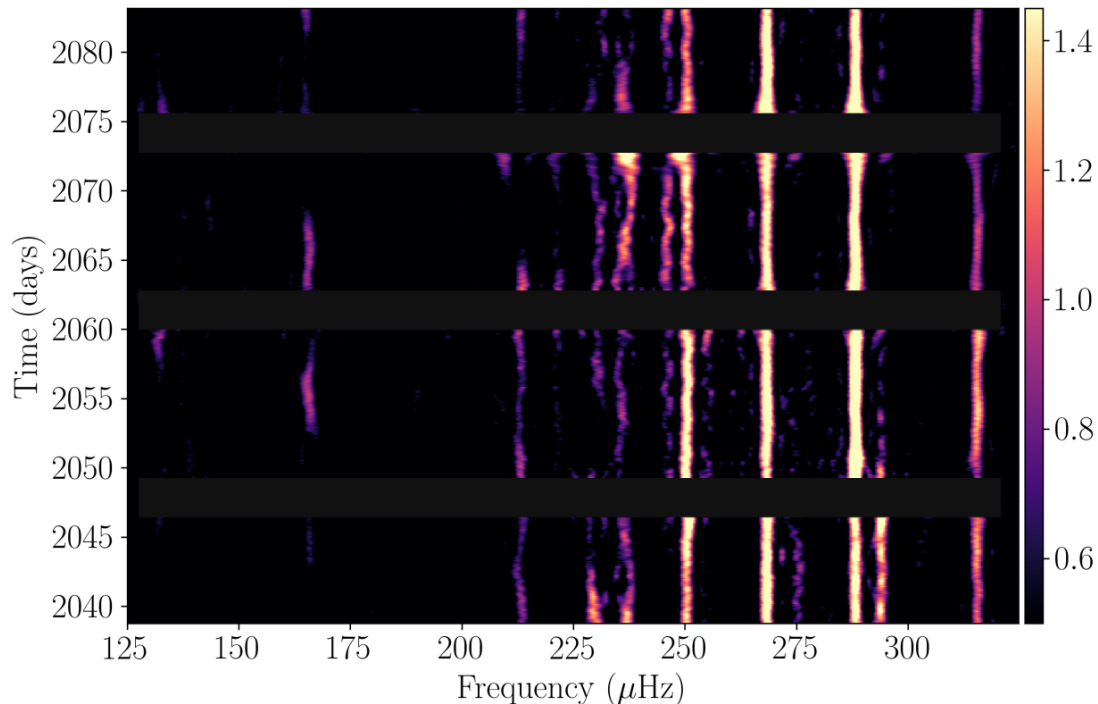


Figure 2.7: Sliding Fourier transform of TIC 260795163 from USC data. The color-scale illustrates amplitude in ppt units. See text for more details on sFT computations.

As this frequency is above the 0.1% FAP level in the FT, we include it in our analysis as well.

We do not find strong evidence of rotational splitting in any of the targets analyzed in this paper, and hence all of them must have considerably longer rotation periods than the length of their TESS dataset. Consequently, any peak we have observed must be considered an unresolved multiplet consisting of a summation of three, for $l = 1$, or more sinusoids with independent phase and amplitude, and with each sinusoid having slightly different unresolved frequency. This produces a beating effect on timescales longer than the analyzed TESS dataset, which then may appear as any form of frequency and/or amplitude variation. Beating of unresolved multiplets is therefore the default cause of any such variations observed in datasets that are too short to reveal rotational splitting.

2.3.4 Asymptotic g-mode period spacing

Fontaine et al. (2003) showed that the oscillation modes detected in long-period pulsating subdwarf B stars are associated with high-order g-modes. In the asymptotic limit, when $n \gg l$ the consecutive radial overtones of high-order g-modes are evenly spaced in period such that the consecutive g-modes follow the equation:

$$P_{l,n} = \frac{\Delta P_0}{\sqrt{l(l+1)}} n + \epsilon_l, \quad (2.1)$$

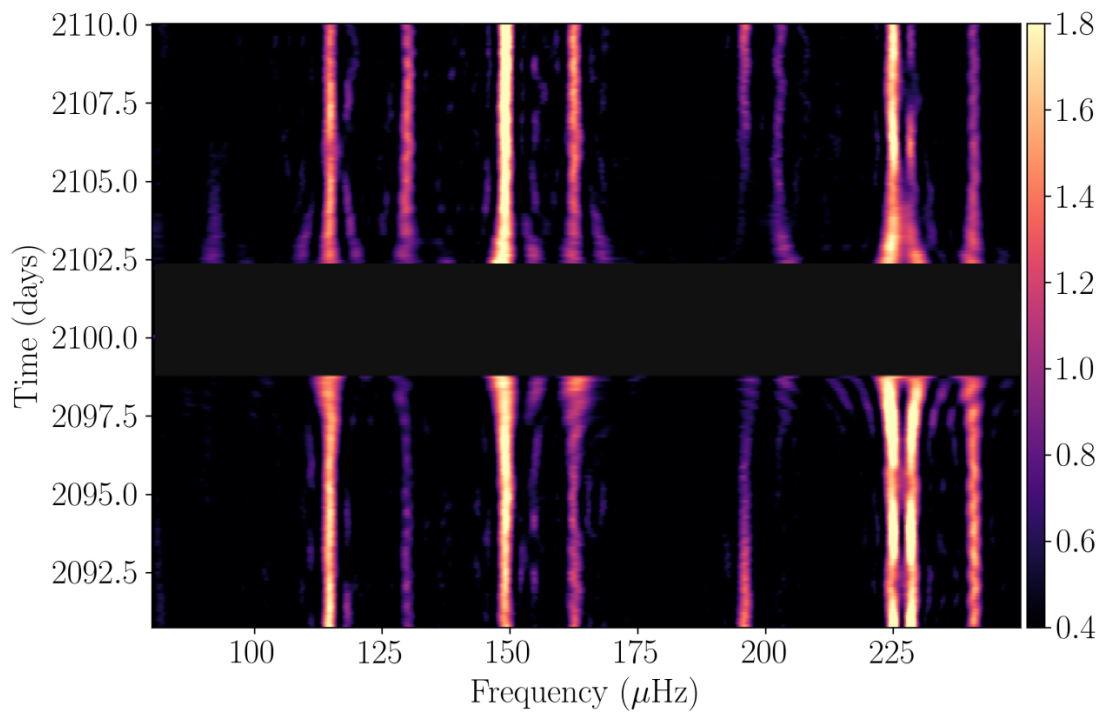


Figure 2.8: Sliding Fourier transform of TIC 080290366. The sFT is calculated from USC data.

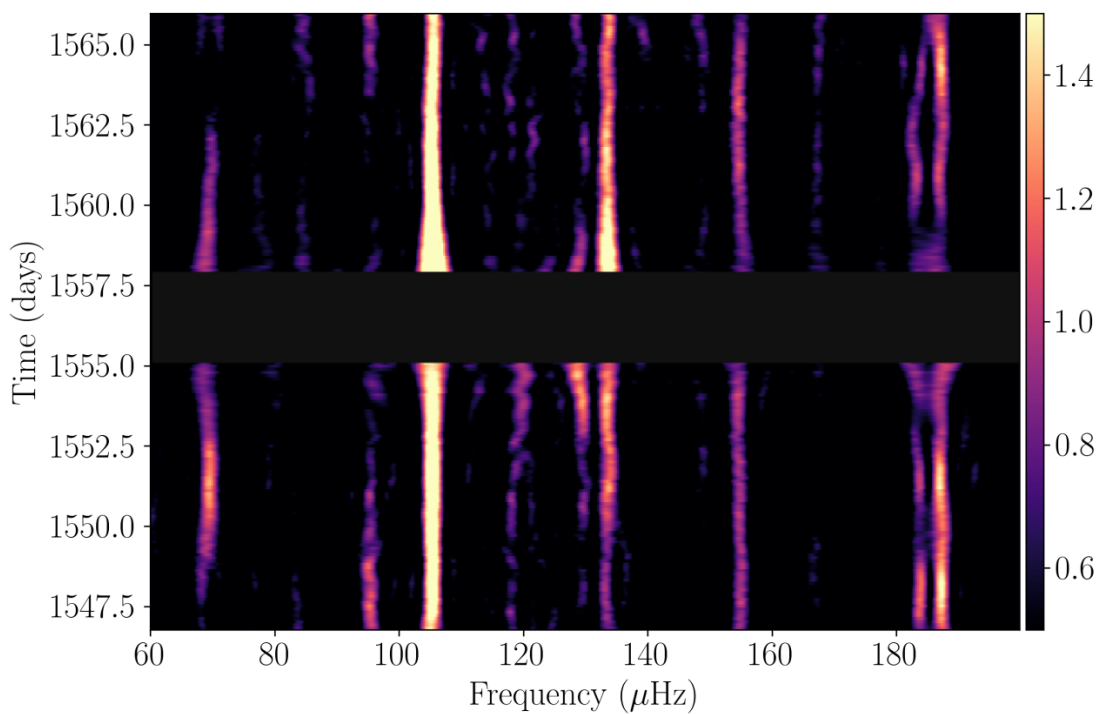


Figure 2.9: As in Fig. 2.8 but for TIC020448010. The sFT is calculated from SC data.

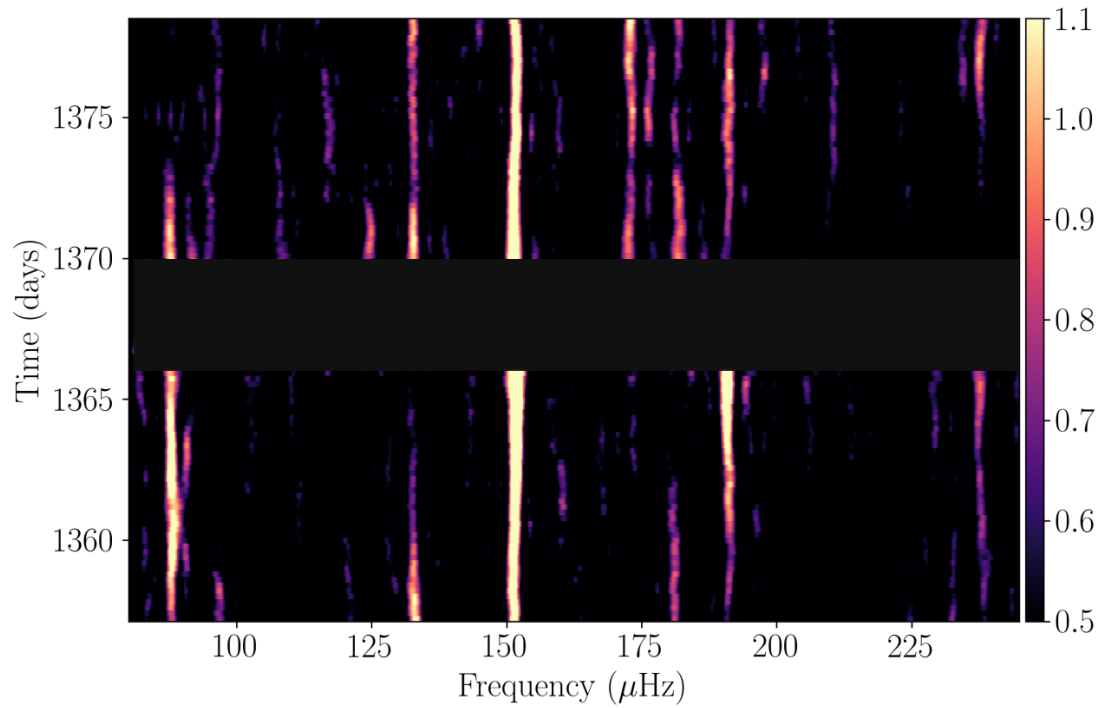


Figure 2.10: The same figure as 2.8 but for TIC 138707823. The sFT is calculated from SC data.

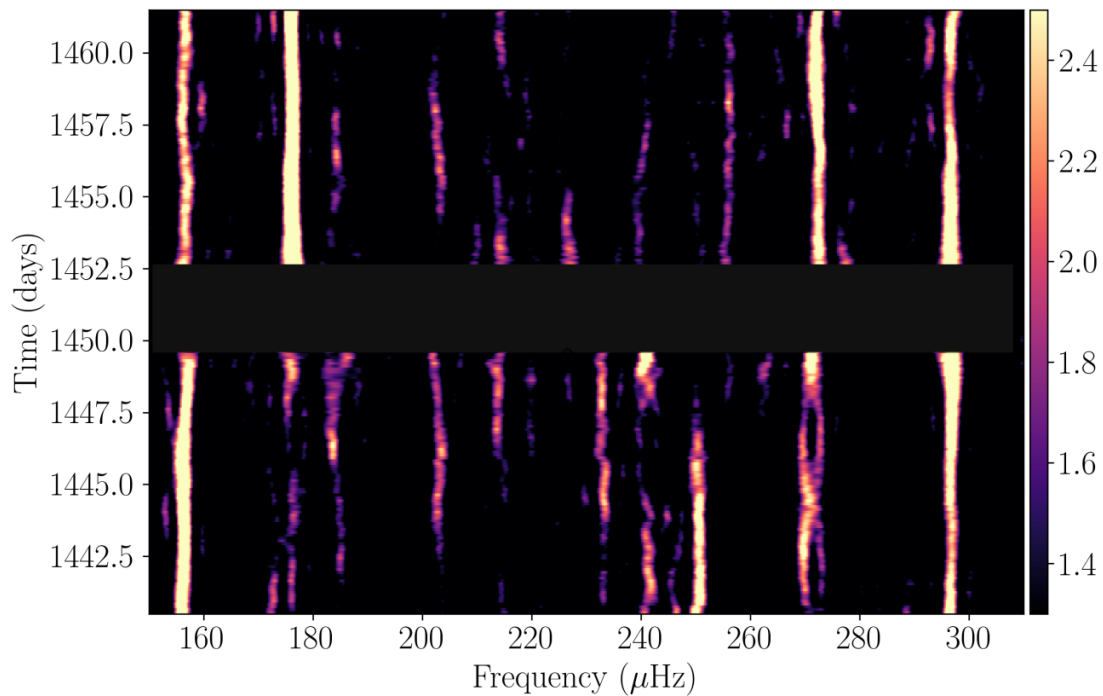


Figure 2.11: As in Fig. 2.8 but for TIC 415339307. The sFT is calculated from SC data.

where ΔP_0 is just the asymptotic period spacing for g-modes, which is defined as $\Delta P_0 \propto [\int_{r_1}^{r_2} \frac{|N|}{r} dr]^{-1}$, N being the Brunt-Väisälä frequency, the critical frequency of nonradial g-modes (Tassoul, 1980), and ϵ_l is a constant (Unno et al., 1979).

The existence of a nearly constant period spacing of g-modes in the asymptotic regime means that we can search for the patterns of modes with a given harmonic degree in the observed period spectra of pulsating stars. This method, referred to as the asymptotic period spacing method, has been used to identify the degree of pulsational modes in many g-mode pulsators such as γ -Dor stars, slowly pulsating B stars (SPBs), and white dwarfs (Aerts, 2019, and references therein).

However, only with the onset of space-based light curves such as those obtained by *Kepler* did it become possible to use this method to identify the degrees of the pulsational modes in sdB stars (Reed et al., 2011, e.g.,). However, this method cannot be used to determine the absolute radial order n of a given mode from the equation (2.1) without detailed modeling. What we can do is choose a relative number for a radial order (n_l) corresponding to a modal degree l such that all other consecutive radial orders for this modal degree have an offset with respect to n_l . The ratio between consecutive overtones is then derived from equation (2.1), such that the ratio for dipole ($l = 1$) and quadrupole ($l = 2$) modes is $\sqrt{3}$. Based on the theoretical models by Charpinet et al. (2000), the period spacing of $l = 1$ modes is around 250 s for sdB pulsators. The *Kepler* and K2 observations of g-mode pulsating sdB stars find that the average period spacing for $l = 1$ modes ranges from 227 s to 276 s (Reed et al., 2018). Recent results from the TESS mission on five g-mode sdB pulsators find similar results, with the average period spacing ranging from 232 s to 268 s (Charpinet et al., 2019; Sahoo et al., 2020a; Reed et al., 2020a). Here, we search for constant period spacing in our five target stars observed by TESS using the Kolmogorov-Smirnov (K-S; Kawaler, 1988a) and the inverse variance (I-V; O'Donoghue, 1994a) significance tests.

In the K-S test, Q is the quantity that defines the probability distribution of observed modes. If the data have a nonrandom distribution in the period spectrum, then the distribution will have a peak at the minimum value of Q . In the I-V test, on the other hand, a maximum of the inverse variance will indicate a consistent period spacing.

In Figure 2.12, we show the K-S (top panel) and I-V (bottom panel) results obtained for the five stars in our sample. For both panels, we applied a vertical, arbitrary offset for visualization purposes. The same color coding is applied for both panels. For all targets, the statistical tests display a clear indication of the mean period spacing at around 250 s. For the case of TIC 260795163 and TIC 080290366, the I-V test is not as conclusive as for the other three stars. However, the K-S test does show an indication of a possible mean period spacing of $l = 1$ at 250 s. Moreover, TIC 260795163 and TIC 080290366 show peaks at around 150 s referring to the possible period spacing of quadrupole modes.

Based on the potential period spacings obtained from the K-S and I-V tests, we search for the sequences of dipole and quadrupole modes in the entire FT of each star. First, we search for

the $l = 1$ and $l = 2$ sequences examining consecutive modes in the period domain of the FT of each star. Given that the higher degree modes are more sensitive to geometrical suppression due to the mode cancellation effect (Aerts et al., 2010), we assume that the highest amplitude frequencies are corresponding to low-degree modes ($l = 1$ and $l = 2$). This assumption is only valid if all the modes have the same intrinsic amplitude. For sdB pulsators, the majority of the detected frequencies have been identified with low-degree modes ($l \leq 2$). However, a few exceptional examples have been reported. For instance, in two sdB pulsators observed during the nominal mission of *Kepler*, the high-degree g-modes were assigned up to $l = 6$ (Kern et al., 2018) or $l = 8$ (Telting et al., 2014) using the method of rotational multiplets. Silvotti et al. (2019) also reported several high-degree modes up to $l = 12$ using solely asymptotic period spacing in the brightest ($V = 10.2$) sdB pulsator HD 4539 (EPIC 220641886) observed during the K2 mission. We proceed in the following way: we assign arbitrary radial orders (n) for each identified l degree and calculate the mean period spacing using a linear regression fit. In this way, we calculated the mean period spacing (ΔP) for all stars and find that the mean period spacing for the $l = 1$ mode ranges from 251 s to 255 s. In order to assess the errors of the mean period spacing obtained in our analysis, we performed a bootstrap resampling analysis as described by Efron (1979); Simpson & Mayer-Hasselwander (1986). We used this method because many possible modes are not detected in the amplitude spectra. Furthermore, in some cases, the individual pulsational period has no unique modal degree solution, and in some specific cases the modes could be altered due to mode trapping.

In order to make a realistic error assignment, we simulated 10^4 datasets from the determined l modes. For each target, we created sets of randomly chosen observed periods that are already identified as $l = 1$ or $l = 2$ modes in order to obtain the mean period spacing from each different subsequence. The same data point can occur multiple times and ordering is not important, such that for N data points the total number of possible different bootstrap samples is $\frac{(2N-1)!}{N!(N-1)!}$ (Andrae, 2010). For instance, for a given dipole sequence consisting of ten modes, the highest possible number of different bootstrapping subsets is about 10^5 . For the five stars analyzed in this paper, we detected dipole sequences that range from 7 to 13 modes depending on the star. Therefore, we restricted ourselves to 10^4 subsets. For each of the subsets that include a series of dipole or quadrupole modes, we derive the mean period spacing with the linear regression fit. The most probable solution is obtained as a mean period spacing (which corresponds to the 50th percentile of the $\Delta P_{l=1}$ distribution). The errors are then estimated as 1σ and given in Table 2.9.

The right panels of Figs. 2.13, 2.14, 2.15, 2.16 and 2.17 show the residuals between the observed periods and the periods derived from the mean period spacing for the $\Delta P_{l=1}$ where we can see the deviation of the modes. The scatter of the residuals for all stars is up to 50 s and for the stars for which more $l = 1$ modes are detected, we notice the oscillatory pattern, which is a characteristic feature that was found in several V1093 Hya-type sdB pulsators (Telting et al., 2012; Baran, 2012, e.g.). Detecting all modes of the $l = 1$ sequence with an expected period

spacing of 250 s (Charpinet et al., 2002) is unlikely as the sdB stars are chemically stratified, which causes the observed modes to be scattered around this value. Such small deviations from the mean period spacing are to be expected in those stars where diffusion processes have had enough time to smooth out the H–He transition zone (Miller Bertolami et al., 2012). On the other hand, the efficiency of trapping diminishes with increasing radial order, as discussed in Charpinet et al. (2014). This is because the local wavelength of the modes decreases with increasing radial order, and therefore the higher order g-modes become less affected by the H–He transition zone. In this way, the higher order g-modes may present an almost constant period spacing even without smoothing the H–He transition zone.

TIC 260795163

The K-S test for TIC 260795163 shows an indication of both dipole and quadrupole modes; see the upper panel of Fig. 2.12. Assuming that the highest amplitude frequency at 288.186 μHz (f_{21} in Table 2.4) is an $l = 1$ mode, then the sequence of $l = 1$ mode is fulfilled with the following frequencies: f_{10} , f_{14} , f_{17} and f_{19} . Beyond 6000 s, six additional frequencies (f_1 to f_6) were found to fit the dipole sequence. The six frequencies f_8 , f_9 , f_{11} , f_{15} , f_{16} , and f_{20} showed consistent period spacing for quadrupole modes with a unique solution. For four frequencies, we cannot find a unique solution, namely f_4 , f_6 , f_{10} , and f_{21} , and they could be interpreted as either $l = 1$ or $l = 2$ modes.

Of the total of 23 periodicities detected in TESS data for TIC 260795163, there were five frequencies that did not fit either $l = 1$ or $l = 2$ sequences. These periodicities could be either higher-degree modes or $l = 1$ and/or $l = 2$ modes which are severely affected by mode trapping and do not fit the $l = 1$ or $l = 2$ patterns. However, without detecting rotational multiplets, it is impossible to test either of the two possibilities. The amplitude spectra of TIC 260795163 with our mode identification are presented in Fig. 2.13. Based on this mode identification, we calculate the mean period spacing of dipole modes, $\Delta P_{l=1} = 254.83_{-2.28}^{+2.14}$ s and quadrupole modes, $\Delta P_{l=2} = 150.51_{-2.28}^{+3.27}$ s.

TIC 080290366

Based on the results from the K-S and I-V tests in which there is a peak at around 255 s indicating a possible $\Delta P_{l=1}$, and also a peak at 155 s indicating a possible $\Delta P_{l=2}$ (see upper and lower panel of Fig. 2.12), we searched for dipole and quadrupole sequences in the FT of TIC 080290366. Starting from the highest amplitude frequency at 149.133 μHz (f_7 in Table 2.5) as an $l = 1$ mode, we find two frequencies that fit the dipole mode sequence, f_8 and f_9 . Beyond 7500 s, there are five frequencies that are also following dipole mode sequences: f_1 , f_2 , f_3 , f_4 , and f_5 . We found only three frequencies that uniquely fit the $l = 2$ sequence. For five frequencies (f_5 , f_8 , f_9 , f_{14} and f_{17}) the solution is degenerate as the frequencies fit both dipole and quadrupole mode sequences. Of the 18 detected frequencies, there are 4 that did not fit dipole or quadrupole mode sequences. These frequencies could be high-order degree modes

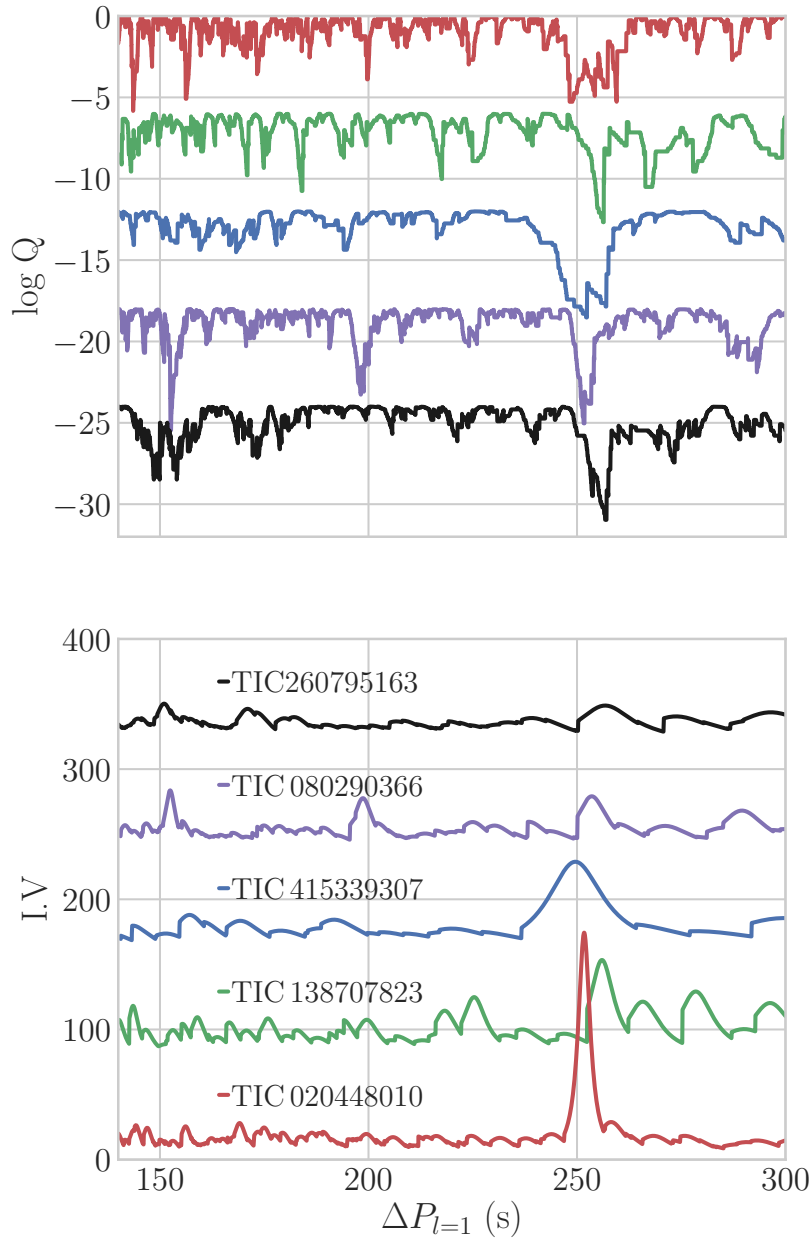


Figure 2.12: Kolmogorov-Smirnov (top panel) and inverse variance (lower panel) tests to search for a constant period spacing in the five stars of our sample. The offset on $\log Q$ for the Kolmogorov-Smirnov is 6 and the offset on y-axis for the inverse variance test is 80. All stars present a significant probability of having a constant period spacing.

Table 2.4: Frequency solution from the *TESS* light curve of TIC 260795163 including frequencies, periods, amplitudes (and their uncertainties), and S/N. Errors are given in parenthesis to 2 significant digits. Identified modal degree and relative radial orders are listed in column 5 and 6, respectively.

ID	Frequency μHz	Period [sec]	Amplitude [ppt]	S/N	l	n
$f_{1\dagger}$	127.915 (20)	7817.63 (1.27)	0.269(44)	4.84	1	30
$f_{2\dagger}$	132.358 (14)	7555.25 (81)	0.394(44)	7.09	1	29
$f_{3\dagger}$	137.178 (16)	7289.77 (85)	0.349(44)	6.28	1	28
f_4	147.752 (36)	6768.08 (1.66)	0.475 (76)	4.75	1/2	26/44
f_5	159.298 (10)	6277.541 (35)	0.26 (43)	4.74	1	24
$f_{6\dagger\dagger}$	165.001 (10)	6060.55 (37)	0.554(44)	9.98	1/2	23/39
$f_{7\dagger}$	166.194 (14)	6017.04 (53)	0.394(45)	7.09		
f_8	207.634 (10)	4816.172 (20)	0.28 (43)	5.17	2	31
$f_{9\dagger\dagger}$	213.093 (08)	4692.77 (18)	0.657(44)	11.83	2	30
$f_{10\dagger}$	221.251 (14)	4519.75 (29)	0.392(44)	7.06	1/2	17/29
$f_{11\dagger}$	228.75 (12)	4371.58 (23)	0.465(44)	8.36	2	28
$f_{12\dagger\dagger}$	230.251 (15)	4343.08 (29)	0.356(44)	6.41		
$f_{13\dagger\dagger}$	231.428 (13)	4320.98 (24)	0.428(44)	7.71		
$f_{14\dagger\dagger}$	235.444 (08)	4247.28 (14)	0.683(44)	12.28	1	16
$f_{15\dagger\dagger}$	237.532 (10)	4209.94 (18)	0.536(44)	9.64	2	27
$f_{16\dagger\dagger}$	245.960 (08)	4065.69 (14)	0.654(44)	11.77	2	26
$f_{17\dagger\dagger}$	250.447 (04)	3992.84 (06)	1.349(44)	24.27	1	15
$f_{18\dagger}$	254.972 (18)	3921.98 (28)	0.308(44)	5.54		
$f_{19\dagger\dagger}$	268.360 (03)	3726.32 (04)	1.624(44)	29.20	1	14
$f_{20\dagger\dagger}$	275.588 (16)	3628.59 (22)	0.335(44)	6.03	2	23
$f_{21\dagger\dagger}$	288.186 (03)	3469.97 (03)	1.716(44)	30.87	1/2	13/22
$f_{22\dagger\dagger}$	293.996 (12)	3401.44 (11)	1.469 (76)	14.70		
$f_{23\dagger\dagger}$	315.537 (05)	3169.19 (05)	1.043(44)	18.77	2	20

†† Frequency and amplitude from sectors 1+27+28.

† Frequency and amplitude from sectors 27+28.

The frequencies that are detected only in sector 1 are unmarked.

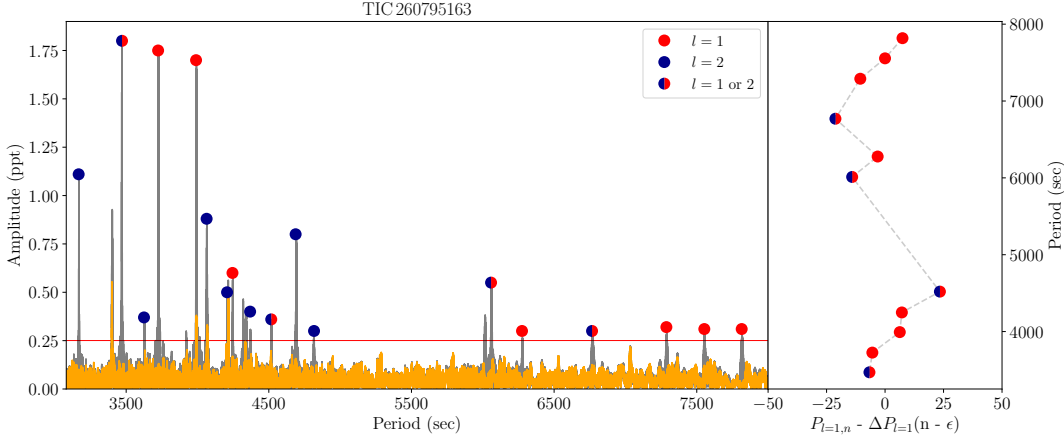


Figure 2.13: Fourier transform of TIC 260795163 (presented here are the sectors 1, 28 and 29 together). The residuals after prewhitening are shown in orange. The red and blue dots show the dipole and quadrupole modes respectively. If there is no unique identification, the period is shown in both colors. The horizontal red line correspond to 0.1% FAP confidence level. The right panel shows the residuals between the observed and the fitted periods. See text for more details on mode identification and the mean period spacing computations.

or trapped modes. The amplitude spectra of TIC 080290366 with our mode identification are presented in Fig. 2.14. Based on the mode identification explained above, we calculated both $\Delta P_{l=1} = 253.32^{+0.78}_{-0.84}$ s and $\Delta P_{l=2} = 154.16^{+2.47}_{-7.97}$ s. The final seismic result for TIC 080290366 and the other stars analyzed in this paper is given in Table 2.9.

TIC 020448010

The K-S and IV tests display a clear indication of a period spacing at 253 s as shown in Fig. 2.12. Starting with the highest amplitude peak at 9 495.5 s (f_5 in Table 2.6), we search for a dipole sequence in the FT. Out of 15 detected frequencies, 12 frequencies uniquely fit the $l = 1$ sequence, while only 2 frequencies can be evaluated as $l = 2$ mode as the difference corresponds to $2 \times \Delta P_{l=2}$. However, one periodicity (at 8778.2 s) does not have a unique solution: it could be either $l = 1$ or $l = 2$ mode.

The amplitude spectra of TIC 020448010 together with the mode identification are presented in Fig. 2.15. Based on our mode identification we calculate the average period spacing for dipole modes, $\Delta P_{l=1} = 251.70^{+0.87}_{-0.96}$ s. In Table 2.9, we also give $\Delta P_{l=2}$ using the ratio between consecutive overtones derived from equation (2.1).

TIC 138707823

The K-S and IV tests show a clear indication of a possible $\Delta P_{l=1}$ at 255 s as can be seen in Fig. 2.12. Assuming the highest peak at 6 600.78 s (f_3) to be an $l = 1$ mode, we find that the dipole

Table 2.5: Frequency solution from the *TESS* light curve of TIC 080290366 including frequencies, periods, and amplitudes (and their uncertainties) and the signal-to-noise ratio. Errors are given in parenthesis to 2 significant digits. Identified modal degree and relative radial orders are listed in column 5 and 6, respectively.

ID	Frequency μHz	Period [sec]	Amplitude [ppt]	S/N	l	n
f_{1++}	81.649 (31)	12247.525 (4.62)	0.412 (53)	6.87	1	47
f_{2+}	90.912 (41)	10999.552 (4.86)	0.313 (53)	5.3	1	42
f_{3+}	114.712 (08)	8717.476 (63)	1.560 (53)	26.00	1	33
f_{4++}	118.217 (28)	8459.017 (2.06)	0.452 (53)	7.54	1	32
f_{5++}	129.967 (13)	7694.241 (78)	0.982 (53)	16.37	1/2	29/48
f_6	141.123 (30)	7086.02 (1.45)	0.390 (52)	6.11	2	44
f_{7++}	149.133 (5)	6705.43 (22)	2.452 (52)	37.02	1	25
f_{8++}	154.754 (24)	6461.854 (1.02)	0.532 (53)	8.87	1/2	24/40
f_{9++}	162.579 (10)	6150.830 (38)	1.266 (53)	21.11	1/2	23/38
f_{10++}	165.129 (10)	6055.88 (62)	1.142 (52)	17.41		
f_{11+}	168.027 (02)	5951.40 (43)	0.371 (53)	5.55		
f_{12++}	195.836 (34)	5106.29 (88)	1.51 (51)	22.98		
f_{13++}	196.144 (11)	5098.29 (30)	1.03 (52)	15.63	2	31
f_{14++}	202.916 (16)	4928.14 (39)	0.737 (52)	11.11	1/2	18/30
f_{15++}	224.994 (07)	4444.544 (14)	1.784 (53)	29.73	2	27
f_{16++}	228.658 (09)	4373.344 (18)	1.392 (54)	23.20		
f_{17++}	240.884 (8)	4151.37 (13)	1.518 (52)	22.93	1/2	15/25
f_{18++}	257.402 (18)	3884.97 (27)	0.635 (51)	9.76	1	14

++ Frequency and amplitude from sectors 2+29.

+ Frequency and amplitude from sector 29.

The frequencies that are detected only in sector 2 are unmarked.

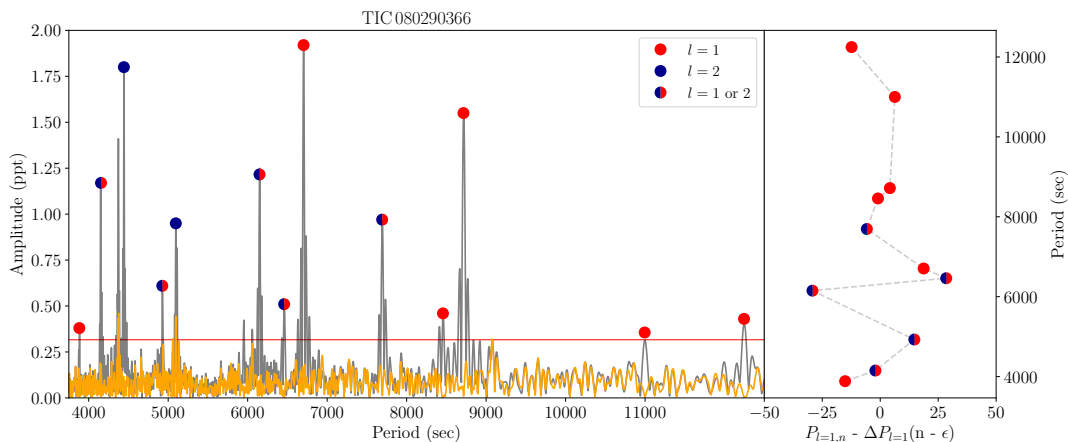


Figure 2.14: Same as Fig. 2.13 but for TIC 080290366 (presented here is sector 29).

Table 2.6: Frequency solution from the *TESS* light curve of TIC 020448010 including frequencies, periods, amplitudes (and their uncertainties), and S/N. Identified modal degree and relative radial orders are listed columns 5 and 6, respectively.

ID	Frequency μHz	Period [sec]	Amplitude [ppt]	S/N	l	n
f_1	68.845(24)	14525.3(5.1)	0.731(7)	8.5	1	56
f_2	70.203(32)	14244.3(6.5)	0.561(7)	6.5	1	55
f_3	83.096(46)	12034.3(6.7)	0.393(7)	4.4	1	46
f_4	95.327(25)	10490.2(2.7)	0.742(7)	8.2	1	40
f_5	105.313(10)	9495.5(9)	1.752(7)	20.4	1	36
f_6	113.918(49)	8778.2(3.7)	0.358(7)	4.2	1/2	33/49
f_7	118.227(28)	8458.3(2.0)	0.615(7)	7.3	2	48
f_8	121.244(39)	8247.8(2.7)	0.442(7)	5.2	1	31
f_9	129.282(27)	7735.0(1.6)	0.677(7)	7.7	1	29
f_{10}	133.516(14)	7489.7(8)	1.260(7)	14.6	1	28
f_{11}	148.722(38)	6724.0(1.7)	0.449(7)	5.3	1	25
f_{12}	154.898(21)	6455.9(9)	0.865(7)	9.8	1	24
f_{13}	167.668(34)	5964.2(1.2)	0.508(7)	6.0	1	22
f_{14}	183.706(22)	5443.5(6)	0.798(7)	9.4	1	20
f_{15}	187.244(16)	5340.64(46)	1.122(7)	12.6		

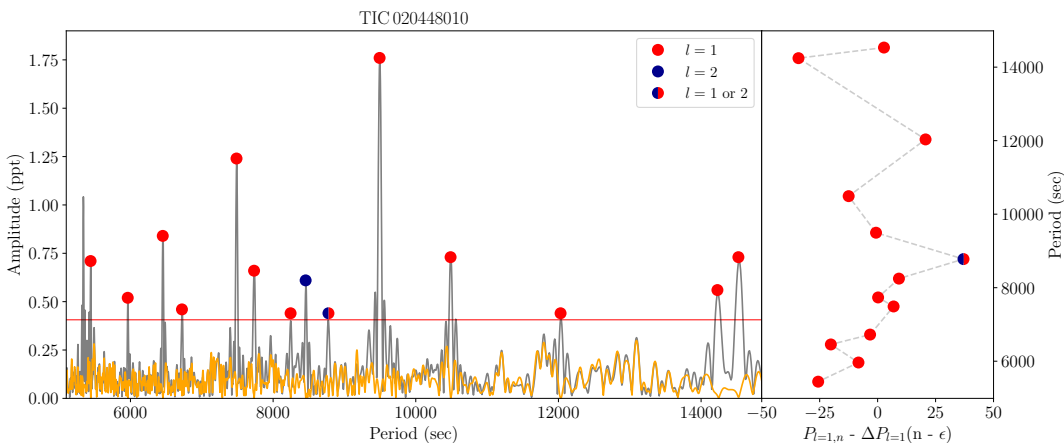


Figure 2.15: Same as Fig. 2.13 but for TIC 020448010 (presented here is sector 9).

Table 2.7: Frequency solution from the *TESS* light curve of TIC 138707823 including frequencies, periods, amplitudes (and their uncertainties), and S/N. Errors are given in parenthesis to 2 significant digits. Identified modal degree and relative radial orders are listed columns 5 and 6, respectively.

ID	Frequency μHz	Period [sec]	Amplitude [ppt]	S/N	l	n
f_1	87.829 (26)	11385.70 (3.33)	0.858 (97)	6.98	1	44
f_2	132.679 (27)	7537.01 (1.51)	0.833 (97)	6.77	1/2	29/45
f_{3++}	151.497 (17)	6600.78 (74)	1.297 (97)	10.55	1	25
f_{4++}	173.099 (29)	5777.02 (97)	0.890 (10)	6.84	1/2	22/33
f_5	181.380 (39)	5513.27 (1.17)	0.576 (98)	4.68	1	21
f_6	191.027 (25)	5234.87 (69)	0.874 (98)	7.11	1	20
f_{7++}	237.895 (32)	4203.52 (57)	0.794 (10)	6.10	1	16

++ Frequency and amplitude from sectors 2+29.

† Frequency and amplitude from sector 29.

The frequencies that are detected only in sector 2 are unmarked.

sequence can be completed with f_4 , f_5 , and f_6 . In the longer period region beyond 6 600 s, there are two more frequencies with the large gap in between that fit the $l = 1$ sequence. We interpreted these two frequencies as $l = 1$ modes and added them to the fitting procedure in order to find the mean period spacing of $\Delta P_{l=1}$. The same case is valid for the shorter period region and between f_6 and f_7 there is a large gap of about 1 000 s (which is four times $\Delta P_{l=1}$). We note that the periodicity (at 6600.78 s) deviates from the mean period spacing significantly. This mode can be interpreted as a candidate trapped mode, but knowledge of where the quadrupole modes are is required in order for us to come to any firm conclusions. The two frequencies f_2 and f_4 could be also interpreted as $l = 2$ modes because three times $\Delta P_{l=1}$ is equal to five times $\Delta P_{l=2}$. If we exclude these two degenerate modes and calculate the average period spacing of $l = 1$, we find $\Delta P_{l=1} = 256.38 \pm 1.43$ s. If we include these two modes and calculate the average period spacing, we find $\Delta P_{l=1} = 256.09^{+6.97}_{-1.21}$ s. We list all modes identified in Table 2.7 and show them in Fig. 2.16.

TIC 415339307

The FT of TIC 415339307 shows that all the frequencies are concentrated in a narrow region between 156 μHz (3 371 s) and 296 μHz (6 399 s) as can be seen in Fig. 2.17. In Fig. 2.12, K-S and I-V tests show signs of a potential average period spacing at 250 s. We identified five dipole modes and two quadrupole modes, while three modes were able to fit both solutions. Between 4 500 s and 6 000 s, there are four frequencies that can only be fitted by a dipole mode sequence. We find that the frequencies f_1 , f_6 , f_8 , and f_{10} also fit the dipole sequence. The frequencies f_7 and f_9 can only be quadrupole modes as the difference between the modes is

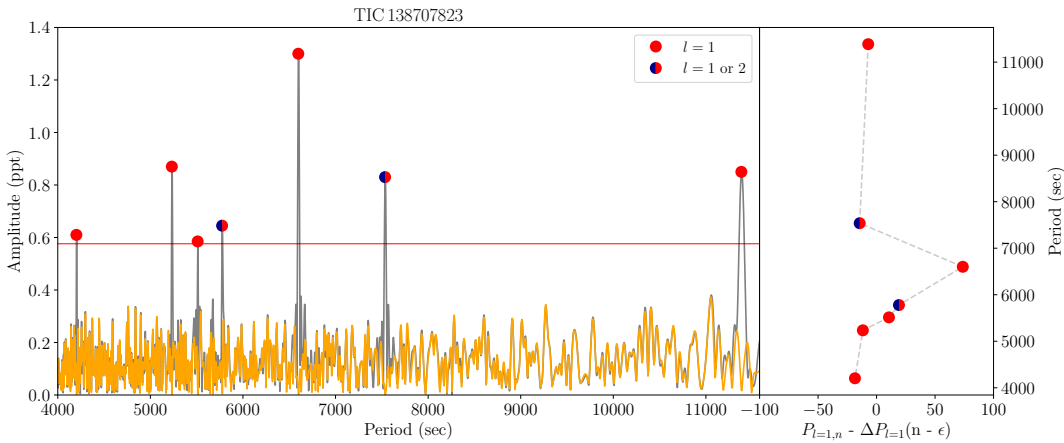


Figure 2.16: Same as Fig. 2.13 but for TIC 138707823 (presented here is sector 2).

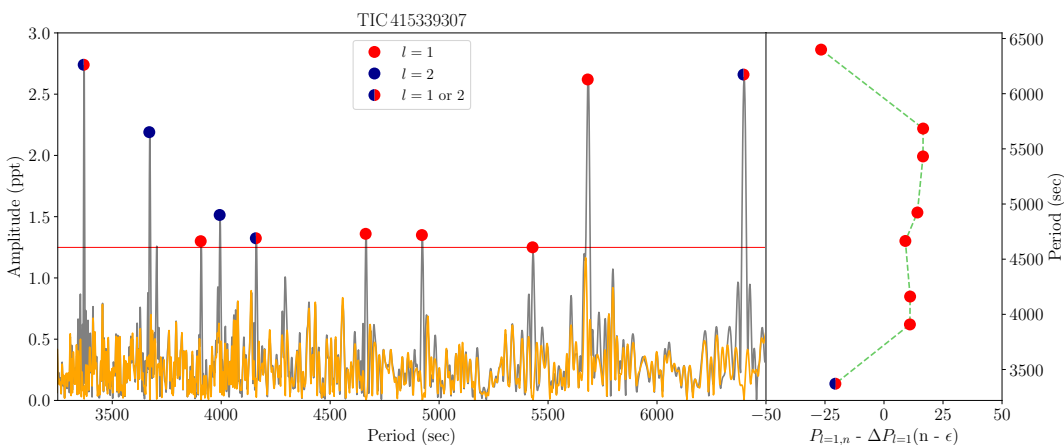


Figure 2.17: Same as Fig. 2.13 but for TIC 415339307 (presented here is sector 5).

around 300 s. The frequencies f_1 , f_6 , and f_{10} can be identified as $l = 2$ modes.

Including all these identified modes, we calculated $\Delta P_{l=1} = 252.84^{+3.30}_{-2.86}$ s and $\Delta P_{l=2} = 151.50^{+6.69}_{-2.06}$ s. We list all identified modes in Table 2.8 and show them in Fig. 2.17.

2.4 Analysis of spectroscopic data

We reduced and analyzed the data from the EFOSC2 spectrograph using standard *PyRAF*⁶ (Science Software Branch at STScI, 2012) procedures. First, we applied bias correction and flat-field correction, and then we removed the pixel-to-pixel sensitivity variations by dividing each pixel with the response function. Subsequently, we applied wavelength calibrations using the

⁶http://www.stsci.edu/institute/software_hardware/pyraf

Table 2.8: Frequency solution from the *TESS* light curve of TIC 415339307 including frequencies, periods, amplitudes (and their uncertainties), and S/N. Identified modal degree and relative radial orders are listed columns 5 and 6, respectively.

ID	Frequency μHz	Period [sec]	Amplitude [ppt]	S/N	l	n
f_1	156.261 (20)	6399.55 (79)	2.661 (21)	9.89	1/2	24/41
f_2	175.929 (19)	5684.11 (63)	2.619 (21)	9.74	1	21
f_3	184.122 (44)	5431.18 (1.26)	1.198 (21)	4.45	1	20
f_4	203.126 (38)	4923.05 (92)	1.346 (21)	5.00	1	18
f_5	214.359 (37)	4665.07 (82)	1.362 (21)	5.06	1	17
f_6	240.309 (36)	4161.31 (67)	1.324 (21)	4.92	1/2	15/26
f_7	250.302 (33)	3995.16 (54)	1.514 (21)	5.63	2	25
f_8	255.863 (34)	3908.34 (60)	1.3 (21)	4.83	1	14
f_9	272.299 (23)	3672.43 (56)	2.188 (21)	8.13	2	23
f_{10}	296.648 (18)	3371.00 (21)	2.736 (21)	10.17	1/2	12/21

Table 2.9: Seismic properties of five pulsating sdB stars studied in this work. Columns 1, 2, 3, 4, 5, 6, and 7 correspond to the *TESS* input catalog number, the number of g-modes extracted from the light curve, the number of identified dipole modes, the number of identified quadrupole modes, the range of radial orders, the average period spacing of dipole modes, and the average period spacing of quadrupole modes, respectively.

TIC	# g	$l = 1$	$l = 2$	n	$\Delta P_{l=1}$	$\Delta P_{l=2}$
260795163	23	11	7	14-44	$254.83^{+2.14}_{-2.28}$	$150.51^{+3.27}_{-2.28}$
080290366	18	11	3	14-48	$253.32^{+0.78}_{-0.84}$	$154.16^{+2.47}_{-7.97}$
020448010	15	14	1	20-56	$251.70^{+0.87}_{-0.96}$	145.32
138707823	7	7	-	16-45	$256.09^{+6.97}_{-1.21}$	147.83
415339307	10	8	2	12-41	$252.84^{+3.30}_{-2.86}$	$151.50^{+6.69}_{-2.06}$

spectra obtained with the internal He-Ar comparison lamp. In a last step, we performed a flux calibration using the standard stars EG 21 and EG 274. The S/N of the final spectra is between 80 and 150 (see Table 5.3).

The data obtained with the B&C spectrograph were reduced in a similar way using *PyRAF*. WE bias subtracted and flat-field corrected all frames, and removed cosmic ray events. Afterwards, we performed a wavelength calibration with calibration spectra taken immediately after target observations. We then corrected all wavelength-calibrated spectra for atmospheric extinction using coefficients provided by *PyRAF*. Finally, we flux calibrated all spectra using the spectrophotometric standard star EG 21. The final spectra have S/N ranging from 70 to 120.

2.5 Spectral analysis with XTGRID

We analyzed all the stars of our sample and derived atmospheric parameters by fitting synthetic spectra to the newly obtained low-resolution spectra. Synthetic spectra were calculated from TLUSTY nonlocal thermodynamic equilibrium stellar atmosphere models (Hubeny & Lanz, 2017) using H and He composition. These models were used in the steepest-descent χ^2 -minimizing fitting procedure XTGRID (Németh et al., 2012) using the web service provided by Astroserver⁷. The iterative procedure starts out from a starting model and by successive corrections converges on the best fit. We applied a convergence limit of 0.5% relative change of all model parameters over three successive iterations. Error bars were calculated by mapping the χ^2 landscape around the best fit until the 3σ confidence limit for the given degree of freedom was reached. The error calculations are performed in one dimension for the He abundance, but include the correlations between surface temperature and gravity.

Figure 2.18 shows the new observations together with their best-fit TLUSTY/XTGRID models and Table 2.10 lists the atmospheric parameters. The sample is very homogeneous, all spectra in Figure 2.18 are dominated by Balmer-lines and only weak He I lines are seen. This together with the Balmer-decrement suggest that the stars must have very similar atmospheric parameters, which is in agreement with earlier observations suggesting that sdBVs stars (g-mode pulsators) form a compact group on the EHB. However, the spectral analysis reveals a systematic difference between the parameters derived from EFOSC2 and B&C data. The poor blue coverage of the NTT/EFOSC2 wavelength calibration lamp results in serious flexure along the dispersion axis and causes discrepancies in fitting. For completeness, we include all results in Table 2.10. Where B&C spectra are available, we consider them superior in quality and the results from B&C data as final.

Among the stars analyzed in this paper, there is a confirmed binary system TIC 138707823. Figure 2.18 shows that TIC 138707823 has a clean sdB spectrum without any significant optical contribution from a companion. This confirms earlier results (Edelmann et al., 2005; Geier &

⁷<https://xtgrid.astroserver.org>

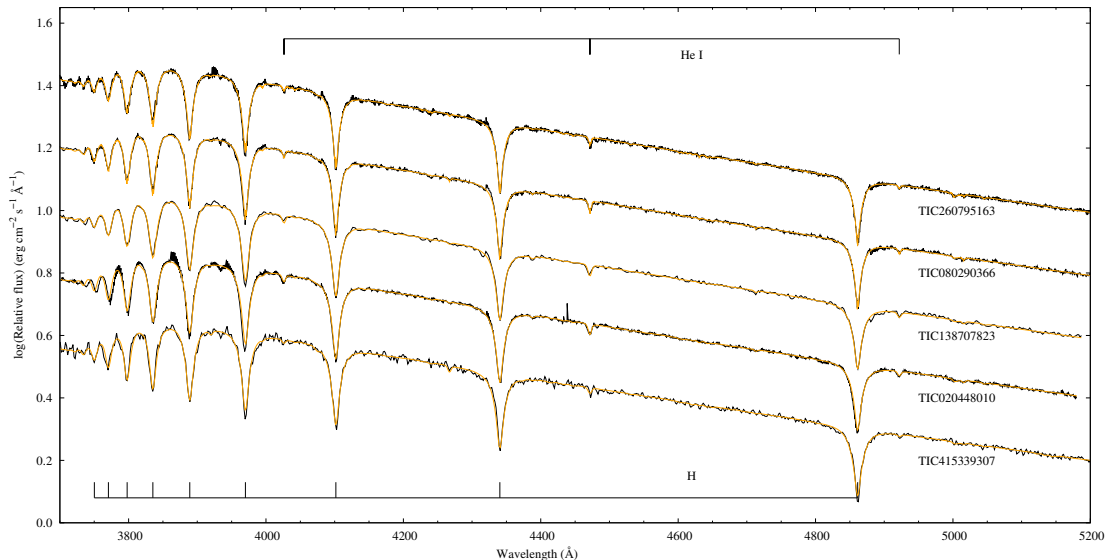


Figure 2.18: Best-fit TLUSTY/XTGRID models for the five hot subdwarf stars analyzed in this paper. The spectra are dominated by the H Balmer-series marked at the bottom and a few weak He I lines marked at the top of the figure. The observed continua adjusted to the theoretical models.

(Heber, 2012) that the companion is a compact object, most likely a WD.

2.6 Asteroseismic models

A proper asteroseismic interpretation of the observed frequencies found in g-mode sdB pulsators requires the computation of oscillations in stellar models (Charpinet et al., 2000, 2002). To this end, we computed stellar evolution models with the LPCODE stellar evolution code (Althaus et al., 2005a), and computed $l = 1$ g-mode frequencies with the adiabatic nonradial pulsation code LP-PUL (Córscico & Althaus, 2006a). Opacities, nuclear reaction rates, thermal neutrino emission, and equation of state are adopted as in Miller Bertolami (2016) and Moehler et al. (2019). In particular, it is worth noting that atomic diffusion was not included in the present computations. Diffusion is expected to reduce mode-trapping features in the latter stages of the He-core burning phase (Miller Bertolami et al., 2012). In the present work we aim to compare the model predictions with observations on a global level by means of a robust indicator such as the mean period spacing (ΔP), leaving detailed period-to-period comparisons of individual stars for future work. As such, we expect trapping features to play no important role in the comparisons. SdB models were constructed from an initially $M_i = 1M_\odot$ ZAMS model with $Z_{\text{ZAMS}} = 0.02$, and $Y = 0.245 + 2 \times Z$, as in Miller Bertolami (2016). Mass loss was artificially enhanced prior to the He-core flash in order to produce sdB models during the core-He-burning stage in the T_{eff} range of g-mode sdB pulsators. The resulting models at

Table 2.10: Spectroscopic results of five sdBV stars analyzed in this paper. The errors are 3σ statistical errors. Systematic differences exist between parameters from different instruments. Where available, B&C observations are adopted. The final parameters are marked with bold font.

TIC	Spectrograph	Sp. Type	T_{eff} (K)	$\log g$ (cm s^{-2})	$\log (n_{\text{He}}/n_{\text{H}})$
260795163	B&C	sdB	27600 (± 460)	5.37 (± 0.08)	-2.76 (± 0.02)
260795163	EFOSC2	sdB	26260 (± 550)	5.12 (± 0.09)	-2.80 (± 0.09)
080290366	B&C	sdB	26310 (± 410)	5.30 (± 0.05)	-2.61 (± 0.08)
080290366	EFOSC2	sdB	25770 (± 380)	5.21 (± 0.06)	-2.69 (± 0.06)
138707823	B&C	sdB+WD	24800 (± 310)	5.49 (± 0.06)	-2.57 (± 0.05)
138707823	EFOSC2	sdB+WD	26310 (± 330)	5.37 (± 0.08)	-2.53 (± 0.07)
020448010	EFOSC2	sdB	23720 (± 480)	5.45 (± 0.08)	-2.57 (± 0.52)
415339307	B&C	sdB	25920 (± 530)	5.44 (± 0.10)	-3.00 (± 0.03)

the beginning of the He-core-burning stage have masses of $M_{\text{ZAHB}} = 0.46738, 0.4675, 0.468, 0.469, 0.47, \text{ and } 0.473 M_{\odot}$. For the sake of comparison, models during the He-core-burning stage were computed under two different assumptions regarding convective boundary mixing (CBM): one is the extreme assumption of a strict Schwarzschild criterion (Schwarzschild, 1906) at the convective core, and the other corresponds to the inclusion of CBM at the boundary of the convective core. In the latter case, CBM is adopted as an exponentially decaying velocity field following Freytag et al. (1996) and Herwig et al. (1997), with free parameters taken as in Miller Bertolami (2016). This corresponds to the assumption of a moderate CBM (see section 3.1 in De Gerónimo et al., 2019). It is worth noting that although strong theoretical arguments indicate that the strict Schwarzschild criterion is not physically sound, it serves as a useful estimation of the smallest possible convective core size (Castellani et al., 1971, 1985; Gabriel et al., 2014). The value of ΔP was computed from the periods of individual $l = 1$ g-modes in the range 2000 s—10000 s, which is a typical range for the periods observed in V1093 Her stars. The computed value of ΔP shows oscillations due to two completely separate factors. On one hand, as the models evolve, structural changes push different periods inside or outside the range in which we computed ΔP , leading to small fluctuations in the value of ΔP . For the sake of clarity, in Fig. 2.19 we show its time-averaged value in a moving window of 3 Myr. The variance around the mean value is shown by the confidence bands in the bottom right panel of Fig. 2.19. On the other hand, larger fluctuations occurring on longer timescales also appear in the sequences that include moderate CBM due to the oscillating behavior of the

boundary of the convective core.

The two sets of sdB models are shown in Fig. 2.19 together with the properties observed in the V1093 Her stars studied in the present and previous works. From Fig. 2.19, it becomes apparent that models with a small convective core close to those predicted by a strict Schwarzschild criterion, are too compact (and consequently too dim) to fit the surface gravities observed in known pulsators. This is reinforced by the comparison between the evolution of the mean period spacing ($\overline{\Delta P_\ell}$) against $\log g$ and $\log T_{\text{eff}}$ in Fig. 2.19. Models with small convective cores give mean period spacings that are too small to account for the observations. On the contrary, models with a moderate CMB prescription are able to reach the range of mean period spacings observed in V1093 Her stars (Fig. 2.19). The reason for this is two fold, and can be understood by looking at the expression of the asymptotic mean period spacing ΔP_ℓ^a ,

$$\Delta P_\ell^a = \frac{P_o}{\sqrt{\ell(\ell+1)}} = \frac{2\pi^2}{\sqrt{\ell(\ell+1)}} \left[\int_{r_1}^{r_2} \frac{N}{r} dr \right]^{-1}. \quad (2.2)$$

The buoyancy (Brunt-Väisälä) frequency for an ideal monoatomic gas with radiation can be written as

$$N^2 = g^2 \frac{\mu(4-3\beta)}{\mathfrak{R}T} \left[\nabla_{\text{ad}} - \nabla + \frac{\beta \nabla_\mu}{4-3\beta} \right], \quad (2.3)$$

where, in the case of sdB stars, radiation pressure is almost negligible and $\beta \sim 1$. We see that period spacing, in general, scales as $\Delta P \propto \bar{g}^{-1} R_\star / (R_\star - R_{\text{core}})$. As models that include CBM have cores that grow larger than those using a strict Schwarzschild criterion, the g-mode propagation cavity (of size $\sim R_\star - R_{\text{core}}$) is reduced and leads to larger values of the period spacings. This is why models that include CBM show oscillations in the value of ΔP , as those models show oscillations in the size of the convective core (see Fig. 2.19). In addition, models with larger convective cores are able to increase the mean molecular weight of the star to larger values than their small convective core counterparts. This leads to greater luminosities in the sdB models that include CBM, and consequently to smaller surface gravities for the same effective temperature. The decrease in the mean value of the local surface gravity then also leads to an increase in the period spacing of the models. Finally, close to the end of the He-core burning stage, sdB models with CBM develop one of more breathing pulse instabilities (Castellani et al., 1985). This creates the loops in the $\log g - \log T_{\text{eff}}$ diagram at relatively low gravities and leads to an extension of the He-core-burning lifetime.

From the previous discussion it is apparent that small convective cores close to those predicted by a bare Schwarzschild criterion can be discarded on the basis of the observations. This is in agreement with theoretical arguments (Castellani et al., 1985; Gabriel et al., 2014) as well as with independent observational constraints (Charpinet et al., 2011; Bossini et al., 2015; Constantino et al., 2015, 2016). Although models with a moderate CBM prescription at the burning core cover the range of observed period spacings, closer inspection shows that observed mean period spacings are about 10 to 20 s larger (~ 5 to 10%) than those predicted by the models. Such a shift could be attained by a small increase in the size of the convective core.

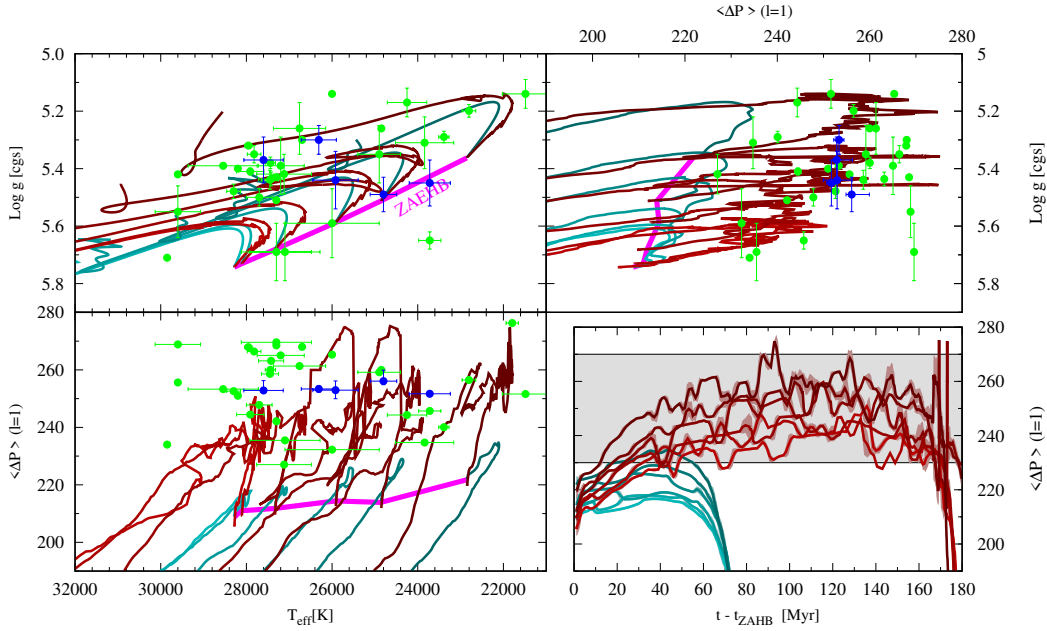


Figure 2.19: Properties of the two sets of stellar evolution models discussed in the text as compared with those observed in pulsating sdB stars. Blue circles indicate the stars studied in this work while green circles indicate those from previous studies (Reed et al., 2018; Charpinet et al., 2019; Reed et al., 2020a; Sahoo et al., 2020a). Red tracks correspond to models computed with a moderate CBM prescription while cyan tracks correspond to those computed under the extreme assumption of a strict Schwarzschild criterion. Masses of the models are $M_{\text{ZAHB}} = 0.467, 0.4675, 0.468, \text{ and } 0.47 M_{\odot}$, and darker colors correspond to more massive models. Thick magenta lines show the locus of the model at the zero-age extreme horizontal branch (ZAEHB). Light-colored bands around the curves in the bottom right panel indicate the typical variance of ΔP around the mean value.

The consequent small decrease in the surface gravity of the models would still be in agreement with observations.

2.7 Summary and conclusions

Here, we present the analysis of data collected for five pulsating hot subdwarf B stars, TIC 260795163, TIC 080290366, TIC 020448010, TIC 138707823, and TIC 415339307, observed with the TESS mission. Of the five analyzed stars, four are new detections of long-period pulsating sdB (V1093 Her) stars, namely TIC 260795163, TIC 020448010, TIC 138707823, and TIC 415339307. This high-duty cycle space photometry delivered by the TESS mission provides data of excellent quality with which to detect and identify the modes in long-period sdBV stars.

The pulsations detected in these five stars are concentrated in the short frequency region from ~ 70 to ~ 300 μHz , which is in line with what was discovered during the second half of the survey phase of *Kepler* (Baran et al., 2011). We detected 73 oscillation frequencies which we associate with g-modes in sdBVs. We did not find any p-modes for any of the targets. With the 120-second observations, it is difficult to find p-modes because we are limited to a Nyquist frequency of about $4\,200$ μHz . However, we did not find any p-modes either in the 20-second data for TIC 260795163, TIC 080290366, and TIC 138707823, even though the Nyquist frequency for that data set is about $25\,000$ μHz . This might imply that the analyzed stars are most likely pure g-mode sdB pulsators.

We analyzed the data using the asteroseismic methods of rotational multiplets and asymptotic period spacing in order to identify pulsational modes. Although we detect many pulsation frequencies, we do not find evidence for complete rotational multiplets in any of the analyzed stars. Relying solely on asymptotic period spacing relationships, we identify the observed periods as mainly dipole and quadrupole g-modes.

We constructed sFTs to examine the temporal evolution of the pulsation modes. None of the pulsation spectra or sFTs for any of the analyzed stars show a clear pattern indicating rotational multiplets. Moreover, the highest signal-to-noise frequencies seem to be stable over the course of these TESS observations (from 25 to 49 days). However, the low-amplitude frequencies do show complex patterns in their sFTs.

For the 5 V1093 Her stars analyzed in this paper, namely TIC 260795163, TIC 080290366, TIC 020448010, TIC 138707823, and TIC 415339307, we identified 49 frequencies out of the 73 detected ones as $l = 1$ modes using solely asymptotic period spacing. In some cases, we were not able to identify the modes with a unique modal degree. We mention that for 15 periodicities, we do not find a unique identification, and therefore these can be interpreted as either $l = 1$ or $l = 2$ modes. We apply the method of bootstrapping with 10^4 times randomization in order to calculate the mean period spacing obtained in our analysis and also to assess the errors. The mean period spacing for $l = 1$ modes obtained in this way for the five analyzed stars ranges from 251 s to 255 s, while the average period spacing for $l = 2$ modes spans from 145 s to 155 s.

We derived atmospheric parameters for all five stars by fitting synthetic spectra to the newly obtained low-resolution Dupont/B&C and NTT/EFOOSC2 spectra. The effective temperatures of the observed sdB stars span from 23 700 K to 27 600 K and their surface gravity ($\log g$) is in the range from 5.3 to 5.5 dex, confirming that they are indeed occupying the g-mode sdBV parameter space.

We computed stellar evolution models with LPCODE stellar evolution code (Althaus et al., 2005a), and computed $l = 1$ g-mode frequencies with the adiabatic nonradial pulsation code LP-PUL (Córscico & Althaus, 2006a). We compared the derived mean period spacings (ΔP) of dipole g-modes derived from TESS observations for the five sdBV stars of our sample and 33 found in the literature with the predictions of the adiabatic pulsation computations performed

on stellar evolutionary models. In agreement with expectations from theoretical arguments and previous asteroseismological works (Castellani et al., 1985; Gabriel et al., 2014; Charpinet et al., 2011; Bossini et al., 2015; Constantino et al., 2015; Schindler et al., 2015), and recently (Ostrowski et al., 2021), we find that models relying on a simplistic implementation of the Schwarzschild criterion lead to small convective cores and values of ΔP which are too low to match the observations. On the contrary, models with a standard treatment of convective boundary mixing at the convective core are able to match the observed values of ΔP , although more intense convective boundary mixing cannot be discarded.

We did not attempt to constrain envelope properties for any of the targets analyzed in this work for the following reasons. First, we did not detect any p-modes. Although lower order g-modes are sensitive to envelope properties, a model fit of the observed periods is required, as was done by (Charpinet et al., 2019), which is beyond the scope of this paper. Second, we did not detect any trapped modes either, which can be used to investigate the envelope by identifying the period spacing between the trapped modes.

Pulsating hydrogen-deficient white dwarfs: Discovery of two new GW Vir stars TIC333432673 and TIC095332541

This chapter was originally published as:

A&A 655, A27 (2021)
<https://doi.org/10.1051/0004-6361/202141253>
 © ESO 2021

**Astronomy
&
Astrophysics**

Pulsating hydrogen-deficient white dwarfs and pre-white dwarfs observed with TESS

II. Discovery of two new GW Vir stars: TIC 333432673 and TIC 095332541

M. Uzundag^{1,2}, A. H. Córscico^{3,4}, S. O. Kepler⁵, L. G. Althaus^{3,4}, K. Werner⁶, N. Reindl⁷, K. J. Bell^{8*}, M. Higgins⁹, G. O. da Rosa⁵, M. Vučković¹, and A. Istrate¹⁰

Author contributions: Murat Uzundag performed the majority of the analysis presented in this chapter with guidance and discussions with Alejandro H. Córscico, S. O. Kepler and Maja Vučković. Murat Uzundag carried out the light curve analyses as well as frequency solutions. The tests related to the results were performed by Murat Uzundag and Alejandro H. Córscico. Alejandro H. Córscico computed stellar evolution models using the LPCODE stellar evolution code and determined the masses of each target. The spectroscopic observations for the southern hemisphere and the data reduction were made by Murat Uzundag. The spectroscopic observations for the northern hemisphere was made by Alina Istrate. Klaus Werner and Nicole Reindl carried out a spectral fitting using Tübingen model atmosphere models. Keaton J. Bell, Michael Higgins and Gabriela O. da Rosa were involved the investigation of the flux contamination from the other stars in the field of view of TESS. The text was written by Murat Uzundag and Alejandro H. Córscico and all co-authors provided useful discussion and feedback throughout the whole process.

ABSTRACT

Context. The Transiting Exoplanet Survey Satellite TESS mission is revolutionizing the blossoming area of asteroseismology, particularly of pulsating white dwarfs and pre-white dwarfs, thus continuing the impulse of its predecessor, the Kepler mission.

Aims. In this paper, we present the observations from the extended TESS mission in both 120 s short-cadence and 20 s ultra-short-cadence mode of two pre-white dwarf stars showing hydrogen deficiency. We identify them as two new GW Vir stars, TIC 333432673 and TIC 095332541. We apply the tools of asteroseismology with the aim of deriving their structural parameters and seismological distances.

Methods. We carried out a spectroscopic analysis and a spectral fitting of TIC 333432673 and TIC 095332541. We also processed and analyzed the high-precision TESS photometric light curves of the two target stars, and derived their oscillation frequencies. We performed an asteroseismological analysis of these stars on the basis of PG 1159 evolutionary models that take into account the complete evolution of the progenitor stars. We searched for patterns of uniform period spacings in order to constrain the stellar mass of the stars. We employed the individual observed periods to search for a representative seismological model.

Results. The analysis of the TESS light curves of TIC 333432673 and TIC 095332541 reveals the presence of several oscillations with periods ranging from 350 to 500 s associated to typical gravity (g)-modes. From follow-up ground-based spectroscopy, we find that both stars have a similar effective temperature ($T_{\text{eff}} = 120,000 \pm 10,000$ K) and surface gravity ($\log g = 7.5 \pm 0.5$), but a different He/C composition of their atmosphere. On the basis of PG 1159 evolutionary tracks, we derived a spectroscopic mass of $M_{\star} = 0.58^{+0.16}_{-0.08} M_{\odot}$ for both stars. Our asteroseismological analysis of TIC 333432673 allowed us to find a constant period spacing compatible with a stellar mass $M_{\star} \sim 0.60 - 0.61 M_{\odot}$, and an asteroseismological model for this star with a stellar mass $M_{\star} = 0.589 \pm 0.020 M_{\odot}$, as well as a seismological distance of $d = 459^{+188}_{-156}$ pc. For this star, we find an excellent agreement between the different methods to infer the stellar mass, and also between the seismological distance and that measured with Gaia ($d_{\text{Gaia}} = 389^{+5.6}_{-5.2}$ pc). For TIC 095332541, we have found a possible period spacing that suggests a stellar mass of $M_{\star} \sim 0.55 - 0.57 M_{\odot}$. Unfortunately, we have not been able to find an asteroseismological model for this star.

Conclusion. Using the high-quality data collected by the TESS space mission and follow-up spectroscopy, we have been able to discover and characterize two new GW Vir stars. The TESS mission is having, and will continue to have, an unprecedented impact on the area of white-dwarf asteroseismology.

3.1 Introduction

Asteroseismology of WDs and pre-WDs has been strongly promoted during the last decade mainly by the availability of space missions that provide unprecedented high-quality data. Particularly, the Kepler satellite, both the main mission (Borucki et al., 2010b) and the K2 mode

(Howell et al., 2014), allowed the study of 32 ZZ Ceti stars and two V777 Her stars (Østensen et al., 2011a; Greiss et al., 2014; Hermes et al., 2014; Bell et al., 2015; Hermes et al., 2017b,c; Bell et al., 2017; Córscico, 2020), until it was out of operation by October 2018. The successor of Kepler is the Transiting Exoplanet Survey Satellite (TESS, Ricker et al., 2015b). TESS has provided extensive photometric observations of the 200 000 brightest stars in 85 % of the sky in the first part of the mission, each observation with a time base of about 27 days per sector observed. In the context of pulsating WDs and pre-WDs, the high-quality observations of TESS, combined with ground-based observations, are able to provide a very important input to the asteroseismology of DBVs (Bell et al., 2019; Bognár et al., 2021), DAVs (Bognár et al., 2020), pre-ELMVs (Wang et al., 2020; Hong et al., 2021), and GW Vir stars (Córscico et al., 2021a).

In this work, we report for the first time the photometric variability of the PG1159 stars TIC 333432673 (WD J064115.64-134123.77) and TIC 095332541 (WD J060244.99-135103.57) observed with TESS. Given the small number of already known pulsating stars of this class (20 objects; see Córscico et al., 2019; Sowicka et al., 2021a), the discovery of two new GW Vir stars constitutes a particularly relevant finding, even more so since the Kepler / K2 mission publications do not include any new object of this nature to date. We perform an asteroseismological analysis of these stars based on the state-of-the-art evolutionary models of PG 1159 stars of Althaus et al. (2005b) and Miller Bertolami & Althaus (2006). This study is the second part of a series of papers devoted to the study of pulsating H-deficient WDs observed with TESS. The first article was devoted to a set of six already known GW Vir stars (Córscico et al., 2021a).

The paper is organized as follows. In Sect. 3.2, we present the details of the spectroscopic observations and the data reduction. In Sect. 3.3, we derive atmospheric parameters for each star by fitting synthetic spectra to the newly obtained low-resolution spectra. In Sect. 3.4, we analyse the photometric TESS data and give details on the frequency analysis. Sect. 3.5 is devoted to the asteroseismic analysis of our targets. Finally, in Sect. 3.6, we summarize our main results.

3.2 Spectroscopy

TIC 333432673 (WD J064115.64-134123.77) and TIC 095332541 (WD J060244.99-135103.57) were classified as white dwarf candidates by Gentile Fusillo et al. (2019) from their colors and *Gaia* DR2 parallax. The *Gaia* DR3 parallax and corresponding distance for TIC 333432673 are $\pi = 2.57^{+0.07}_{-0.04}$ mas and $d = 389.00^{+5.59}_{-5.22}$ pc, while for TIC 095332541 are $\pi = 2.60^{+0.07}_{-0.04}$ mas and $d = 384.48^{+5.54}_{-5.04}$ pc (Bailer-Jones et al., 2021), respectively. We obtained spectroscopic observations for TIC 333432673 and TIC 095332541, to determine the atmospheric parameters.

TIC 333432673 was observed with the Southern Astrophysical Research (SOAR) Telescope, a 4.1-meter aperture optical and near-infrared telescope (Clemens et al., 2004), situated at Cerro Pachón, Chile on March 5, 2021 (under the program allocated by the Chilean Time Allocation Committee (CNTAC), no:CN2020B-74). We use Goodman spectrograph with a setup of

Table 3.1: Log of spectroscopic observations including TESS and WD catalogs numbers, right ascension, declination, exposure times, signal-to-noise ratio at 4200 Å and the name of the spectrograph.

TIC	Name	RA (J2000)	Dec (J2000)	Exp. (sec)	S/N (at 4200 Å)	Inst.
333432673	WD ¹	06:41:15.88	-13:41:31.31	450	80	GOODMAN
095332541	WD ²	06:02:45.00	-13:51:03.50	2x1800	80	IDS

1: WD J064115.64–134123.77

2: WD J060244.99–135103.57

4001/mm grating with the blaze wavelength 5500 Å (M1: 3000-7050 Å) with a slit of 1 arcsec. This setup provides a resolution of about 5.6 Å. The data reduction has been partially done by using the instrument pipeline¹ including overscan, trim, slit trim, bias and flat corrections. For cosmic rays identification and removal, we used an algorithm as described by Pych (2004), which is embedded in the pipeline. Then, we applied the wavelength calibrations using the frames obtained with the internal He-Ar-Ne comparison lamp at the same telescope position as the targets. In a last step, we normalized the spectrum with a high-order Legendre function, using the standard star EG 274 observed with the same setup. The signal to noise ratio of the final spectrum is around 80 at 4200 Å with 450 s exposure time.

TIC 095332541 was observed with the Isaac Newton Telescope (INT), a 2.54 m (100 in) optical telescope run by the Isaac Newton Group of Telescopes at Roque de los Muchachos Observatory on La Palma on February 15 and 16, 2021 (ProgID: ING.NL.21A.003) with an exposure time of 1800 s, respectively. We used the Intermediate Dispersion Spectrograph (IDS) long-slit spectrograph with the grating R400V ($R = 1452$) and a 1.5 arcsec slit. This setup provides a resolution of about 3.5 Å. Bias and flat field corrections were applied to the data, the wavelength calibration was performed with Cu-Ne-Ar calibration lamp spectra. We did not flux calibrate the spectra. The signal-to-noise ratio (S/N) of the final spectra is around 80 (see Table 3.1).

3.3 Spectral fitting

The spectra of both stars exhibit lines exclusively from He II and C IV. Oxygen, which is usually the most abundant element after He and C in PG1159 stars, and nitrogen, which is found as trace element in some PG1159 stars, might be detectable in spectra of better resolution and signal-to-noise ratio. There are no hints of the presence of hydrogen in the spectra.

¹https://github.com/soar-telescope/goodman_pipeline

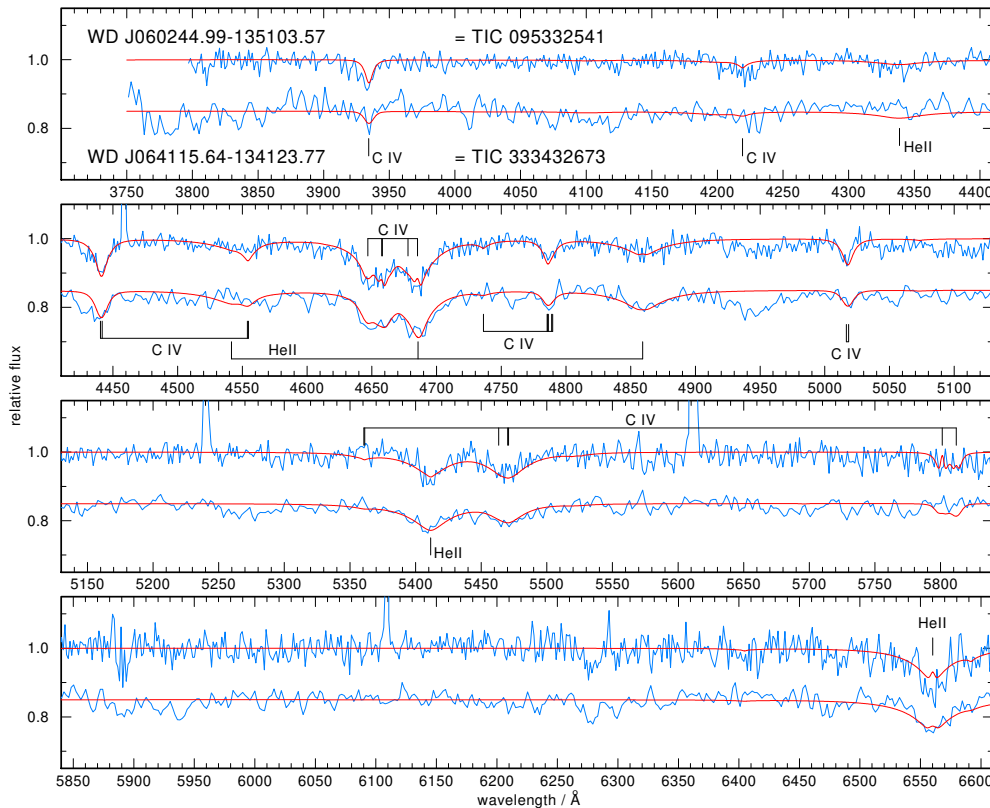


Figure 3.1: Optical spectra of the two new GW Vir stars. Overplotted are the best-fit models. Identifications of He II and C IV lines are marked.

For the spectral analysis, we used a grid of line-blanketed non-local thermodynamic equilibrium (non-LTE) model atmospheres consisting of H, He, and C as introduced by Werner et al. (2014). In essence, it spans $T_{\text{eff}} = 60,000\text{--}140,000$ K in effective temperature and $\log g = 4.8\text{--}8.3$ in surface gravity, with steps of 5,000 K or 10,000 K and 0.3 dex, respectively. C/He mass ratios in the range 0.0–1.0 were considered, namely C/He = 0.0, 0.03, 0.09, 0.33, 0.77, and 1.0. Synthetic spectra were convolved with a Gaussian accounting for the spectral resolution of the observations. The best fitting models were chosen by visual comparison with the rectified observed spectra.

The model fits are displayed in Fig. 4.1. Both stars have $T_{\text{eff}} = 120,000 \pm 10,000$ K and $\log g = 7.5 \pm 0.5$, but a different atmospheric composition. For TIC 095332541, we found He = $0.50^{+0.20}_{-0.05}$ and C = $0.50^{+0.05}_{-0.20}$ and for TIC 333432673, we measured He = $0.75^{+0.05}_{-0.15}$ and C = $0.25^{+0.15}_{-0.05}$ (mass fractions).

3.4 Photometric observations — TESS

We investigate for variability of the two new PG 1159 stars by examining their high-precision photometric observations obtained with TESS. TIC 333432673 was observed with 120 s cadence

mode, while TIC 095332541 was observed with both 120 s and 20 s cadence modes in Sector 33, between 2020-Dec-17 and 2021-Jan-13. We downloaded the data from the “Barbara A. Mikulski Archive for Space Telescopes” (MAST)². We downloaded the target pixel files (TPFs) of both targets from the MAST archive with the Python package `lightkurve` (Lightkurve Collaboration et al., 2018). The TPFs are examined to determine the amount of crowding and other potential bright sources near the target. The contamination factor is indicated with the keyword `CROWDSAP`, which gives the ratio of the target flux to the total flux in the TESS aperture. For each target, we have checked the contamination by looking at the `CROWDSAP` parameter which is listed in Table 3.2. In the case of TIC 095332541 the `CROWDSAP` value is about 0.8, which implies that $\sim 20\%$ of the total flux measured in the TESS aperture comes from other unresolved sources. We have checked for the nearby targets and their brightness. We found 3 nearby objects to TIC 095332541 within 25 arcsec (based on *Gaia* measurements) with G_{mag} of 19.5, 20.78 and 20.76. As the differences in magnitude between TIC 095332541 and the nearby objects are larger than 4, we safely confirm that the variation comes from the PG 1159 star. In addition, these nearby objects are beyond the detection limit of TESS.

In the case of TIC 333432673, the `CROWDSAP` value is around 0.15, which means that more than 80% of the flux in the TESS aperture comes from the other blended sources. As the contamination from the nearby targets is non-negligible, we considered the proximity and brightness of nearby *Gaia* sources that could contaminate the photometric aperture. In Fig. 3.2, we show the field of view of TESS for TIC 333432673 with the aperture mask. Within the aperture mask that we used to extract the photometry, four other objects along with TIC 333432673 are located. Two of them are fainter than $G_{mag} = 18$ (circles 2 and 5), and thus it is not possible to detect any variation from them with TESS. However, the other two targets (circles 3 and 4) are relatively bright, with G_{mag} of 14.7 and 16.4. The origin of the signals has been found using a locator code (Higgins & Bell, in prep.) that produces a light curve and computes its Fourier transform for each pixel in the star’s Target Pixel File (TPF). Then it compares the amplitudes and locates the pixel where each signal period has the highest amplitude. We find that the location of maximum power from the four highest signals in Table 3.3 is most consistent with the position of the PG 1159 source (*Gaia* source_id 2950907725113997312).

The data are in the FITS format which includes all the photometric information, which have been already processed with the Pre-Search Data Conditioning Pipeline (Jenkins et al., 2016) to remove common instrumental trends. From the FITS file, first we have extracted times in barycentric corrected Julian days (“BJD - 245700”), and fluxes (“PDCSAP FLUX”). Afterwards, we removed outliers by applying a running 5σ clipping mask. The fluxes were then normalized by the mean flux.

The final light curves of the target stars are shown in Fig. 3.3. After detrending the light curves, we calculated their Fourier transforms (FTs) to search for periodic signals. The FT of the resulting light curves are shown in Fig. 3.4. For pre-whitening, we employed a nonlinear

²<http://archive.stsci.edu>

least square (NLLS) method, by simultaneously fitting each pulsation frequency above the 0.1% false-alarm probability (FAP), calculated randomizing the light curve 1000 times and measuring the highest peaks in their Fourier transforms. This iterative process has been done starting with the highest amplitude peak, until there is no peak that appears above 0.1% FAP significance threshold. All prewhitened frequencies for both targets are given in Table 3.3 and 3.4 including frequencies (periods) and amplitudes with their corresponding errors and the S/N ratio.

In the case of TIC 333432673, we detected 6 peaks, which are located between 2000 μHz and 3000 μHz . Two frequencies at 2015.393 and 2194.806 μHz show significant residuals. For these unresolved peaks, we did not produce an NLLS fit to extract from the light curves as they can be due to either photon-count noise caused by contamination of the background light in the aperture or amplitude, frequency and/or phase variations over the length of the data. The frequencies of 2013.329 and 2015.393 μHz can be considered as a rotationally split dipole mode. If we assume that a central azimuthal component ($m = 0$) is missing, then the rotation period of TIC 333432673 would be 5.6 d. If one of the side components ($m = +1$ or -1) is missing, then the rotation period of TIC 333432673 would be 2.8 d.

In the case of TIC 095332541, we identified 6 frequencies in the 120 s short-cadence (SC) data, while we detected 7 frequencies in 20 s ultra-short-cadence (USC) data. The frequencies that located in a similar region as TIC 333432673, between 2200 and 2900 μHz as can be seen in Fig. 3.4. In table 3.4, we present the frequency solution that is derived from the USC observations. All frequencies except 2403.783 μHz (f_4) were found in the FT of SC data as well. The amplitudes of frequencies that were extracted from USC observations are about 2% higher than the amplitudes of the SC observations. This effect can be seen in the lower panel of Fig. 3.4, where we depicted FT of USC data (orange lines) and the FT of SC data (black lines). We found a doublet for TIC 095332541 as well at 2401.602 and 2403.783 μHz . Again, if we assume that this pattern is due to rotational multiplets, then the rotation period of TIC 095332541 would be either 2.65 d (in case of either $m = +1$ or -1 is missing) or 5.3 d (in case of a central azimuthal component $m = 0$ is missing).

The periodicities detected in these two PG 1159 stars are concentrated in a short region from 350 s to 500 s, which agree with the period spectrum typically exhibited by pulsating PG 1159 or GW Vir stars (e.g., McGraw et al., 1979; Winget et al., 1991; Costa et al., 2008; Córscico et al., 2021a). Due to the absence of evidence of any nebulae, these two GW Vir stars are classified as DOV stars.

Table 3.2: The two new GW Vir stars reported from TESS observations, including the name of the targets, Gaia magnitude, observed sectors, date, *CROWDSAP* estimate, and length of the runs (columns 1, 2, 3, 4, 5 and 6, respectively).

Name	G_{mag}	Obs. Sector	Start Time (BJD-2 457 000)	<i>CROWDSAP</i>	Length [d]	R μHz	AN [ppt]	0.1% FAP [ppt]
TIC 333432673	15.66	33	2201.7372	0.14	25.83	0.45	0.95	3.67
TIC 095332541	15.79	33	2201.7373	0.78	25.83	0.45	0.71	3.06

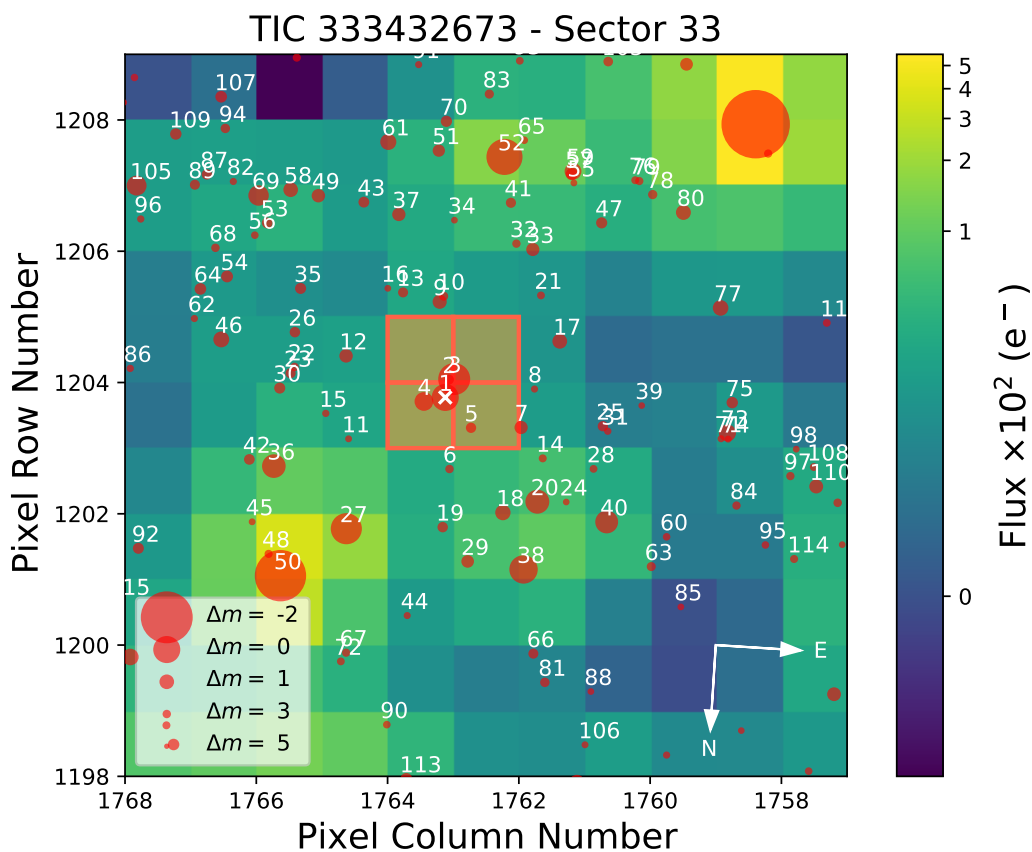


Figure 3.2: Target pixel file (TPF) of TIC 333432673 (created with *tpfplogger*, Aller et al. 2020). The aperture mask used by the pipeline to extract the photometry is overplotted with shaded red square. The size of the red circles indicates the Gaia magnitudes of all nearby stars and TIC 333432673 (circle 1 is marked with a cross).

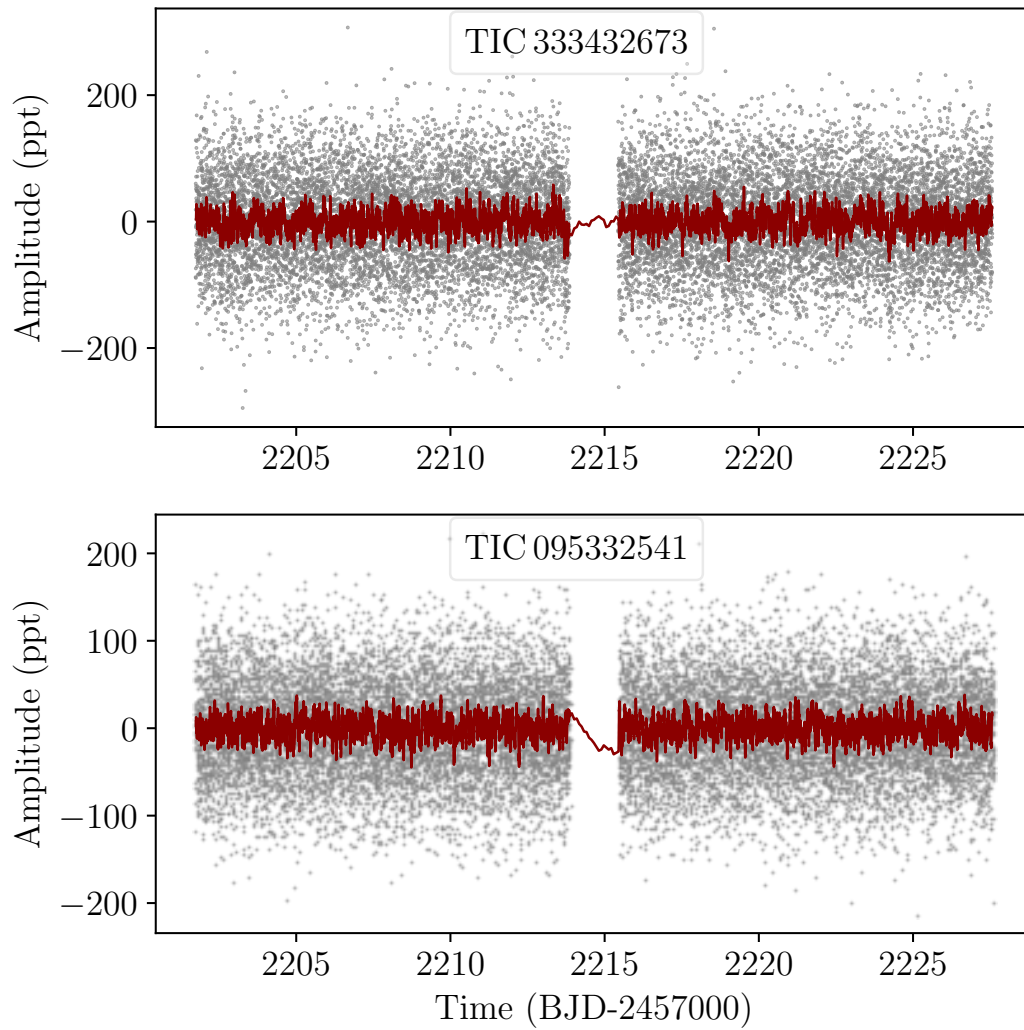


Figure 3.3: The light curves of the new pulsating DOV stars TIC 333432673 (upper panel) and TIC 095332541 (lower panel). The red lines are binned light curves which are calculated by running mean every 20 points (corresponding to 38 minutes).

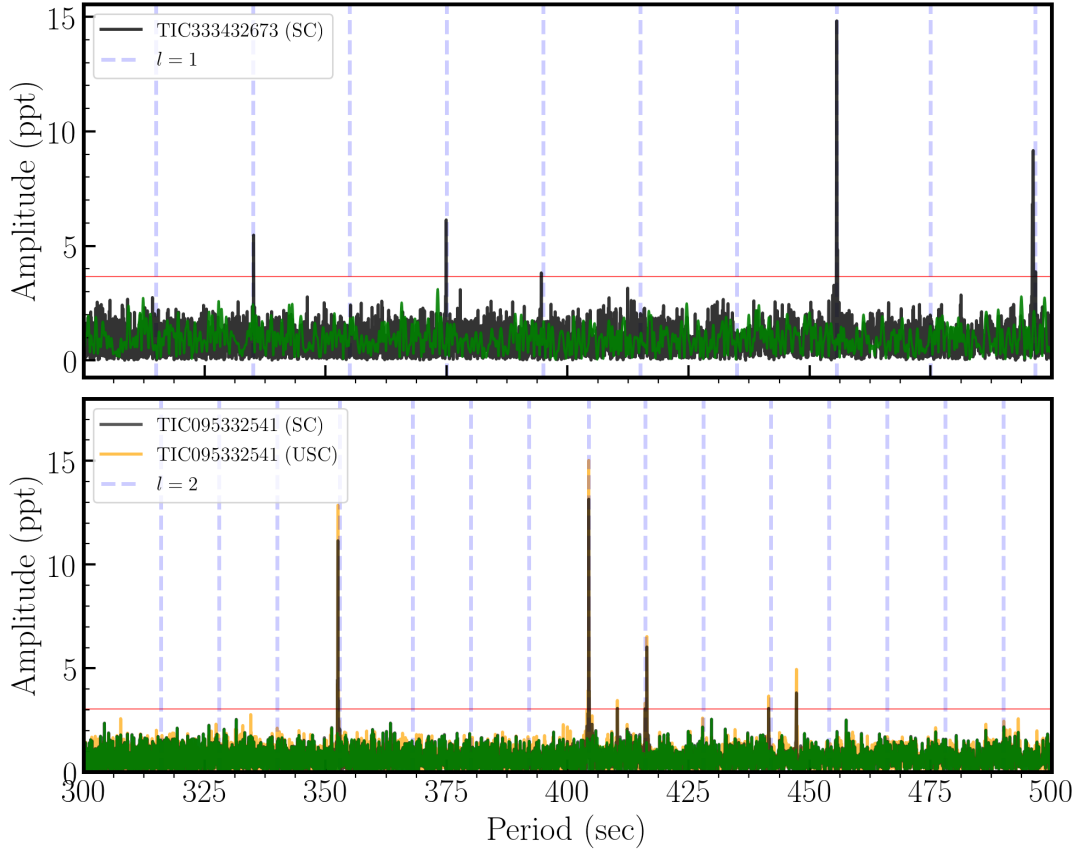


Figure 3.4: Pulsation spectrum in period of the new pulsating DOV stars TIC 333432673 (upper panel) and TIC 095332541 (lower panel). For TIC 095332541, we overplotted the Fourier Transform of both 120 s data (black) and 20 s (orange). The horizontal red line indicates the 0.1% false-alarm probability (FAP) level. In green we depict the FT of the prewhitened light curve. The blue vertical dashed lines indicate the expected locations of $\ell = 1$ modes for TIC 333432673 and $\ell = 2$ modes for TIC 095332541 from the asymptotic pulsation theory described in Section 3.5.2.

Table 3.3: Independent frequencies, periods, and amplitudes, their uncertainties, and the signal-to-noise ratio in the data of TIC 333432673.

Peak	ν (μHz)	Π (s)	A (ppt)	S/N
f_1	2013.329 (44)	496.689 (10)	4.155 (75)	4.38
f_2	2015.393 (23)	496.181 (05)	8.718 (77)	9.19
f_3	2194.806 (15)	455.621 (03)	15.819 (80)	16.68
f_4	2534.342 (47)	394.579 (07)	3.829 (75)	4.03
f_5	2667.136 (29)	374.933 (04)	6.143 (75)	6.48
f_6	2983.709 (33)	335.153 (03)	5.478 (75)	5.77

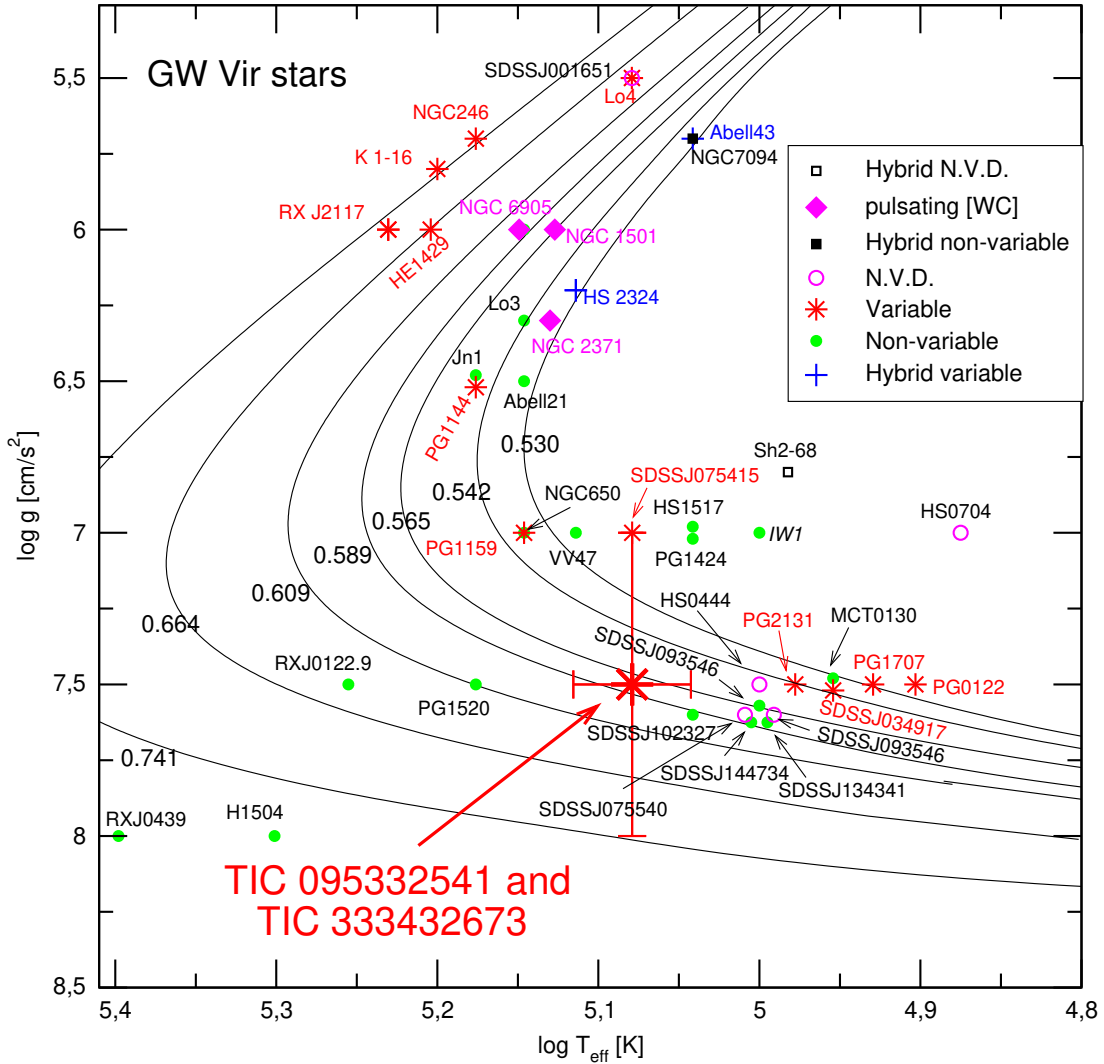


Figure 3.5: The already known variable and non-variable PG 1159 stars and variable [WCE] stars in the $\log T_{\text{eff}} - \log g$ plane. Thin solid curves show the post-born again evolutionary tracks from Miller Bertolami & Althaus (2006) for different stellar masses. "N.V.D." stands for PG 1159 stars with no variability data. "Hybrid" refers to PG 1159 stars exhibiting H in their atmospheres. The location of the two new GW Vir stars TIC 333432673 and TIC 095332541 is emphasized with a large red star symbol with error bars. Both stars share the same spectroscopic surface parameters, $T_{\text{eff}} = 120\,000 \pm 10\,000$ K and $\log g = 7.5 \pm 0.5$.

Table 3.4: Independent frequencies, periods, and amplitudes, their uncertainties, and the signal-to-noise ratio in the data of TIC 095332541.

Peak	ν (μHz)	Π (s)	A (ppt)	S/N
f_1	2235.669 (27)	447.293 (55)	4.975 (57)	7.10
f_2	2264.722 (37)	441.555 (72)	3.675 (57)	5.25
f_3	2401.602 (21)	416.389 (37)	6.447 (57)	9.21
f_4	2403.783 (44)	416.011 (77)	3.105 (57)	4.43
f_5	2437.256 (38)	410.298 (64)	3.578 (57)	5.11
f_6	2472.863 (09)	404.390 (15)	15.119 (57)	21.59
f_7	2836.338 (11)	352.567 (13)	12.856 (57)	18.36

3.5 Asteroseismology

3.5.1 Spectroscopic mass

For the asteroseismological analysis of this work, we employ the set of state-of-the-art evolutionary models of PG 1159 stars of Althaus et al. (2005b) and Miller Bertolami & Althaus (2006, 2007a,b). In those works, a set of post-AGB evolutionary sequences computed with the LPCODE evolutionary code (Althaus et al., 2005b) were followed through the very late thermal pulse (VLTP) and the resulting born-again episode that give rise to the H-deficient, He-, C- and O-rich composition characteristic of PG 1159 stars. The masses of the resulting remnant models are 0.530, 0.542, 0.565, 0.589, 0.609, 0.664, and $0.741M_{\odot}$. In Fig. 4.2 we show the evolutionary tracks of PG 1159 stars in the $\log T_{\text{eff}}$ vs. $\log g$ plane. In Table 3.5 we show the values of the stellar mass, the mass of the envelope, and the surface chemical abundances by mass of ^4He , ^{12}C , and ^{16}O for the evolutionary sequences employed in this study. M_{env} is defined as the mass external to the location of the O/C/He chemical transition region. Since this chemical transition has a finite width (see Fig. 3.10), we consider the location of the interface as the point at which the He abundance has reduced to half of its surface abundance. We note that, in this work, element diffusion was neglected. This is motivated by theoretical expectations that residual weak winds and radiative acceleration retard the gravitational settling of He until the surface gravity reaches a value between $\log g = 7.5$ and 8 (see Unglaub & Bues, 2000). For a $0.529M_{\odot}$ PG 1159 model, this occurs by $T_{\text{eff}} = 65\,000$ K. At higher T_{eff} , the abundances of CNO elements remain nearly unchanged.

We emphasize the need of evolutionary models derived from the full computation of the late thermal pulse to perform seismological studies of PG 1159 stars. Such models provide realistic predictions of the internal chemical stratification and a correct assessment of the evolutionary time scales during the PG 1159 regime, where He shell burning is the main source of energy. The set of PG 1159 sequences we use in this work reproduces the spread in surface

Table 3.5: Stellar mass (in solar units), surface gravity, envelope mass, and the surface chemical abundances by mass for the evolutionary sequences considered in this work. The values correspond to models with $\log(T_{\text{eff}}) = 5.1$ (K) at the stages before the evolutionary knee, that is, the maximum effective temperature possible (see Fig. 4.2).

M_{\star}/M_{\odot}	$\log g$ (cgs)	$\log(M_{\text{env}}/M_{\star})$	X_{He}	X_{C}	X_{O}
0.530	6.120	-1.18	0.33	0.39	0.17
0.542	5.944	-1.22	0.28	0.41	0.21
0.565	5.853	-1.34	0.39	0.27	0.22
0.589	5.780	-1.40	0.31	0.38	0.23
0.609	5.677	-1.51	0.50	0.35	0.10
0.664	5.541	-1.86	0.47	0.33	0.13
0.741	5.417	-2.00	0.48	0.34	0.14

chemical composition observed in PG 1159 stars, the short born-again time of post born again objects, and the location of the GW Vir instability strip, see Córscico et al. (2006); Althaus et al. (2010b). During the very late thermal pulse, an outward-growing convection zone driven by the He-burning shell develops and reaches the H-rich envelope. As a result, most of the H content of the remnant is violently burned in the He-flash convection zone. After this short-lived evolutionary stage, during which the remnant returns from the hot white dwarf stage to the red giant state, evolution proceeds to the domain of PG 1159 stars with a H-deficient surface composition rich in He, C and O. The interplay between mixing and burning during the late thermal pulse creates large quantities of ^{13}C and ^{14}N . The role of such isotopes is by no means negligible since during the PG 1159 regime, α captures by ^{13}C affect the shape of the O profile at the base of the He, C, O envelope (see Fig. 3.10).

On the basis of the evolutionary tracks and the values of the spectroscopic surface gravity and effective temperature of TIC 333432673 and TIC 095332541, we derive by interpolation a value of the spectroscopic mass. We obtained a stellar mass of $M_{\star} = 0.58_{-0.08}^{+0.16} M_{\odot}$ for both GW Vir stars. The large uncertainties of the spectroscopic mass come mainly from the uncertainties in the surface gravity.

3.5.2 Mean period spacing of TIC 333432673

In the asymptotic limit of stellar pulsations, that is for large radial orders ($k \gg \ell$), g modes of consecutive radial order in WDs and pre-WDs are approximately uniformly spaced in period (Tassoul et al., 1990). The asymptotic period spacing is given by $\Delta\Pi_{\ell}^{\text{a}} = \Pi_0 / \sqrt{\ell(\ell+1)}$, Π_0 being a constant defined as $\Pi_0 = 2\pi^2 \left[\int_{r_1}^{r_2} \frac{N}{r} dr \right]^{-1}$, where N is the Brunt-Väisälä frequency (see, e.g., Unno et al., 1989, for its definition). This asymptotic formula constitutes a very precise description of the pulsational properties of chemically homogeneous stellar models.

However, the g -mode period spacings in chemically stratified PG 1159 stars show appreciable departures from uniformity caused by the mechanical resonance called “mode trapping” (Kawaler & Bradley, 1994). The observed average period spacing of GW Vir stars primarily depends on the stellar mass and the effective temperature (Kawaler & Bradley, 1994). It allows us to estimate M_* by fixing T_{eff} . Specifically, a way to derive an estimate of the stellar mass is by comparing the observed average period spacing ($\Delta\Pi$) of the target star with the asymptotic period spacing ($\Delta\Pi_\ell^a$) computed at the effective temperature of the star (see the pioneer works of Kawaler, 1987, 1988b). Since GW Vir stars generally do not have all of their pulsation modes in the asymptotic regime, there is usually no perfect agreement between $\Delta\Pi$ and $\Delta\Pi_\ell^a$. A variation of this approach is to compare $\Delta\Pi$ with the average of the computed period spacings ($\overline{\Delta\Pi_k}$), instead the asymptotic period spacing.

We searched for a constant period spacing in the data of the new GW Vir stars using the Kolmogorov-Smirnov (K-S; Kawaler, 1988b), the inverse variance (I-V; O’Donoghue, 1994b), and the Fourier Transform (F-T; Handler et al., 1997) significance tests. In Fig. 3.6 we show the results of applying these tests to the set of 6 periods of TIC 333432673 (Table 3.3). A very strong signature of a period spacing of ~ 20 s is evident according to the three tests. There is also an indication of a possible period spacing of ~ 40 s according to the K-S and F-T tests, although it is completely absent in the I-V test. In Fig. 3.7 we show the dipole ($\ell = 1$, upper panel) and quadrupole ($\ell = 2$, lower panel) average of the computed period spacings, $\overline{\Delta\Pi_k}$, assessed in a range of periods that includes the periods observed in TIC 095332541 and TIC 333432673 (300 – 500 s), shown as curves for different stellar masses. The g -mode adiabatic pulsation periods employed to assess $\overline{\Delta\Pi_k}$ were computed with the LP-PUL pulsation code (Córscico & Althaus, 2006b). We can safely discard a period spacing of ~ 40 s due to the fact that if such a long period spacing were real, TIC 333432673 should have an extremely low mass, irreconcilable with the spectroscopic mass. Thus, we can assume that the mean period spacing of 20.19 s is robust and reliable for this star. It can be associated with a sequence of $\ell = 1$ modes³. An $\ell = 2$ period spacing, if present, should have a value $\Delta\Pi_{\ell=2} \sim \Delta\Pi_{\ell=1} / \sqrt{3} \sim 11.7$ s. Given the absence of a period spacing of this value in the three statistical tests, we conclude that there is no period spacing corresponding to modes with $\ell = 2$ in the observed pulsational spectrum of TIC 333432673. We compared the period spacing of ~ 20.19 s with the $\overline{\Delta\Pi_k}$ in terms of T_{eff} for all the masses considered in the upper panel of Fig. 3.7. The resulting mass value is $M_* \sim 0.61 M_\odot$ or $M_* \sim 0.60 M_\odot$ if the star is before or after the evolutionary knee, respectively. These values are in good agreement with the spectroscopic mass value ($M_* = 0.58^{+0.16}_{-0.08} M_\odot$).

³If they were $\ell = 2$, then the stellar mass of TIC 333432673 would be extremely low (see lower panel of Fig. 3.7), and thus, incompatible with the spectroscopic mass.

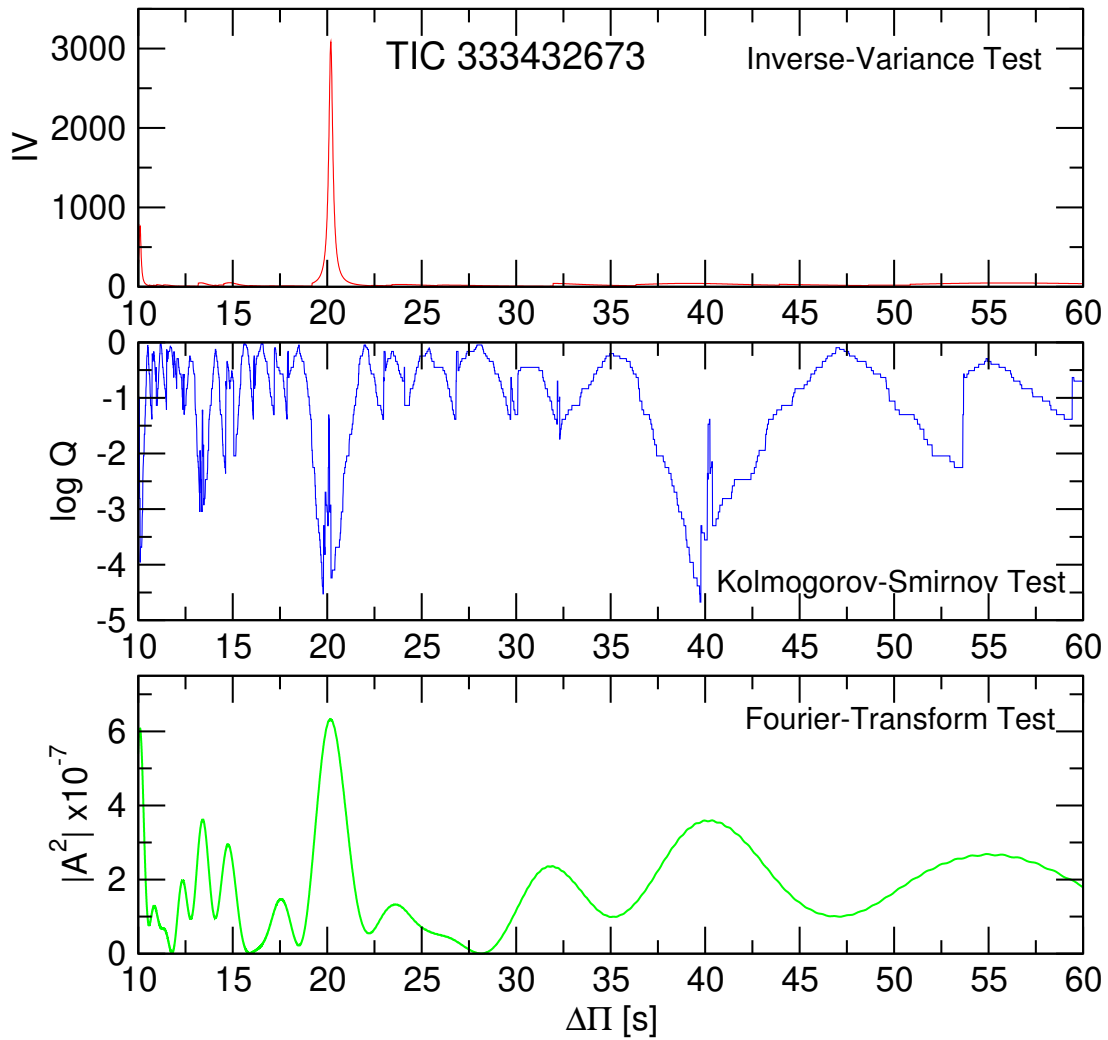


Figure 3.6: I-V (upper panel), K-S (middle panel), and F-T significance tests to search for a constant period spacing in TIC 333432673. The tests are applied to the set of 6 pulsation periods of Table 3.3. A strong signal of a constant period spacing at ~ 20 s is evident. See text for details.

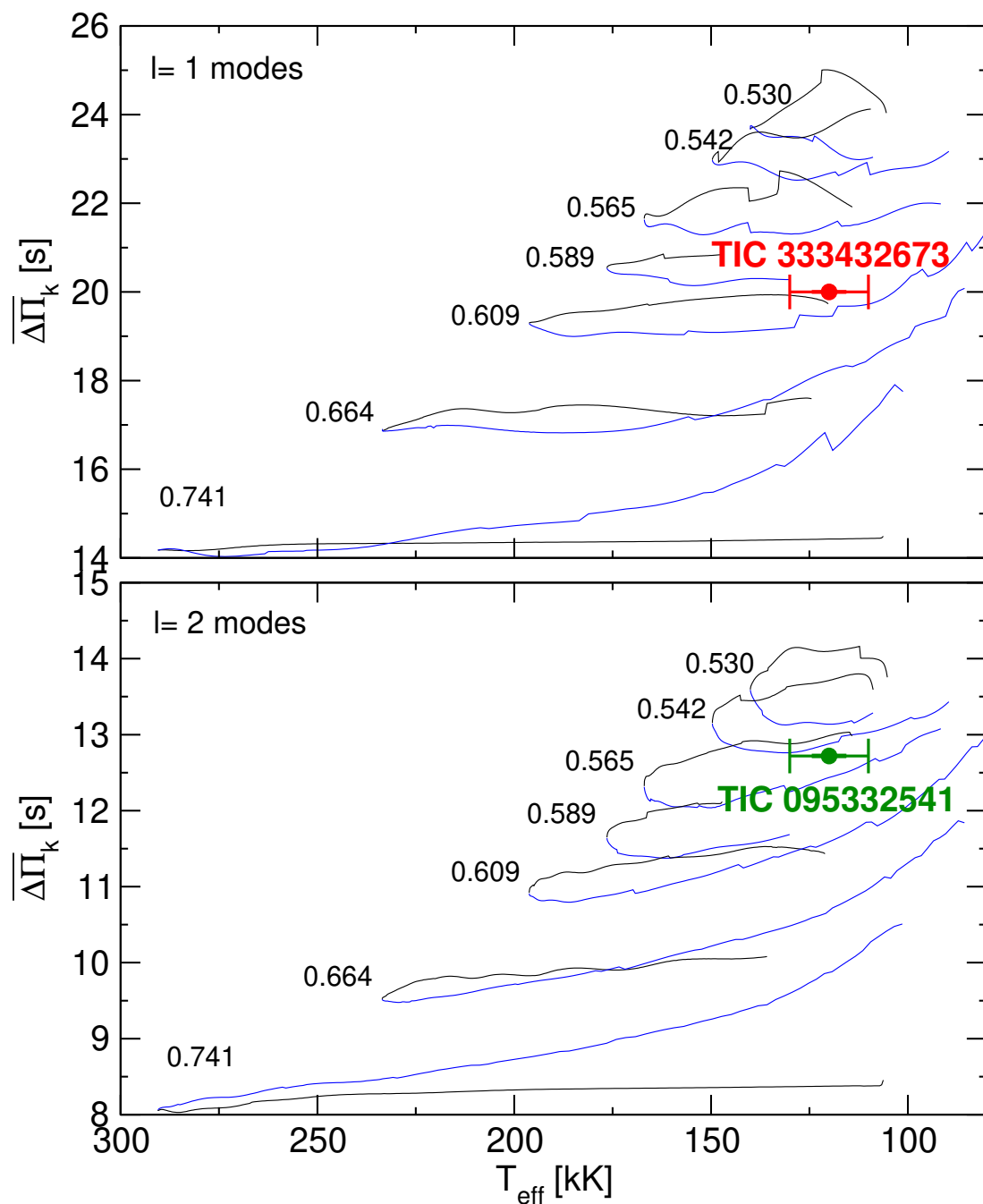


Figure 3.7: Upper panel: dipole ($\ell = 1$) average of the computed period spacings, $\overline{\Delta\Pi_k}$, assessed in a range of periods that includes the periods observed in the GW Vir star TIC 095332541 and TIC 333432673, shown as black (blue) curves corresponding to stages before (after) the maximum T_{eff} for different stellar masses. The location of TIC 333432673 when we use the spectroscopic effective temperature, $T_{\text{eff}} = 120\,000 \pm 10\,000$ K, and the dipole period spacing $\Delta\Pi_{\ell=1} = 20.19$ s, is highlighted with a red circle in the upper panel. Lower panel: same as in upper panel, but for the average of the computed period spacings with $\ell = 2$. The GW Vir star TIC 09533254 is drawn in this plot considering a quadrupole period spacing of ~ 13 s (see Sect. 3.5.5).

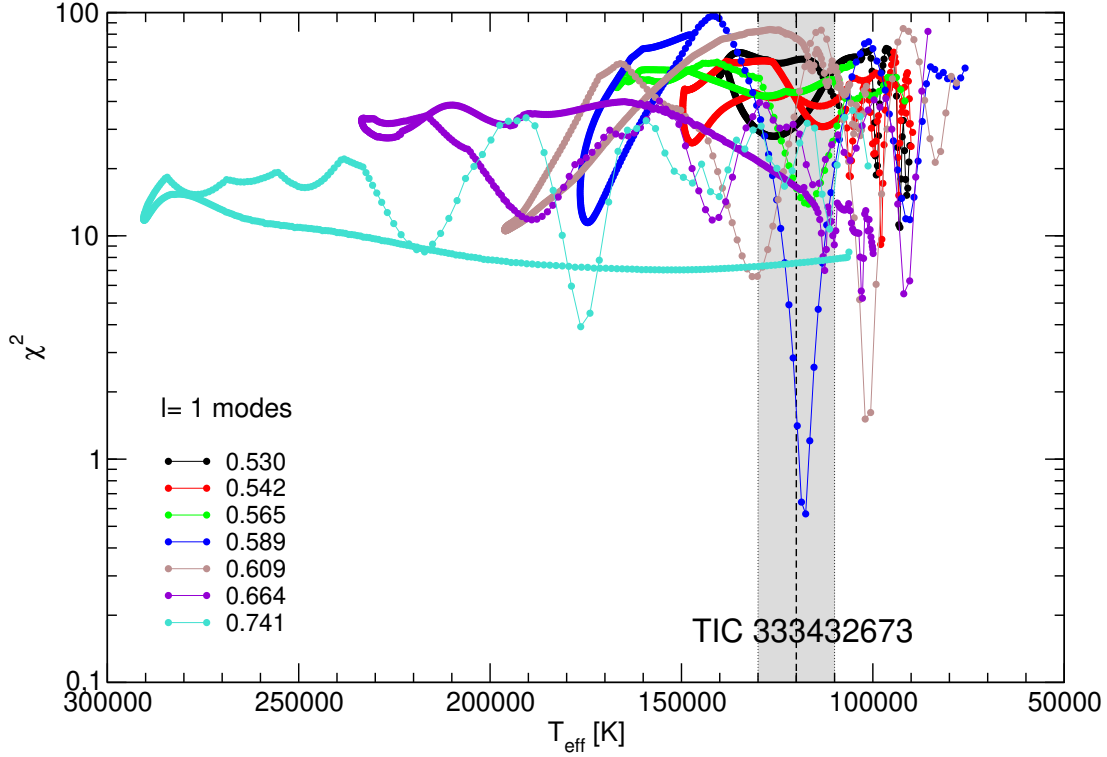


Figure 3.8: The quality function of the period fits in terms of the effective temperature for the PG 1159 sequences with different stellar masses (in solar units) corresponding to the case in which all the observed periods are assumed to be associated to dipole ($\ell = 1$) modes. We note the presence of a strong minimum corresponding to $M_{\star} = 0.589M_{\odot}$ and $T_{\text{eff}} = 117\,560$ K. The vertical dashed line is the spectroscopic T_{eff} of TIC 333432673 (120 000 K) and the gray zone depicts its uncertainties ($\pm 10\,000$ K).

3.5.3 Period-to-period fits for TIC 333432673

A powerful asteroseismological tool to disentangle the internal structure of GW Vir stars is to seek theoretical models that best match the individual pulsation periods of the target stars. To measure the goodness of the match between the theoretical pulsation periods ($\Pi_{\ell,k}$) and the observed individual periods (Π_i°), we assess the merit function $\chi^2(M_{\star}, T_{\text{eff}}) = \frac{1}{N} \sum_{i=1}^N \min[(\Pi_{\ell,k} - \Pi_i^{\circ})^2]$ (see, for instance, Córscico et al., 2021a). Here, N is the number of observed periods. In order to find the stellar model that best replicates the observed periods exhibited by each target star — the “asteroseismological” model — we evaluate the function χ^2 for stellar masses between 0.530 and $0.741M_{\odot}$ and effective temperatures in the range $80\,000 - 300\,000$ K, with $\Delta T_{\text{eff}} \sim 30$ K. For each target star, the PG 1159 model that shows the lowest value of χ^2 is adopted as the best-fit asteroseismological model.

The period-to-period fits for TIC 333432673 lead us to an excellent seismological solution for this star. The quality function versus the effective temperature for the different stellar

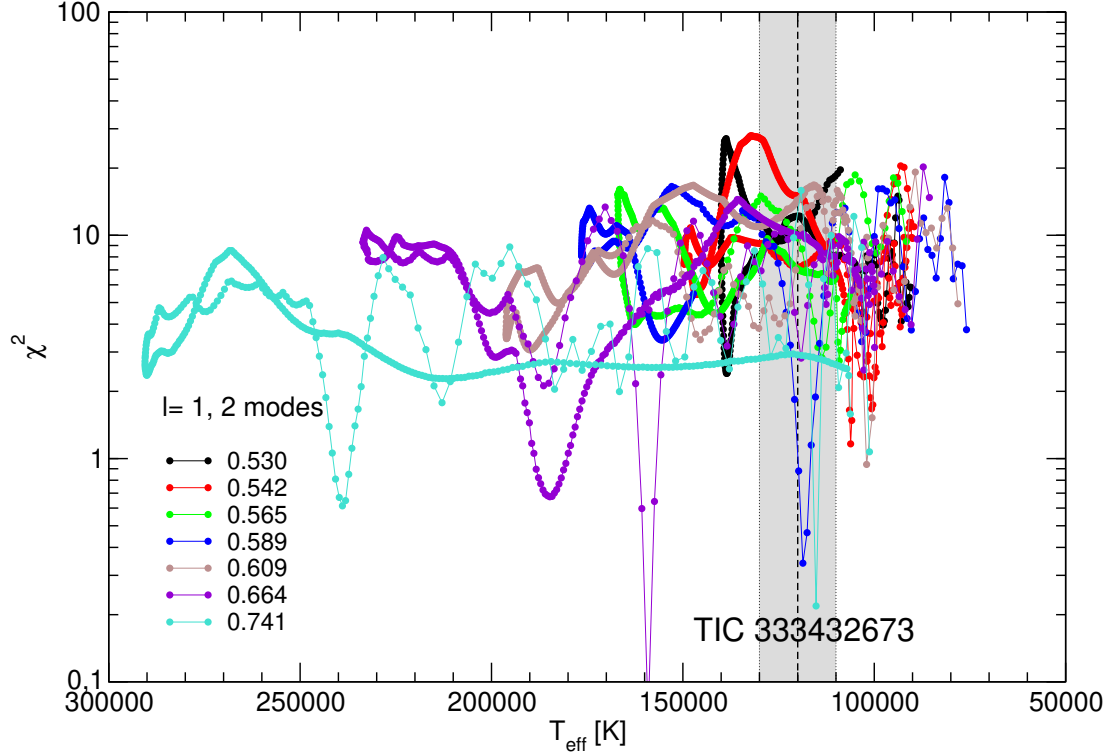


Figure 3.9: The quality function of the period fits in terms of the effective temperature for the PG 1159 sequences with different stellar masses (in solar units) corresponding to the case in which the observed periods are assumed to be associated to dipole ($\ell = 1$) and quadrupole ($\ell = 2$) modes. We note the presence of two strong minimum compatible with the effective temperature of the star, corresponding to $M_{\star} = 0.589M_{\odot}$ and $T_{\text{eff}} = 118\,655$ K, and $M_{\star} = 0.741M_{\odot}$ and $T_{\text{eff}} = 115\,203$ K.

Table 3.6: Observed and theoretical periods of the asteroseismological model for TIC 333432673 [$M_{\star} = 0.589M_{\odot}$, $T_{\text{eff}} = 117\,560$ K, $\log(L_{\star}/L_{\odot}) = 1.896$]. Periods are in seconds and rates of period change (theoretical) are in units of 10^{-12} s/s. $\delta\Pi_i = \Pi_i^{\text{O}} - \Pi_k$ represents the period differences, ℓ the harmonic degree, and k the radial order.

Π_i^{O} (s)	ℓ^{O}	Π_k (s)	ℓ	k	$\delta\Pi_k$ (s)	$\dot{\Pi}_k$ (10^{-12} s/s)
335.153	1	335.306	1	14	-0.153	6.006
374.933	1	374.215	1	16	0.718	6.763
394.579	1	396.035	1	17	-1.456	5.165
455.621	1	455.941	1	20	-0.320	5.632
496.181	1	496.467	1	22	-0.286	8.181

masses corresponding to the case in which we assume that all the observed periods correspond to $\ell = 1$ modes is shown in Fig. 3.8. We note that, among the periods 496.181 s and 496.689 s⁴ The stellar mass of this model is $M_\star = 0.589 M_\odot$, in perfect agreement with the mass derived with the period spacing, $M_\star = 0.60 - 0.61 M_\odot$, and the spectroscopic mass value, $M_\star = 0.58 M_\odot$.

We have also performed period fits assuming the situation in which the five observed periods are a mix of $\ell = 1$ and $\ell = 2$ periods, i.e., we compare the observed periods with dipole and quadrupole theoretical periods. In this case, which is illustrated in Fig. 3.9, we find two possible solutions compatible with the spectroscopic effective temperature, one of them characterized by $T_{\text{eff}} = 118\,655$ K, $M_\star = 0.589 M_\odot$, and $\chi^2 = 0.340$ s² and the other one characterized by $T_{\text{eff}} = 115\,203$ K, $M_\star = 0.741 M_\odot$ and $\chi^2 = 0.219$ s². In addition, a very strong minimum of χ^2 is found for a model with $T_{\text{eff}} = 159\,100$ K, $M_\star = 0.664 M_\odot$ and $\chi^2 = 0.070$ s², but we have to discard this model as a possible solution since it is too hot and incompatible with the range of possible effective temperatures given by spectroscopy.

In summary, we face the problem of choosing an asteroseismological model among three possible solutions. In Section 3.5.2 we found that the periods of TIC 333432673 make up an equispaced pattern with a period separation of 20.19 s corresponding to dipole modes. This finding constitutes a strong constraint on the assignment of the ℓ value of the modes, that is, it indicates that the identification of all the observed periods with modes $\ell = 1$ is robust. In Córscico et al. (2021a) we have employed this constraint to assign the ℓ value of the periods of a set of GW Vir stars observed with TESS. Using that constraint for TIC 333432673, we safely retain the solution characterized by $T_{\text{eff}} = 117\,560$ K and $M_\star = 0.589 M_\odot$, in which all modes are dipole modes, as the asteroseismological model for this star. We note that this solution is very close to one of the possible solutions obtained when we assume a possible mixture of $\ell = 1$ and $\ell = 2$ modes in the observed spectrum of TIC 333432673 ($T_{\text{eff}} = 118\,655$ K and $M_\star = 0.589 M_\odot$).

In Table 3.6 we show a detailed comparison of the observed periods of TIC 333432673 and the theoretical periods of the asteroseismological model. According to our asteroseismological model, all the periods exhibited by the star correspond to $\ell = 1$ modes with high radial order k . We compute the average of the absolute period differences, $\overline{\delta\Pi_i} = (\sum_{i=1}^n |\delta\Pi_i|) / n$, where $\delta\Pi_i = (\Pi_{\ell,k} - \Pi_i^o)$ and $n = 5$, and the root-mean-square residual, $\sigma = \sqrt{(\sum_{i=1}^n |\delta\Pi_i|^2) / n} = \sqrt{\chi^2}$. We compute also the Bayes Information Criterion (BIC; Koen & Laney, 2000), $\text{BIC} = n_p \left(\frac{\log n}{n} \right) + \log \sigma^2$, where n_p is the number of free parameters of the models, and n is the

⁴These two very close periods could be part of a rotational frequency triplet; see at the end of Sect. 3.4, we have retained only the largest amplitude one, that is, 496.181 s. So, we employ a set of 5 observed periods in our period fits (first column in Table 3.6). It is noteworthy the existence of a very clear minima of the quality function ($\chi^2 = 0.568$ s²) corresponding to an asteroseismological model characterized by an effective temperature of $T_{\text{eff}} = 117\,560$ K, very close to the spectroscopic effective temperature of TIC 333432673 and well within its uncertainties ($T_{\text{eff}} = 120\,000 \pm 10\,000$ K).

Table 3.7: The main characteristics of the new GW Vir star TIC 333432673.

Quantity	Spectroscopy	Asteroseismology
	Astrometry	
T_{eff} [kK]	120 ± 10	118 ± 12
M_{\star} [M_{\odot}]	$0.58^{+0.16}_{-0.08}$	0.589 ± 0.020
$\log g$ [cm/s ²]	7.5 ± 0.5	$7.55^{+0.52}_{-0.55}$
$\log(L_{\star}/L_{\odot})$...	$1.90^{+0.25}_{-0.34}$
$\log(R_{\star}/R_{\odot})$...	$-1.67^{+0.22}_{-0.25}$
$(X_{\text{He}}, X_{\text{C}}, X_{\text{O}})_s$	0.75, 0.25, ...	0.30, 0.38, 0.23
d [pc]	389 ± 5^a	459^{+188}_{-156}
π [mas]	$2.57^{+0.07,a}_{-0.04}$	$2.18^{+1.12}_{-1.85}$

References: (a) Gaia DR3.

number of fitted periods. The smaller the value of BIC, the better the quality of the fit. In our case, $n_p = 2$ (stellar mass and effective temperature), and $n = 5$. We obtain $\overline{\delta\Pi_i} = 0.59$ s, $\sigma = 0.75$ s, and $\text{BIC} = 0.03$, which means that our period fit is excellent, although admittedly, the differences between theoretical and observed periods is larger than the uncertainties in the measured periods.

We also include in Table 3.6 the rates of period change ($\dot{\Pi} \equiv d\Pi/dt$) predicted for each g mode of TIC 333432673. Note that all of them are positive ($\dot{\Pi} > 0$), implying that the periods are lengthening over time. The rate of change of periods in WDs and pre-WDs is related to \dot{T} (T being the temperature at the region of the period formation) and \dot{R}_{\star} (R_{\star} being the stellar radius) through the order-of-magnitude expression $(\dot{\Pi}/\Pi) \approx -a(\dot{T}/T) + b(\dot{R}_{\star}/R_{\star})$ (Winget et al., 1983). According to our asteroseismological model, the star is cooling at almost constant radius after reaching its maximum temperature (evolutionary knee), i.e., TIC 333432673 is in its cooling stage. As a consequence, $\dot{T} < 0$ and $\dot{R}_{\star} \sim 0$, and then, $\dot{\Pi} > 0$. Continuous monitoring of this star could in the future make it possible to measure rates of period change for comparison with our theoretical predictions, if the pulsations are shown to be otherwise coherent over the span of observations.

In Table 3.7, we list the spectroscopic and astrometric parameters of TIC 333432673 and the main characteristics of the asteroseismological model found in this work. The seismological stellar mass is in excellent agreement with the value derived from the period spacing ($0.60 - 0.61 M_{\odot}$) and the spectroscopic mass. The average of the dipole ($\ell = 1$) period spacings of our asteroseismological model is $\overline{\Delta\Pi} = 20.469$ s, in excellent agreement with the $\ell = 1$ mean period spacing derived for TIC 333432673, $\Delta\Pi = 20.19$ s.

In Fig. 3.10 we show the fractional abundances of the main chemical species, ^4He , ^{12}C , and ^{16}O , corresponding to our asteroseismological model with $M_{\star} = 0.589 M_{\odot}$ and $T_{\text{eff}} = 117\,560$ K. The chemical transition regions of O/C and O/C/He are clearly visible. The location, thick-

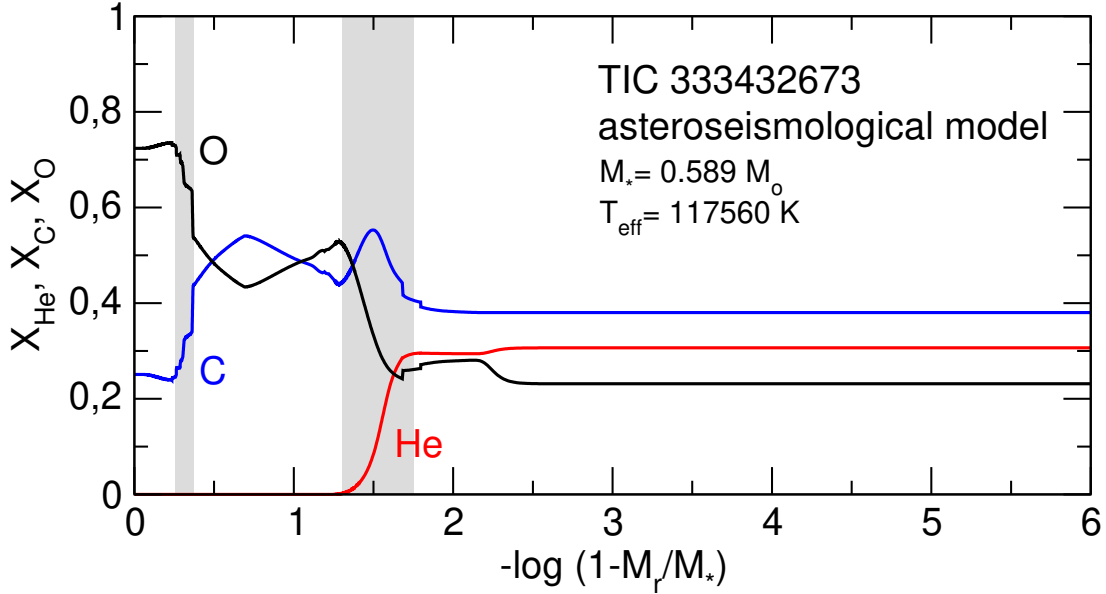


Figure 3.10: Internal chemical profile of the asteroseismological model of TIC 333432673 ($M_* = 0.589M_\odot$, $T_{\text{eff}} = 117560$ K) in terms of the outer fractional mass. The locations of the O/C and O/C/He chemical interfaces are indicated with gray regions.

ness, and steepness of these chemical interfaces define the mode-trapping properties of the models. (see, e.g., Córscico & Althaus, 2005, 2006b, for details).

3.5.4 The asteroseismological distance of TIC 333432673

We can assess the asteroseismological distance on the basis of the luminosity of the asteroseismological model [$\log(L_*/L_\odot) = 1.90^{+0.25}_{-0.34}$]. Using a bolometric correction $BC = -7.05$, interpolated from the values corresponding to PG 1159–035 ($T_{\text{eff}} = 140\,000$ K, $BC = -7.6$), RX J2117+3142 ($T_{\text{eff}} = 160\,000$ K, $BC = -7.95$), and PG 2131+066 ($T_{\text{eff}} = 95\,000$ K, $BC = -6.0$), as given by Kawaler & Bradley (1994), Córscico et al. (2007), and Kawaler et al. (1995), respectively, the visual absolute magnitude can be assessed as $M_V = M_B - BC$, where $M_B = M_{B,\odot} - 2.5 \times \log(L_*/L_\odot)$. We employ the solar bolometric magnitude $M_{B,\odot} = 4.74$ (Cox, 2000). The seismological distance d is derived from the relation: $\log d = (1/5) [m_V - M_V + 5 - A_V(d)]$, where we employ the 3D reddening map of Lallement et al. (2014) (see also Capitanio et al., 2017; Lallement et al., 2018)⁵ to infer $E(B - V)$ and then the interstellar absorption $A_V(d)$, which is a nonlinear function of the distance and also depends on the Galactic latitude (b) and longitude (l). For the equatorial coordinates of TIC 333432673 (Epoch B2000.00, $\alpha = 6^{\text{h}}41^{\text{m}}15.^{\text{s}}88$, $\delta = -13^{\circ}41'31.''31$) the corresponding Galactic latitude is $b = -8.^{\circ}41280066$ and $l = 224.^{\circ}06462259$. We use the apparent visual magnitude $m_V = 15.658$ (TESS catalog),

⁵<https://stilism.obspm.fr/>

and obtain iteratively the seismological distance, $d = 459_{-156}^{+188}$ pc, parallax $\pi = 2.18_{-1.85}^{+1.12}$ mas, and extinction coefficient $A_V = 0.307_{-0.121}^{+0.053}$. The large uncertainty in the seismological distance comes mainly from the large uncertainty in the luminosity of the asteroseismological model and in the reddening coefficient $E(B - V)$. A very important check for the validation of the asteroseismological model of TIC 333432673 is the comparison of the seismological distance with the distance derived from astrometry. The following estimates from Gaia EDR3 are available (Gaia Collaboration et al., 2021b): $d_G = 389.0_{-5.2}^{+5.6}$ pc and $\pi_G = 2.57_{-0.04}^{+0.07}$ mas. They are in excellent agreement with the asteroseismological derivations in view of the uncertainties in both determinations. This adds confidence to the correctness of the asteroseismological model.

3.5.5 Mean period spacing of TIC 095332541

In Fig. 3.11 we show the results of applying the significance tests to the set of 7 periods of TIC 095332541 (Table 3.4). The three tests point to the existence of a probable constant period spacing of $\Delta\Pi \sim 31$ s. If we want to guess what the stellar mass corresponding to this period spacing would be by comparing it with the average of the computed period spacings, we realize that we cannot draw the location of TIC 095332541 in the diagrams of Fig. 3.7. A period spacing as long as ~ 31 s for TIC 095332541 does not make physical sense, since it would be compatible with a star with an unusually low mass (much below $0.4M_\odot$), in strong conflict with the spectroscopic mass. Therefore, this possible period spacing has to be disregarded. For the same reason, we also rule out a possible period spacing of ~ 45 s that can be seen in Fig. 3.11. A third possible constant period separation is ~ 13 s, as suggested by the K-S test. Such a short period spacing could make any sense only if all the modes exhibited are quadrupole ($\ell = 2$) modes. In this case, the stellar mass would be $\sim 0.55M_\odot$ (see lower panel of Fig. 3.7). However, since this possible period-spacing signature is only suggested by one of the significance tests, we cannot take it as true, and we are forced to discard it. We conclude that it is not possible to find a realistic period spacing for TIC 095332541 with this data set of only 7 detected periods.

We have sought an alternative interpretation of the period spectrum of TIC 095332541 in which we consider subsets of periods when looking for patterns of period spacing. In particular, if we consider the subset of 4 periods 352.567 s, 404.390 s, 416.389 s, and 441.555 s, we find what is plotted in Fig. 3.12, where we show the statistical tests considering this reduced set of periods. The existence of a period spacing of around ~ 13 s is evident according the three significance tests. Averaging the results between the three tests, we find $\Delta\Pi = 12.71$ s. A period spacing of ~ 13 s can be due to that the four periods considered are associated to $\ell = 2$ modes, which implies a stellar mass in the range $\sim 0.548 - 0.570M_\odot$ (see lower panel of Fig. 3.7). The remainder periods (410.298 s, and 447.293⁶) could be $\ell = 2$ modes affected

⁶The period at 416.011 s is very similar to the period at 416.389 s, and could be a component of a rotational multiplet or a single mode with $\ell = 1$. We do not consider it in the computation of the period

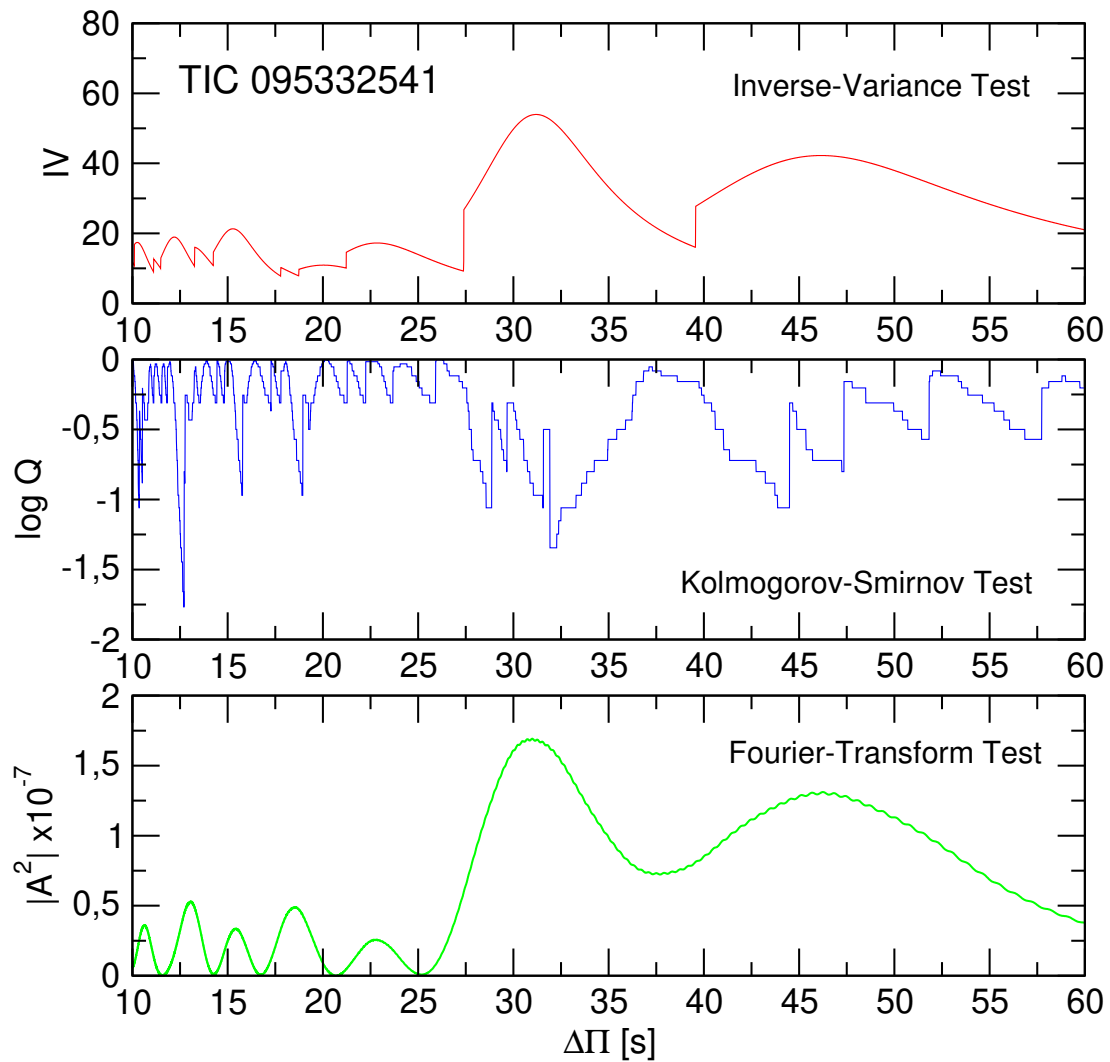


Figure 3.11: I-V (upper panel) and K-S (middle panel), and F-T (bottom panel) significance tests to search for a constant period spacing in TIC 095332541, applied to the set of 7 pulsation periods of Table 3.4. A signal of a constant period spacing at ~ 31 s is evident in the three tests. See text for details.

by mode trapping, or, alternatively, $\ell = 1$ modes. The absence of a dipole period spacing at ~ 21 sec (according to the asymptotic theory) and the simultaneous presence of a quadrupole period spacing at ~ 13 s is hard to explain, because modes with $\ell = 1$ should have higher observable amplitudes when compared with modes to $\ell = 2$ due to geometric cancellation effects (Dziembowski, 1977). However, it might be possible that some $\ell = 1$ modes, and the associated period spacing, are not driven to observable amplitudes for some reason; for instance, it might be that $\ell = 1$ modes are not excited at the effective temperature and gravity of this star but $\ell = 2$ modes are unstable.

The other possibility in the interpretation of the period spacing of ~ 13 s of TIC 095332541 is that it is due to $\ell = 1$ modes. In this case, however, the stellar mass should be unusually large for the standards of PG 1159 stars ($\gtrsim 1M_{\odot}$; see upper panel of Fig. 3.7), and in serious conflict with the spectroscopic mass ($\sim 0.58M_{\odot}$), or mode trapping is severe.

We conclude that the period spacing $\Delta\Pi = 12.71$ s is most probably associated to quadrupole modes and that the stellar mass derived on the basis of this period spacing is $M_{\star} = 0.55 - 0.57M_{\odot}$. This constraint in the value of ℓ of the four periods at 352.567 s, 404.390 s, 416.389 s, and 441.555 s will be used in the next section when performing period fits to TIC 095332541.

3.5.6 Period-to-period fits for TIC 095332541

We have also performed period fits for the new GW Vir star TIC 095332541. We started by examining the case in which we consider the 7 detected periods of this star according to Table 3.4. Unfortunately, our period-to-period fits for this star, either considering all modes as $\ell = 1$, as $\ell = 2$, or as a mixture of $\ell = 1$ and $\ell = 2$, do not allow us to find a clear seismological solution, that is, a single minima of the function χ^2 distinguishable from a crowd of similar minima associated to different effective temperatures and stellar masses. Therefore, we cannot find an asteroseismological model for this star in this case.

We also carried out period fits for this star following the results obtained in Sect. 3.5.5. That is, we assumed that a subset of 4 periods are associated with $\ell = 2$ modes, and left the assignment as $\ell = 1$ or $\ell = 2$ free to the remaining two periods. Specifically, we set the "observed" value $\ell = 2$ for the periods at 352.567 s, 404.390 s, 416.389 s, and 441.555 s, and we assume that the periods at 410.298 s and 447.293 s can be either $\ell = 1$ or $\ell = 2$. The quality function versus the effective temperature for the different stellar masses is depicted in Fig. 3.13. Unfortunately, there is no single and clear solution in the range of effective temperature of the star, so, neither in this case we are able to choose any asteroseismological model for TIC 095332541.

Since an asteroseismological model for TIC 095332541 is not available, we lack the luminosity of the star, and that prevents us from assessing its seismological distance. More obser-

spacing nor in our period fits; see the next section.

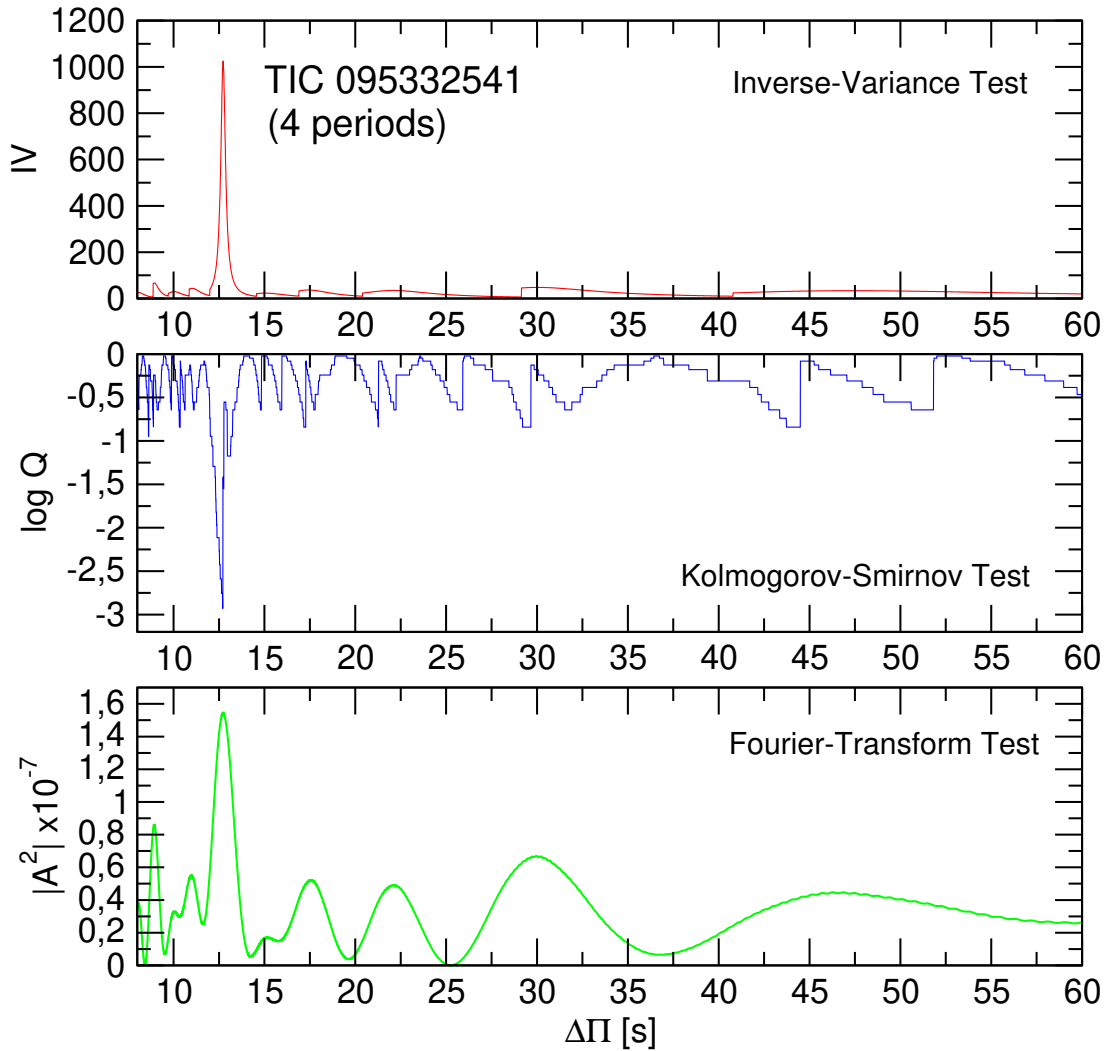


Figure 3.12: Same as in Fig. 3.11, but for the case in which we consider the subset of 4 periods 352.567 s, 404.390 s, 416.389 s, and 441.555 s. See text for details.

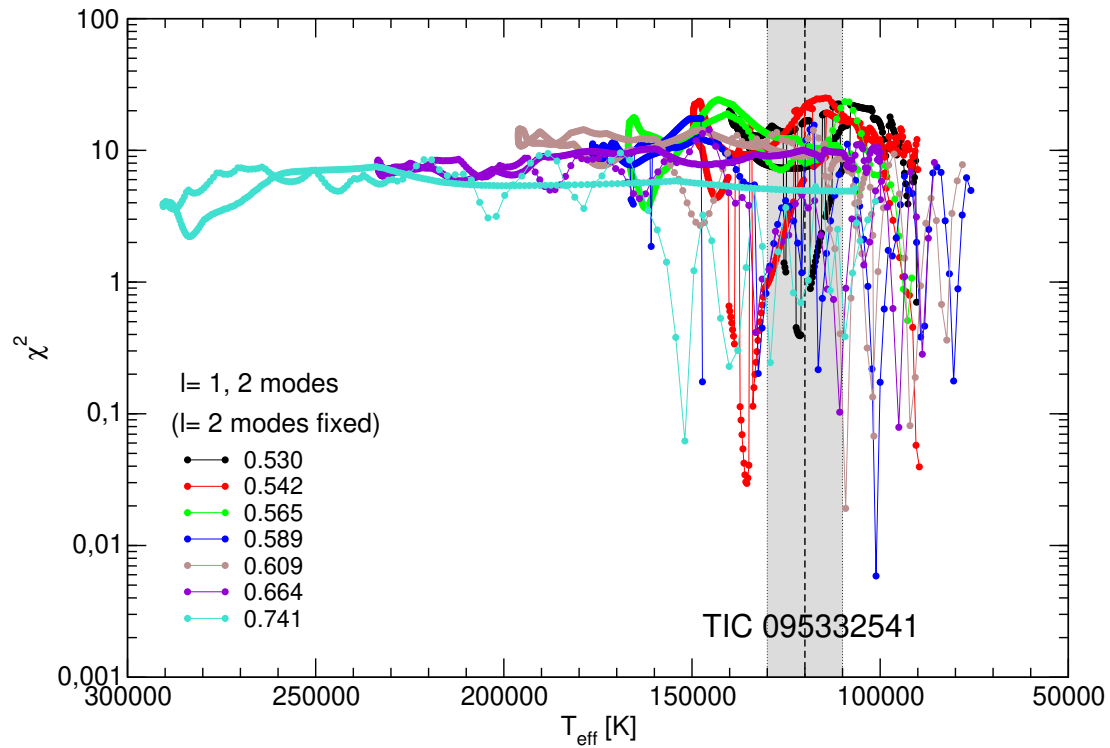


Figure 3.13: The quality function of the period fits in terms of the effective temperature for the PG 1159 sequences with different stellar masses (in solar units) corresponding to the case in which 4 observed periods are assumed to be associated to quadrupole ($\ell = 2$) and the remainder 2 periods can be associated either to dipole ($\ell = 1$) or quadrupole ($\ell = 2$) modes. No clear and distinguishable seismological solution is evident for TIC 095332541 in this figure.

variations are needed.

3.6 Summary and conclusions

In this paper, we have presented the discovery of two new GW Vir stars, TIC 333432673 and TIC 095332541. We have derived atmospheric parameters for both stars by fitting synthetic spectra to the newly obtained low to intermediate resolution SOAR/GOODMAN for TIC 333432673 and INT/IDS for TIC 095332541 spectra. The determined atmospheric parameters show that TIC 333432673 and TIC 095332541 are identical in terms of surface temperature and surface gravity ($T_{\text{eff}} = 120,000 \pm 10,000 \text{ K}$ and $\log g = 7.5 \pm 0.5$) and they are only different regarding the surface C and He abundance.

We investigate the potential variability of the two new PG 1159 stars by examining their short and ultra-short-cadence single-sector observations obtained with TESS. Our frequency analysis reveals six significant independent oscillation frequencies for TIC 333432673 and seven for TIC 095332541, which we associate with g -modes. The periodicities detected in these two PG 1159 stars are compatible with the period spectrum typically exhibited by GW Vir stars. TIC 333432673 exhibits a possible contamination by other sources in the TESS aperture within a magnitude limit of $\Delta m = 2$. We examined the target pixel files of TIC 333432673 in order to verify the frequencies that are originated by the PG 1159. We found that the location of the 4 frequencies ($S/N \geq 5$) is most consistent with the position of TIC 333432673. TIC 333432673 is a great target for ground-based time-series photometry in order to confirm TESS signals. Furthermore, TIC 333432673 and TIC 095332541 are excellent targets for the future ground-based photometric monitoring in order to possibly measure rates of period change and compare it to the theoretical predictions.

We have carried out an asteroseismological investigation on both GW Vir stars employing fully evolutionary models of PG 1159 stars. For TIC 095332541 we have been able to find a possible constant period spacing, and therefore it was possible to estimate a stellar mass in the range $0.55 - 0.57 M_{\odot}$ based on that quantity. Unfortunately, we did not find an asteroseismological model for this star, which prevented us from estimating its structural parameters and its seismological distance. For TIC 333432673 we have been able to find a very clear constant period spacing that leads to a stellar mass in very good agreement with the spectroscopic mass. Also for this star, we were able to find an asteroseismological model whose mass is in excellent agreement with the spectroscopic mass, and the derived seismological distance is in concordance with the distance estimated by Gaia for this star.

Pulsating hydrogen-deficient white dwarfs: Discovery of two new GW Vir stars TIC0403800675 and TIC1989122424

This chapter was originally published as:



Pulsating hydrogen-deficient white dwarfs and pre-white dwarfs observed with *TESS* – IV. Discovery of two new GW Vir stars: TIC 0403800675 and TIC 1989122424

Murat Uzundag^{1,2*}, Alejandro H. Córscico,^{3,4} S. O. Kepler⁵, Leandro G. Althaus,^{3,4} Klaus Werner⁶, Nicole Reindl⁷ and Maja Vučković¹

Author contributions: This paper is based on an original idea by Murat Uzundag, who prepared the observations. Murat Uzundag performed the SOAR/Goodman data reduction. Klaus Werner performed the atmospheric analysis. Nicole Reindl produced a fit to the spectral energy distribution (SED). Alejandro H. Córscico and Leandro G. Althaus produced evolutionary tracks for both targets. All authors contributed to the discussion and interpretation of the results and commented on the written draft of the paper.

ABSTRACT

Two new GW Vir-type pulsating white dwarf stars, TIC 0403800675 (WDJ115727.68-280349.64) and TIC 1989122424 (WD J211738.38-552801.18) discovered based on the photometric data from the Transiting Exoplanet Survey Satellite (TESS) were presented. For both stars, the TESS light curves reveal the presence of oscillations with periods in a narrow range between 400 and 410 s, which are associated with typical gravity (g)-modes. Follow-up ground-based spectroscopy shows that both stars have similar effective temperature ($T_{\text{eff}} = 110,000 \pm 10,000$ K) and surface gravity ($\log g = 7.5 \pm 0.5$), but different He/C composition (mass fractions): He=0.75 and C=0.25 for TIC 0403800675, and He=0.50 and C=0.50

for TIC 1989122424. By performing a fit to their spectral energy distributions, we found for both stars radii and luminosities of $R = 0.019 \pm 0.002 R_{\odot}$ and $\log(L/L_{\odot}) = 1.68^{+0.15}_{-0.24}$, respectively. By employing evolutionary tracks of PG 1159 stars, we find the masses of both stars to be $0.56 \pm 0.18 M_{\odot}$ from the $\log g - T_{\text{eff}}$ diagram and $0.60^{+0.11}_{-0.09} M_{\odot}$ from the Hertzsprung Russell diagram.

4.1 Introduction

White dwarf (WD) stars are the end evolutionary state of all stars formed with initial masses below around $7-11 M_{\odot}$, which comprise more than 95% of all stars in our galaxy (Althaus et al., 2010b). In the course of their evolution, WDs cross at least one phase of pulsational instability that converts them into pulsating variable stars. GW Vir variable stars are the hottest known class of pulsating WDs and pre-WDs, with $75\,000 \text{ K} \leq T_{\text{eff}} \leq 250\,000 \text{ K}$ and $5.3 \leq \log g \leq 8$ (Werner et al., 2021). They are located within a definite instability strip (see Fig. 1 of Córscico et al., 2019). GW Vir stars include some objects that are still surrounded by a nebula, called the variable planetary nebula nuclei (PNNVs), and some objects that lack a nebula, which are called DOVs. Both groups (DOVs and PNNVs) are frequently referred to as GW Vir variable stars. GW Vir stars display brightness fluctuations with periods in the range $300 - 6\,000 \text{ s}$, and amplitudes up to a few mmag (1 mmag=1 ppt), associated with low-order ($\ell \leq 2$) non-radial g (gravity) modes.

GW Vir stars are pulsating PG 1159 stars (after the prototype of the spectroscopic class, the star PG 1159-035), which are hydrogen(H)-deficient post-AGB stars with surface layers rich in helium (He), carbon (C) and oxygen (O) (Werner & Herwig, 2006). It is believed that this mixture is a result of a mixing event produced by a late He flash during the so-called born-again episode (Fujimoto, 1977; Schoenberner, 1979; Iben et al., 1983; Althaus et al., 2010b). PG 1159 stars are considered the evolutionary link between post-AGB stars and most of the H-deficient WDs, including DO and DB WDs (Herwig et al., 1999; Althaus et al., 2005b; Sowicka et al., 2021b). They can be either the outcome of single star evolution (late thermal pulse scenario, LTP, or very late thermal pulse scenario, VLTP) or binary star evolution (double WD merger). The classification of GW Vir stars includes also the pulsating Wolf-Rayet central stars of a planetary nebula ([WC]) and Early-[WC] = [WCE] stars since they share the same pulsation properties of pulsating PG 1159 stars (Quirion et al., 2007). Thus far about 50 PG 1159 stars have been identified (Werner et al., 2021). Amongst them, approximately 50% (22 objects; see Córscico et al., 2019; Uzundag et al., 2021) have been discovered to be pulsating. It is especially important to find new pulsators of this class, as they can provide insight into the AGB and VLTP/LTP phases, as well as angular momentum loss throughout the extensive mass loss phases (Kepler et al., 2014, and references therein).

Prior to space missions, GW Vir stars were monitored through long-term observations carried out by the multisite photometric campaign with the "Whole Earth Telescope" (WET;

Nather et al., 1990). These observations provided invaluable sources of information to constrain their internal structure (Winget et al., 1991). The spectral observations from the Sloan Digital Sky Survey (SDSS, York et al., 2000) promoted the discovery of a GW Vir pulsating star, SDSS J075415.12+085232.18 (Kepler et al., 2014). The advent of the *Kepler* space mission has resulted in important advances in the study of pulsating stars in general (Aerts, 2021; Kurtz, 2022) and pulsating WDs in particular (Córscico, 2020). Unfortunately, during the main mission of the *Kepler* satellite (Borucki et al., 2010b), no GW Vir star was observed. During the *Kepler* extended mission (*K2*; Howell et al., 2014), the prototype PG 1159–035 was observed during almost 50 days of coverage and the findings will be reported soon (G. O. da Rosa et al. in preparation). Currently, uninterrupted observations from space with the Transiting Exoplanet Survey Satellite (TESS) allow us to find and characterize new and already known GW Vir stars. Indeed, TESS has allowed a detailed asteroseismological analysis of a number of formerly known GW Vir stars (Córscico et al., 2021a), enabling the determination of their fundamental parameters and evolutionary properties. The discovery of two new GW Vir stars has been presented by Uzundag et al. (2021). In these studies, using asteroseismic techniques (e.g., asymptotic period spacing and rotational splittings), the authors were able to determine the internal chemical stratification, total mass and, in some cases, rotation velocity of GW Vir stars.

In this work, we present the discovery of two new GW Vir stars, TIC 0403800675 (WD J115727.68-280349.6) and TIC 198912242 (WD J211738.38-552801.1), which were observed during the survey phase of the southern ecliptic hemisphere cycle 1 and 3 of TESS. In addition, for each target we obtained low-resolution spectra and fitted model atmospheres to estimate their fundamental atmospheric parameters, and examined the TESS light curve to identify the pulsational modes. This study is the fourth part of a series of papers devoted to the study of pulsating H-deficient WDs and pre-WDs observed with TESS. The first article was devoted to a set of six already known GW Vir stars including PNNVs and DOVs (Córscico et al., 2021a), the second to the discovery of two new GW Vir stars of the DOV type (Uzundag et al., 2021), and the third to a detailed asteroseismological analysis of the prototype of the pulsating DB WD, GD 358 (Córscico et al., 2022).

The paper is organized as follows. In Sect. 4.2, we present the details of spectroscopic observations and the data reduction. In Sect. 4.3, we derive atmospheric parameters for each star by fitting synthetic spectra to the newly obtained low-resolution spectra. In Sect. 4.5, we analyze the photometric TESS data and give details on the frequency analysis. Finally, in Sect. 5.5, we summarize our main results.

4.2 Spectroscopy

TIC 0403800675 (WD J115727.68–280349.6) and TIC 198912242 (WD J211738.38–552801.1) were classified as WD candidates by Gentile Fusillo et al. (2019) from their colors and Gaia

Table 4.1: Log of spectroscopic observations including TESS and WD catalogs numbers, right ascension, declination, *Gaia* magnitude, date, exposure time, grating, resolution and signal-to-noise ratio.

TIC	Name	RA (J2000)	Dec (J2000)	G_{mag}	Obs. Date (UT)	Exp. Time (sec)	Grating (l/mm)	R. ($\Delta\lambda$ (Å))	S/N
0403800675	WD ¹	11:57:28	-28:03:53	16.16	2021-06-18	1200	400	4.6	65
1989122424	WD ²	21:17:40	-55:28:16	16.75	2021-06-19	900	400	4.6	70

1: WDJ115727.68–280349.6

2: WDJ211738.38–552801.1

DR2 parallax. The *Gaia* DR3 parallax and corresponding distance for TIC 0403800675 are $\pi = 1.86_{-0.06}^{+0.07}$ mas and $d = 535.41_{-18.44}^{+19.49}$ pc, while for TIC 198912242 are $\pi = 1.45_{-0.06}^{+0.05}$ mas and $d = 688.27_{-26.31}^{+22.34}$ pc (Bailer-Jones et al., 2021), respectively.

To estimate the atmospheric parameters of TIC 0403800675 and TIC 1989122424, we obtained spectra with the Goodman High-Throughput Spectrograph (GHTS, Clemens et al., 2004) at the SOAR 4.1-m telescope on Cerro Pachón. We reduced the spectroscopic data using the instrument pipeline¹ including overscan, trim, slit trim, bias and flat corrections. We employed a method developed by Pych (2004), which is included in the pipeline, to identify and remove cosmic rays. After the reduction was completed, the wavelength calibration has been applied by using *PyRAF*² (Science Software Branch at STScI, 2012). We used the frames produced with the internal He-Ar-Ne comparison lamp at the same telescope position as the targets in order to apply wavelength calibrations. The sixth order Legendre function is used to calibrate the pixel-wavelength correspondence using an atlas of known He-Ar-Ne lines. Finally, we used the standard star Feige 110 seen with the identical apparatus to normalize the spectra with a high-order Legendre function. Table 4.1 contains the details of the spectroscopic observations, including the name of the targets, right ascension, declination, *Gaia* magnitude, date, exposure time, grating, resolution, and S/N ratio.

4.3 Spectral fitting

The spectral lines in the spectra of TIC 0403800675 and TIC 1989122424 are all from He II and C IV. Oxygen, which is the most abundant element in PG 1159 stars after He and C, and nitrogen (N) —which is present as a trace element in some PG 1159 stars— may be visible in spectra with higher resolution and signal-to-noise ratio. In the spectra of both stars, there are no indications of the presence of H.

¹https://github.com/soar-telescope/goodman_pipeline

²http://www.stsci.edu/institute/software_hardware/pyraf

For the spectral analysis, we used a grid of line-blanketed non-local thermodynamic equilibrium (non-LTE) model atmospheres consisting of H, He, and C as introduced by Werner et al. (2014). The grid spans $T_{\text{eff}} = 60,000\text{--}140,000$ K in effective temperature and $\log g = 4.8\text{--}8.3$ in surface gravity, with steps of 5,000 K or 10,000 K and 0.3 dex, respectively. C/He mass ratios in the range 0.0–1.0 were considered, namely C/He = 0.0, 0.03, 0.09, 0.33, 0.77, and 1.0. The hydrogen abundance was set to zero. Synthetic spectra were convolved with a Gaussian accounting for the spectral resolution of the observations. The best fitting models were chosen by visual comparison with the rectified observed spectra.

The model fits are depicted in Fig. 4.1. Both stars have $T_{\text{eff}} = 110,000 \pm 10,000$ K and $\log g = 7.5 \pm 0.5$, but a different atmospheric composition. For TIC 0403800675, we found $\text{He} = 0.75^{+0.05}_{-0.15}$ and $\text{C} = 0.25^{+0.15}_{-0.05}$ and for TIC 1989122424, we measured $\text{He} = 0.50^{+0.20}_{-0.05}$ and $\text{C} = 0.50^{+0.05}_{-0.20}$ (mass fractions). An upper limit to the abundance of hydrogen was determined to be 5% by mass. At this abundance, a $\text{H}\alpha$ emission core would be detectable and the $\text{H}\beta$ line blend with the respective He II line would be too strong.

In Fig. 4.2 we show the location of the new GW Vir stars in the $\log g\text{--}T_{\text{eff}}$ diagram. By linear interpolation among the PG 1159 evolutionary tracks of Althaus et al. (2005b) and Miller Bertolami & Althaus (2006), we derive a stellar mass of $M_{\star} = 0.56 \pm 0.18 M_{\odot}$ for TIC 0403800675 and TIC 1989122424. These evolutionary tracks of PG 1159 stars have been compared by Miller Bertolami & Althaus (2007a) with other independent published calculations. These authors concluded that the differences in the inferred masses using different sets of PG1159 evolutionary tracks must be less than $\sim 0.01 M_{\odot}$. This constitutes the systematic errors associated with the Althaus et al. (2005b) and Miller Bertolami & Althaus (2006) evolutionary tracks. We conclude that the errors in the spectroscopic mass of the two new GW Vir stars come mainly from the uncertainties in the spectroscopic $\log g$ and T_{eff} .

4.4 SED fitting

In order to determine the radii of the two stars we performed a fit to the spectral energy distribution (SED), by varying the solid angle $\pi(R/d)^2$, (which relates the flux at the surface of the system to what is received at Earth) until a good agreement of the predicted fluxes and the observations was found as shown in Fig. 4.4. We employed our best fitting model atmospheres for both stars, and using the Fitzpatrick (1999) reddening law, our predicted spectra were reddened for different values of $E_{\text{B-V}}$. We used the distance provided by Bailer-Jones et al. (2021) and employed photometry from GALEX (Bianchi et al., 2014), Gaia DR2 and eDR3 (Gaia Collaboration et al., 2021b), and Pan-STARRS1 (Chambers et al., 2016). Magnitudes were converted into fluxes using the VizieR Photometry viewer³. For TIC 0403800675 we find a reddening of $E_{\text{B-V}} = 0.034$ mag and for TIC 1989122424 we find $E_{\text{B-V}} = 0.048$ mag. Both values are in agreement with the upper limits of the 2D dust map provided by Schlafly

³<http://vizier.unistra.fr/vizier/sed/>

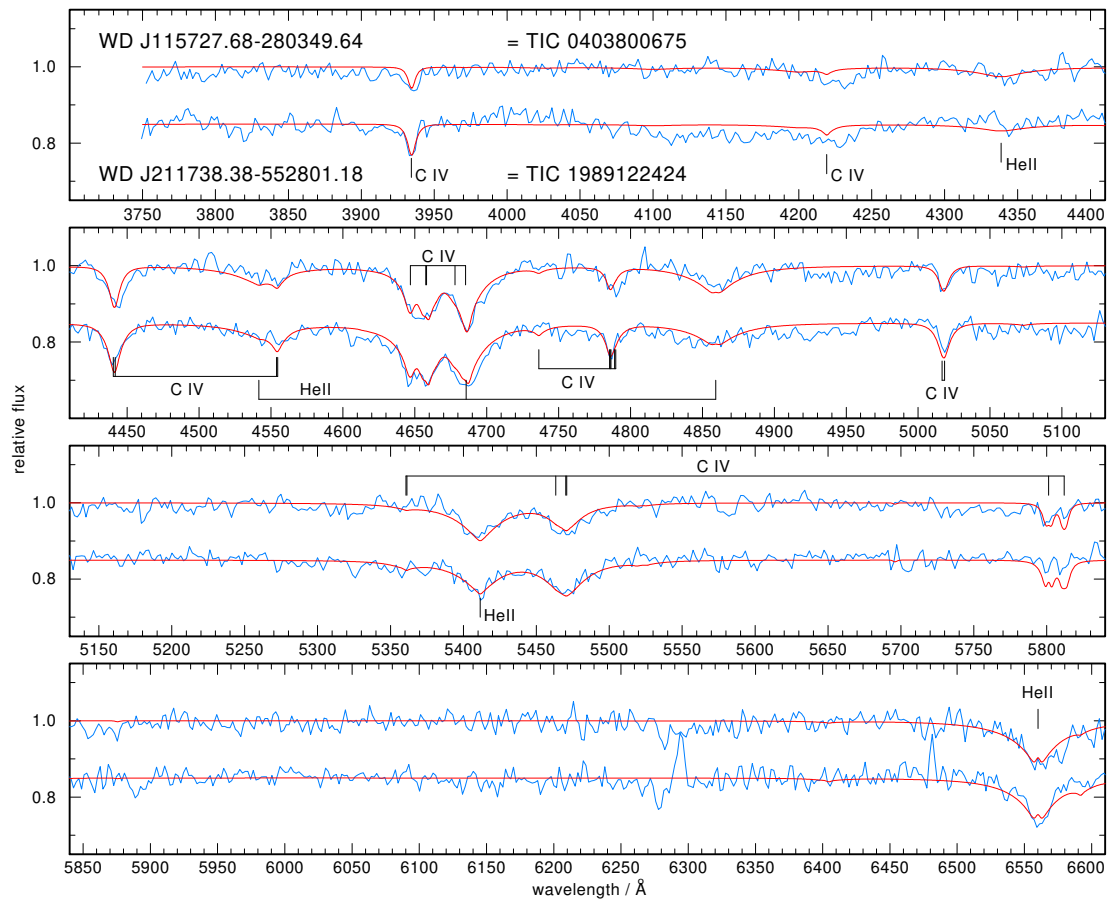


Figure 4.1: Optical spectra of the two new GW Vir stars (blue graphs) obtained with SOAR/Goodman. Overplotted are the best-fit models (red). Identifications of He II and C IV lines are marked.

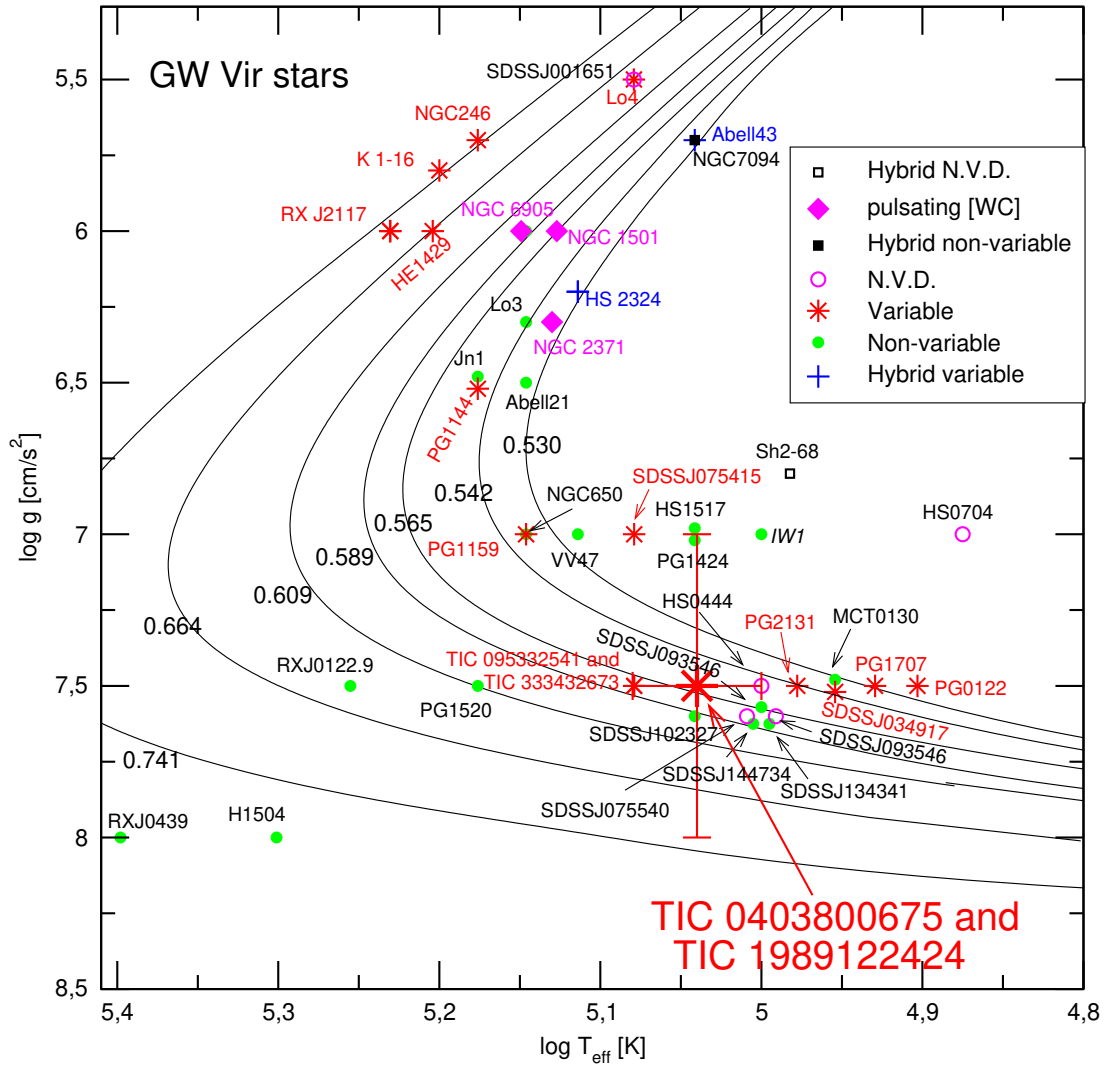


Figure 4.2: The already known variable and non-variable PG 1159 stars and variable [WCE] stars in the $\log T_{\text{eff}} - \log g$ diagram. Thin solid black curves show the post-born again evolutionary tracks from Althaus et al. (2005b) and Miller Bertolami & Althaus (2006) for different stellar masses noted on top of each track. “N.V.D.” stands for PG 1159 stars with no variability data. “Hybrid” refers to PG 1159 stars exhibiting H in their atmospheres. The location of the two new GW Vir stars TIC 0403800675 and TIC 1989122424 is emphasized with a large red star symbol and error bars. Both stars share the same spectroscopic surface parameters, $T_{\text{eff}} = 110\,000 \pm 10\,000$ K and $\log g = 7.5 \pm 0.5$.

Table 4.2: Properties of GW Vir pulsating stars studied in this work.

Quantity	TIC 0403800675	TIC 1989122424
T_{eff} [kK]	110 ± 10	110 ± 10
M_{\star} [M_{\odot}]	0.56 ± 0.18	0.56 ± 0.18
$\log g$ [cm/s ²]	7.5 ± 0.5	7.5 ± 0.5
(He, C)	$0.75^{+0.05}_{-0.15}, 0.25^{+0.15}_{-0.05}$	$0.50^{+0.20}_{-0.05}, 0.50^{+0.05}_{-0.20}$
R_{\star} [R_{\odot}]	0.019 ± 0.002	0.019 ± 0.002
$\log(L_{\star}/L_{\odot})$	$1.68^{+0.15}_{-0.24}$	$1.68^{+0.15}_{-0.24}$
$E(B - V)$ [mag]	0.034	0.048
π [mas]	$1.86^{+0.07}_{-0.06}$	$1.45^{+0.05}_{-0.06}$
d [pc]	$535.41^{+19.49}_{-18.44}$	$688.27^{+22.34}_{-26.31}$

& Finkbeiner (2011). For both stars we determine a radius of $R = 0.019 \pm 0.002 R_{\odot}$. Using $L = 4\pi\sigma R^2 T_{\text{eff}}^4$, where σ is the Stefan-Boltzmann constant, we calculate for both stars a luminosity of $\log(L/L_{\odot}) = 1.68^{+0.15}_{-0.24}$. This allows us now to also derive the masses for TIC 0403800675 and TIC 1989122424 in the Hertzsprung–Russell diagram (HRD, see Fig. 4.4). By linear interpolation among the PG 1159 evolutionary tracks of Miller Bertolami & Althaus (2006), we derive a stellar mass of $M_{\star} = 0.60^{+0.11}_{-0.09} M_{\odot}$ for both stars, which is in agreement with the masses derived from the $\log g$ - T_{eff} diagram (see Fig.4.3). The main characteristics of TIC 0403800675 and TIC 1989122424 are listed in Table 4.2 including atmospheric parameters, masses, luminosities, radii, distances and reddening.

4.5 Photometric observations — TESS

TIC 0403800675 was observed by TESS in sector 10 between 26 March to 22 April 2019 and in sector 36 between 7 March and 2 April 2021. TIC 1989122424 was observed in a single sector 27 between 4 July and 30 July 2020 with only 120 sec cadence.

The light curves were downloaded from The Mikulski Archive for Space Telescopes, which is hosted by the Space Telescope Science Institute (STScI)⁴ as FITS format. The light curves were processed by the Science Processing Operations Center (SPOC) pipeline (Jenkins et al., 2016). We first downloaded the target pixel file (TPF) of interest from the MAST archive, which is maintained by the Lightkurve Collaboration; Lightkurve Collaboration et al. (2018). The TPFs comprises an 11x11 postage stamp of pixels from the one of four CCDs per camera that the target is located on. The TPFs are examined to determine the amount of crowding and other potential bright sources near the target. Because both targets had a modest amount of crowding which we evaluated using the CROWDSAP parameter, that was set to 0.6

⁴<http://archive.stsci.edu/>

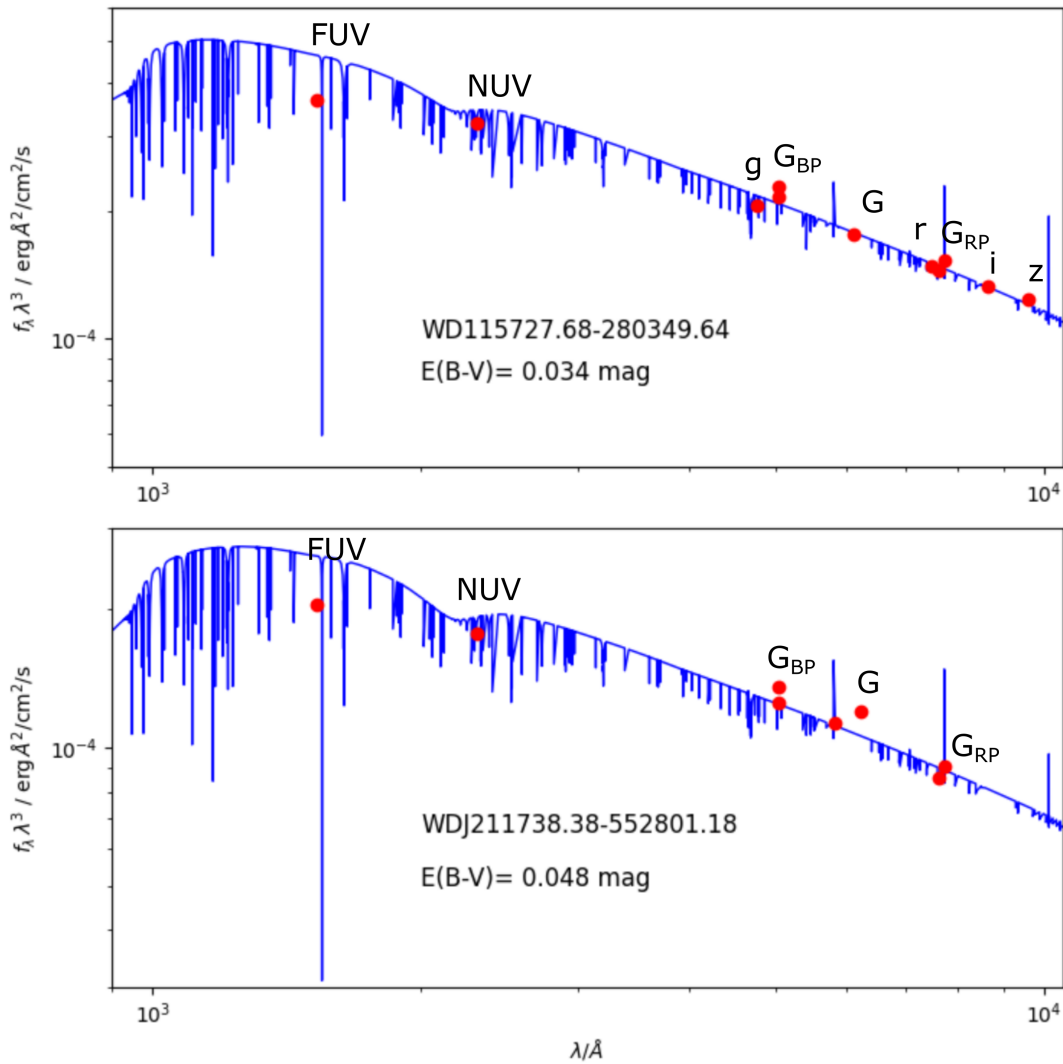


Figure 4.3: Fit to the SEDs of TIC 0403800675 (WDJ115727.68-280349.64, upper panel) and TIC 1989122424 (WDJ211738.38-552801.18, bottom panel). The red dots indicate filter-averaged fluxes that were converted from observed magnitudes. Error bars are smaller than symbol size. The blue solid lines represent our best fitting model fluxes with the parameters as stated in Section 4.4. The assumed values for the interstellar reddening in each fit are indicated.

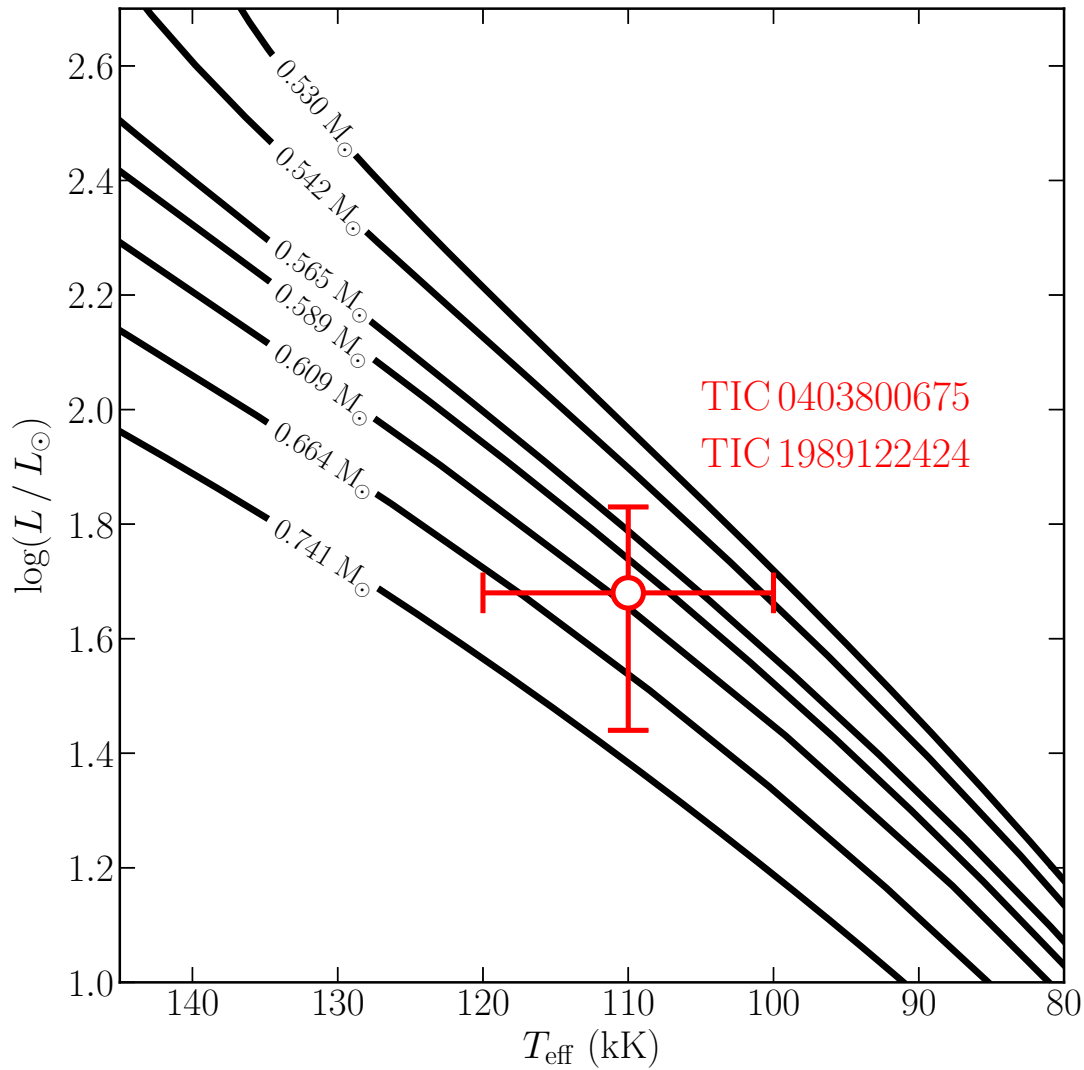


Figure 4.4: The location of the two new GW Vir stars TIC 0403800675 and TIC 1989122424 (emphasized with a large red dot symbol and error bars) in the HRD. Black curves show the post-born again evolutionary tracks from Miller Bertolami & Althaus (2006) for different stellar masses. Both stars share the same effective temperatures ($T_{\text{eff}} = 110\,000 \pm 10\,000$ K) and luminosities ($\log(L_*/L_\odot) = 1.68^{+0.15}_{-0.24}$).

for TIC 1989122424 and 0.8 for TIC 0403800675. Therefore we have decided to use the pipeline aperture as it gave the most optimal result with respect to signal-to-noise ratio. We extracted times in barycentric corrected dynamical Julian days and fluxes (PDCSAP FLUX) from the FITS files. We converted the fluxes to fractional variations from the mean and transformed to amplitudes in parts-per-thousand (ppt). Finally, the data were sigma-clipped based on 5σ to remove the outliers which appear above 5 times the median of intensities. The resulting short-cadence (SC) light curve of TIC 040380067 comprises 29 298 images spanning 47.4 days, while the resulting SC light curve of TIC 1989122424 includes 16 478 data points spanning 23.9 days. TIC 0403800675 was also observed with ultra-short-cadence (USC) during 23.9 days in sector 36 that yield 93 122 images.

4.5.1 Frequency solution

The Fourier transform (FT) was used to examine the periodicities present in the light curves. The frequencies, amplitudes and errors were estimated using both the `Period04` and our custom tool. We fitted each frequency that appears above the 0.1% false alarm probability (FAP). The FAP level was calculated by reshuffling the light curves 1000 times as described in (Kepler, 1993). The errors of each frequency and amplitude of the pulsation modes were estimated using Monte Carlo simulations (Lenz & Breger, 2005). Furthermore, we have calculated sliding Fourier transform (sFT) for both stars in order to see the temporal evolution of the pulsational modes over the course of TESS observations. To do so, we use a nine-day sliding window with a 2-day step size. A color-scale in ppt units is used to depict the amplitudes. Following that, we calculate the Fourier transform of each subset and trail them in time.

For TIC 0403800675, we analyzed TESS observations using the SC and USC modes. The SC mode samples every 2-minutes allowing us to analyze the frequency range up to the Nyquist frequency at about $4167 \mu\text{Hz}$, while the USC mode samples every 20-seconds permitting us to examine the frequency range up to the Nyquist frequency at about $25\,000 \mu\text{Hz}$. For TIC 0403800675, we detected two significant frequencies at $2445 \mu\text{Hz}$ and $2450 \mu\text{Hz}$. In Fig.4.5, we show FT of combined SC data of sector 10 and 36 (black lines) (top panel), while the middle panel, we present USC data of sector 36. The magenta lines show the FT of the prewhitened light curves. The signals are 20% more amplified in USC data. Sliding Fourier transform display the both identified peaks in Fig.4.5. The frequencies detected for TIC 0403800675 are presented in Table 4.3.

For TIC 1989122424, we also detected two clear signals at similar region between $2450 \mu\text{Hz}$ and $2490 \mu\text{Hz}$ using solely SC observations. In Fig.4.6, we focus on this region and show the FT of the original light curve (black line) and the FT of the prewhitened light curves (magenta line). In sFT, these peaks also clearly visible along with some other peaks. The two reported peaks at $2466 \mu\text{Hz}$ and $2479 \mu\text{Hz}$ are clearly visible in sFT and they are stable during the run. We also see that there is a peak at $2470 \mu\text{Hz}$, which is stable during the first ten days. For this peak, we did not produce an non-linear least square (NLLS) fit to extract from the light curve.

Table 4.3: Identified frequencies, periods, and amplitudes (and their uncertainties) and the signal-to-noise ratio in the data of TIC 0403800675. Frequency and amplitude that are detected in both sector 10 and 36.

Peak	ν (μHz)	Π (s)	A (ppt)	S/N
f_1	2443.597(51)	409.232(86)	1.63(33)	4.3
f_2	2449.261(33)	408.286(55)	2.54(33)	6.3

Table 4.4: Identified frequencies, periods, and amplitudes (and their uncertainties) and the signal-to-noise ratio in the data of TIC 1989122424.

Peak	ν (μHz)	Π (s)	A (ppt)	S/N
f_1	2466.673(41)	405.404(68)	18.35(2.89)	5.1
f_2	2479.888(44)	403.243(72)	16.99(2.89)	4.7

We need additional observations to confirm whether it is real pulsational peak or not. The detected frequencies for TIC 0403800675 are reported in Table 4.4.

We hypothesized that the two closely spaced frequencies in both amplitude spectra and sFT can be due to stellar rotation in which the pulsation frequencies are split into $2\ell+1$ azimuthal components. Assuming these frequencies are dipole modes and result from stellar rotation, then the rotation periods would range from 1.02 to 2.04 d (depending on the missing azimuthal order) for TIC 0403800675 and 0.43 d to 0.87 d for TIC 1989122424. Given the rotation periods of the GW Vir pulsating stars, which range from 5 hours to a few days (Córscico et al., 2019, 2021a), any of the potential solutions that we estimate for TIC 0403800675 and TIC 1989122424 could be conceivable. Furthermore, we note that the rotational periods of GW Vir stars cover about the same period range as white dwarfs showing ultra-highly excited (UHE) metals in their optical spectra. Reindl et al. (2021) discovered recently that this latter class of white dwarfs show photometric periods between 6 hours to 3 days and that their variability is likely caused by spots on the surfaces of these stars and/or geometrical effects of circumstellar material (see also Reindl et al. 2019). Since UHE white dwarfs are considered to be in an evolutionary stage immediately following that of the GW Vir pulsators, it would be interesting to know the rotational periods of more GW Vir stars in order to test a possible evolutionary connection.

4.6 Conclusions

In this paper, we have presented the discovery of two new GW Vir pulsating white dwarfs TIC 0403800675 and TIC 1989122424. We derived atmospheric parameters for TIC 0403800675 and TIC 1989122424 by fitting synthetic spectra to the newly obtained low-resolution

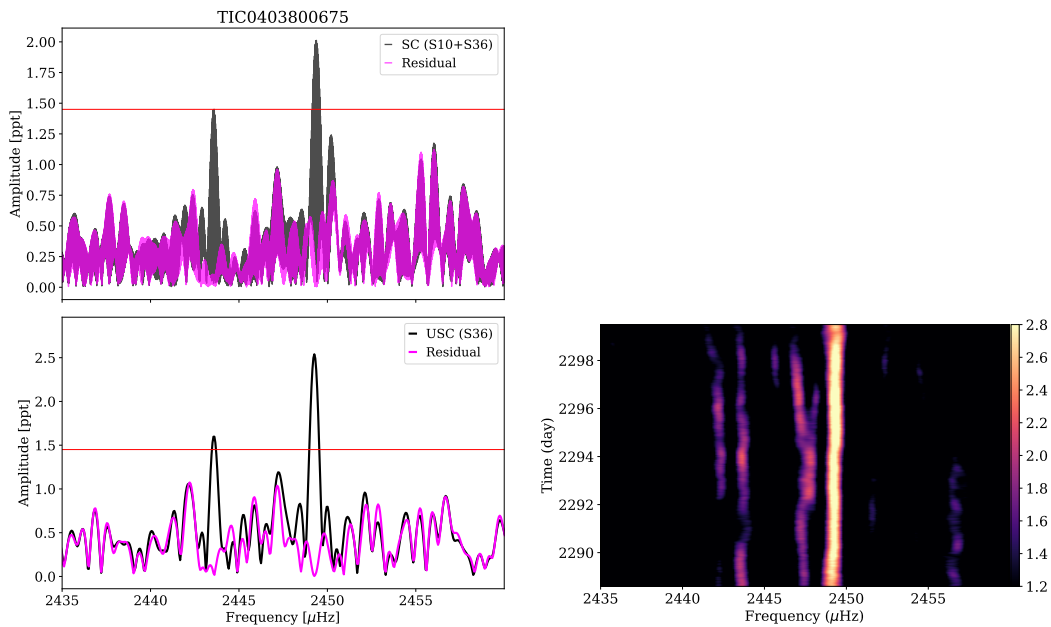


Figure 4.5: TOP LEFT: Fourier transform of short-cadence data of sector 10 and 36 (black lines) for TIC 0403800675. The magenta line depicts the FT of the prewhitened light curve. The horizontal red line indicates the 0.1% FAP level. MIDDLE LEFT: Fourier transform of ultra-short-cadence data of sector 36 (black lines) for TIC 0403800675. The red and magenta lines are the same as top panel the 0.1% FAP level and the FT of the prewhitened light curve, respectively. BOTTOM RIGHT: Sliding Fourier transform of ultra-short-cadence data of sector 36 data of TIC 0403800675. The color-scale illustrates amplitude in parts-per-thousand.

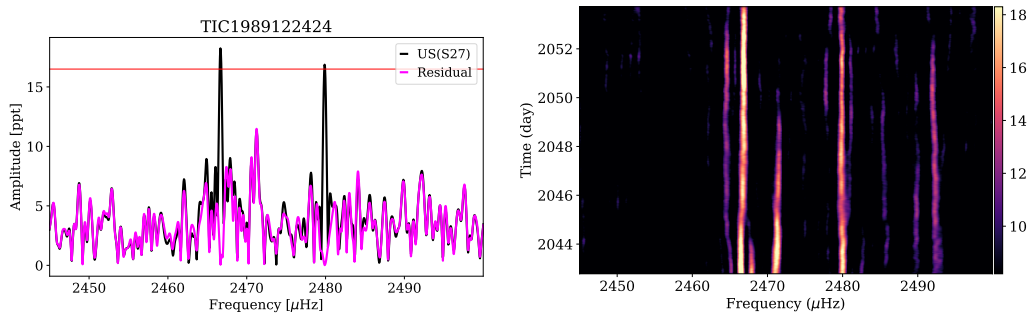


Figure 4.6: LEFT: Fourier transform of short-cadence data of sector 27 of TIC 1989122424. The horizontal red line indicates the 0.1% FAP level. The magenta line depicts the FT of the prewhitened light curve. RIGHT: Sliding Fourier transform of the same data-set of TIC 1989122424. The color-scale illustrates amplitude in parts-per-thousand.

SOAR/GOODMAN spectra. The determined spectroscopic parameters demonstrate that TIC 0403800675 and TIC 1989122424 are the same to within errors in terms of surface temperature and surface gravity ($T_{\text{eff}} = 110,000 \pm 10,000 \text{ K}$ and $\log g = 7.5 \pm 0.5$) and they are only different regarding the surface C and He abundance. By performing a fit to the SEDs and parallaxes we found for both stars radii and luminosities of $R_{\star} = 0.019 \pm 0.002 R_{\odot}$ and $\log(L_{\star}/L_{\odot}) = 1.68^{+0.15}_{-0.24}$, respectively. Using the Althaus et al. (2005b) and Miller Bertolami & Althaus (2006) evolutionary tracks of PG 1159 stars, we find a stellar mass for both stars of $0.56 \pm 0.18 M_{\odot}$ from the $\log g$ - T_{eff} diagram and $0.60^{+0.11}_{-0.09} M_{\odot}$ from the HRD.

We have used the TESS 120-second data for both objects, while we made use of 20-second cadence data for only TIC 0403800675. Both stars exhibit just two periodicities in their amplitude spectra preventing us to make use of the seismic tools of rotational multiplets and asymptotic period spacing. Both pulsational frequencies that we extracted from the light curves are of the order of 7 minutes, attributable to non-radial pulsation g -modes. We also produced sFTs to see if the pulsation modes are resolved and stable throughout the TESS observations, which is limited to a single sector. The analyzed data demonstrate that the main pulsational frequencies of our targets are stable and there is no clear pattern for rotational multiplets. Unfortunately, the presence of only two oscillation frequencies in the power spectrum of each star prevents us from making an asteroseismic modelling of these objects. We hope that more periods can be detected in the future, so that we can investigate the internal structure and evolutionary state of these stars through asteroseismological tools.

Volume limited sample of low mass red giant stars, the progenitors of hot subdwarf stars

This chapter was submitted as:

Astronomy & Astrophysics manuscript no. output
July 29, 2022

©ESO 2022

Volume-limited sample of low-mass red giant stars, the progenitors of hot subdwarf stars

I. Sample selection and binary classification method*

Murat Uzundag^{1,2}, Matías I. Jones², Maja Vučković¹, Joris Vos³, Alexey Bobrick⁴, Claudia Paladini²

Author contributions: The entire analysis that is presented in this chapter was performed by Murat Uzundag. The project was supervised by Matías I. Jones and Maja Vučković, who also provided guidance, discussion, and feedback as the analyses were developed and the manuscript was written. Murat Uzundag and Maja Vučković are PIs of the radial velocity monitoring program of the volume-limited-sample of low-mass red giants with the CORALIE spectrograph. Joris Vos and Alexey Bobrick assisted with the target selection processes. Murat Uzundag wrote the manuscript, and each co-author offered insightful comments.

ABSTRACT

Context. The current theory predicts that hot subdwarf binaries are produced from evolved low-mass binaries that have undergone mass transfer and drastic mass loss during either a common envelope phase or a stable Roche lobe overflow while on the red giant branch (RGB).

Aims. We perform a spectroscopic survey to find binary systems that include low-mass red giants near the tip of the RGB, which are predicted to be the direct progenitors of subdwarf B (sdB) stars. We aim to obtain a homogeneous sample to search for the observational evidence

of correlations between the key parameters governing the formation of sdB stars and constrain the physics of stable mass transfer.

Methods. Based on data from the *Gaia* mission and several ground-based, multi-band photometry surveys, we compiled a sample of low-mass red giant candidates. The candidates were selected according to their *Gaia* data release 2 (DR2) color, absolute magnitude and proper motion cuts. In this work, we concentrated on the southern hemisphere targets and conducted a spectroscopic survey of 88 red giant stars to search for the long-period RGB + MS binary systems within 200 pc. Combining radial velocity (RV) measurements from ground-based observations with CORALIE and RV measurements from *Gaia* DR2 and early data release 3 (eDR3) as well as the astrometric excess noise and RUWE measurements from *Gaia* DR3, we defined a robust binary classification method. In addition, we searched for known binary systems in the literature and in the *Gaia* DR3.

Results. We select a total of 211 RGB candidates in the southern hemisphere within 200 pc based on the *Gaia* DR2 color-magnitude diagram. Among them, a total of 33 red giants were reported as binary systems with orbital periods between 100 and 900 days, some of which are expected to be the direct progenitors of wide binary sdB stars. In addition, we classified 37 new binary candidates, whose orbital parameters will be measured with future spectroscopic follow-up.

Conclusion. Using high-quality astrometric measurements provided by the *Gaia* mission coupled with high-resolution spectroscopy from the ground, we provide a powerful method to search for low-mass red giant stars in binary systems.

5.1 Introduction

Hot subdwarf B stars (sdBs) are evolved low-mass red giants that have had almost all of their envelope stripped away near the tip of the first red giant branch (RGB), according to standard evolutionary scenarios (Dorman & Rood, 1993). They are evolved, compact ($\log g = 4.5 - 6.5$ dex) and hot ($T_{\text{eff}} = 20\,000 - 40\,000$ K) objects with radii between $0.15 R_{\odot}$ and $0.35 R_{\odot}$, located on the so-called extreme horizontal branch (EHB; see Heber, 2016, for a review). Their characteristic mass is close to the core-He-flash mass ($\sim 0.47 M_{\odot}$) and they have a very thin hydrogen envelope ($M_{\text{H}} < 0.01 M_{\odot}$). It was found that a large proportion of sdBs (40–70%) are in binaries (e.g. Maxted et al., 2001; Napiwotzki et al., 2004; Copperwheat et al., 2011b), implying that binary interactions are the most likely explanation for their formation.

The three binary formation channels that contribute to the sdB population are: the common-envelope (CE) ejection channel (Paczynski, 1976; Han et al., 2002), the stable Roche-lobe overflow (RLOF) channel (Han et al., 2002, 2003) and a binary white-dwarf (WD) merger (Webbink, 1984). The sdB component in both binary scenarios (CE and RLOF) has a relatively narrow mass range, peaking at $0.47 M_{\odot}$, whereas the double helium WD merger channel creates a single subdwarf star with a relatively wide and flat distribution, from 0.42 up to 0.72

M_{\odot} (Han et al., 2003). Han et al. (2002) showed that the CE ejection channel leads to close binaries with WD or main sequence (MS) companions with short orbital periods ranging from hours to tens of days. Much of the observational research has focused on these short-period systems, and currently, more than 300 short-period sdB systems have been detected (Kupfer et al., 2015; Schaffner et al., 2019; Dai et al., 2022, references therein).

The RLOF channel generates sdB+MS binaries with orbital periods ranging from 500 to 1600 days (Vos et al., 2019). These systems are challenging to detect, given their long orbital periods. Long-term observational campaigns have been dedicated to discover these systems over the last decades. Recently, the orbital parameters of long-period sdB binaries have been found for 26 systems (Vos et al., 2019; Otani et al., 2021; Németh et al., 2021; Molina et al., 2021) with periods ranging from 500 to 1500 days. Because both stars are visible in the spectrum, these systems are referred to as “composite” binaries which account for 30–40% of all sdBs (Vos et al., 2019). The observed composite binary systems present correlations between orbital elements, which revealed an invaluable source of information to test the RLOF channel. One of the first correlations that have been found is that between eccentricity and period in which the eccentricity increases with increasing orbital period (Vos et al., 2015). This finding contradicts evolutionary models since all current models predict circular orbits. Vos et al. (2015) demonstrated that the observed eccentricities of wide sdB binaries may be explained by combining two eccentricity pumping mechanisms, phase-dependent RLOF and a circumbinary disk. These models, on the other hand, fail to replicate the observed trend of greater eccentricity with longer orbital periods. Furthermore, the wide sdB binaries show another correlation between the mass ratio (q) and the orbital period (P_{orb}) (Vos et al., 2019). The chemical history of our Galaxy can precisely explain the observed relationship between the mass ratio and the orbital period, so called P- q relation, in long-period sdB binaries as found by Vos et al. (2020). The authors performed a small but statistically significant binary population synthesis study with the binary stellar evolution code MESA considering binaries with primary masses between $0.7 M_{\odot}$ and $2.0 M_{\odot}$ and initial orbital periods between ~ 100 and ~ 900 days. The Vos et al. (2020) study enables us to search for wide sdB binary systems’ progenitors right before they enter the RLOF phase, which are low-mass red giant branch stars.

The aim of this study is to analyze the observed characteristics of a statistically significant volume-limited sample of low-mass evolved RGB binaries that are potential progenitors of the wide sdB binaries. We perform a spectroscopic survey searching for binarity among selected low-mass RGB candidates. The observed volume-limited sample composed of pre- and post-mass transfer binaries will then allow us to study the binary interactions and the angular momentum loss mechanisms during the mass loss on the RGB.

The paper is organized as follows. In Section 5.2, we provide the sample selection from *Gaia* DR2 and the literature. In Sect. 5.3, we describe the EULER/CORALIE observations and data reduction. In Sect. 5.4, we describe our classification method to search for low-mass red giants in binary systems. Finally, in Sect. 5.5, we summarize our results and give an outlook

for the future.

5.2 Target selection

To select the low-mass red giant candidates, we have used the *Gaia* mission data release 2 catalog (DR2; Gaia Collaboration et al., 2018) in combination with synthetic colors for RG stars obtained from the MESA Isochrones and Stellar Tracks (MIST; Choi et al. 2016). First, we applied the criteria on photometric and astrometric quality as described in Lindegren et al. (2018a, Appendix C). Then, we chose objects in the region defined by the four equations below:

$$G_{\text{abs}} = 2.19(G_{BP} - G_{RP}) - 1.95; \quad (5.1)$$

$$G_{\text{abs}} = 1.86(G_{BP} - G_{RP}) - 1.10; \quad (5.2)$$

$$G_{\text{abs}} = 45(G_{BP} - G_{RP}) - 43.9; \quad (5.3)$$

$$G_{\text{abs}} = 28.33(G_{BP} - G_{RP}) - 38.28; \quad (5.4)$$

where $G_{\text{abs}} = \text{phot_g_mean_mag} + 5 \log_{10}(\text{parallax}/1000) + 5$. These cuts focus on the systems prior to the tip of the RGB, and cut off evolved higher-mass systems. The selected region is shown in Fig. 5.1 (left panel) as a red shaded region, which includes a total of 6158 targets. We did an external cross-match with several catalogues using TOPCAT (Taylor, 2005). The literature was searched through the SIMBAD Astronomical Database¹ (Wenger et al., 2000) and we removed 158 outlier objects which turn out to be various types of systems from long period variables (LP) to neutron stars (N^*). The remaining 6 000 targets were then cross-matched with the other large-area surveys using a 5 arcsec aperture in order to clean the sample further. We cross-matched the data with the GALEX DR5 All-sky Imaging Survey (AIS; Bianchi et al., 2011) and found 3 331 objects with NUV and FUV measurements. In order to obtain the near-IR measurements, we cross-matched these objects with the Wide-field Infrared Survey Explorer (WISE; Wright et al., 2010), and found 3 325 targets with their W1 and W2 band measurements. Likewise, the other IR surveys, including Infrared Astronomical Satellite (IRAS; Neugebauer et al., 1984) and the Infrared Astronomical Mission (AKARI; Murakami et al., 2007) were cross-matched to exclude the targets further if they show any excess. The UV excess indicates WD companions while the IR-excess indicates the presence of disks or dust. These kinds of systems (548 stars) were excluded from the survey since we are searching for RG + MS stars that have not yet undergone any type of binary interaction. Finally, we selected 2 777 low-mass RG candidates within 500 pc covering the southern and northern hemispheres. All selected objects have an error on the parallax lower than 10 %.

In this study, we limited ourselves only to the southern hemisphere ($\delta \leq 20^\circ$) and to the smaller volume of 200 pc so that we have a feasible number of systems for a pilot study. Within 200 pc, we have a total of 211 low-mass RG candidates in the southern hemisphere. In Fig. 5.1,

¹<https://simbad.u-strasbg.fr/>

we present the color-magnitude diagram of selected low-mass RG candidates within 200 pc with blue dots (left panel) and their spatial distribution with respect to the galactic coordinate system (right panel).

5.2.1 Spectroscopic binaries from the literature

From available surveys, we searched for known low-mass RGs from the literature applying the similar selection criteria as described in Sect. 5.2. We found a total of 300 binaries detected by different spectroscopic surveys (e.g. Setiawan et al., 2004; Jones et al., 2011; Massarotti et al., 2008; Wittenmyer et al., 2011). Among them, we identified 24 RG binary systems with orbital periods ranging from 100 to 900 days, which could be potential progenitors of wide sdB + MS composite systems produced by the RLOF mechanism. The orbital elements of these systems are listed in Table 5.1 including the orbital period of the binary system (P), the amplitude of the radial velocity curve (K), the eccentricity of the orbit (e), angle of periastron (ω), time of periastron (T_0) and the mass function ($f(m)$).

5.2.2 Binaries from DR3

We made use of Non-single stars catalog (I/357²) from *Gaia* DR3 (Gaia Collaboration et al., 2022) to detect more binary stars within 200 pc. DR3 catalog includes astrometric, spectroscopic, and eclipsing binaries (where solutions from the combinations of astrometry and radial velocities, or eclipsing binary light curves and radial velocities are also provided; Gaia Collaboration et al. 2022). From the *Gaia* DR3 catalog, we found nine binary systems with orbital periods between 100 and 900 days. All these systems and their orbital elements are presented in Table 5.2.

5.3 Observations and data reduction

The spectroscopic observations of the low-mass RGB candidates analyzed in this paper were obtained with the CORALIE echelle spectrograph (Queloz et al., 2001) mounted at the Swiss 1.2-metre Leonhard Euler Telescope at La Silla Observatory in Chile. CORALIE has a resolving power of $R \sim 60\,000$, allowing for a long-term radial velocity precision up to 0.03 km s^{-1} (Queloz et al., 2001). CORALIE is fed by two fibers: a $2''$ diameter on-sky science fiber encompassing the star, and another that can either be connected to a Fabry-Pérot etalon for simultaneous wavelength calibration (used in the case of our survey) or on-sky for background subtraction of the sky flux.

From the 200 pc RG sample, we observed 82 stars with Euler/CORALIE. The observations were done in three different runs. The details of these observations are given in Table 5.3 in

²<https://cdsarc.cds.unistra.fr/viz-bin/cat/I/357>

Table 5.1: Orbital solutions for all known binaries, including the Hipparcos catalog number, the orbital period of the binary system (P), the amplitude of the radial velocity curve (K), the eccentricity of the orbit (e), angle of periastron ω , time of periastron (T_0) and the mass function ($f(m)$).

HD	HIP	P (days)	K (km s^{-1})	e	ω	T_0	$f(m)$ (M_\odot)	Ref.
5516	4463	115.7 (0.2)	17.91 (0.09)	0.003	103	52662	3.3127	2
5877	4618	211.4 (0.3)	12.94 (0.01)	0.1	40.8 (0.6)	5406.3 (0.3)	0.467	3
14355	10548	429.1 (0.3)	6.9 (0.3)	0.3	5.0 (1.9)	5306.6 (1.5)	12.9 (0.2)	3
15755	11840	629.2 (2.7)	10.67	0.14	294.6	53979	0.077	2
27697	20455	522.1 (1.8)	2.84 (0.3)	0.48			0.0084	1
29923	22055	680.1 (25.9)	6.48	0.1	42	53797	0.0189	2
30197	22176	107.6 (0.1)	8.51 (0.15)	0.03	254.5	49457.5	0.00623	2
32008	23221	898.1 (2.7)	5.2	0.17	155.1	51240	0.01248	2
54563	34608	113.4 (0.1)	20.75 (0.04)	0.4				2
62644	37606	380.6 (0.1)	9.84 (0.7)	0.73			0.12	1
65938	39198	365.4 (0.6)	9.56	0.52	108.1	53826.9	0.0208	2
72184	41935	324.1 (16.5)	3.83	0.15	90	54051	0.00183	2
94386	53259	925 (1)	2.18 (0.01)	0.42	37.8 (0.2)	54582.1 (1.2)		2,4
102928	57791	489.6 (0.9)	12.48 (0.2)	0.22	102.4	53114.4	0.0916	2
104358	58601	281.1 (0.3)	1.83 (0.04)	0.24	146 (7)	54836.8 (4.2)		4
133166	73758	97.1 (0.2)	11.82 (0.01)	0.4	53.4 (0.1)	5304.3 (0.1)	0.271	3
136138	74896	508.7 (1.6)	6.19 (0.12)	0.33	39	53751.8	0.01053	2
153438	83224	173.3 (0.3)	8.74 (0.01)	0.3	85.6 (0.3)	5251.3 (0.1)	0.104	3
153956	83138	900.14 (14)	3.36 (0.16)	0.07	338	52956	0.00352	2
172831	91751	485.3 (0.3)	9.68	0.21				2
179799	94521	856.1 (39.1)	5.99 (0.4)	0.66			0.081	1,2
181391	95066	266.5 (0.1)	29.86	0.83				2
199870	103519	635.1 (0.5)	6.44	0.44				2
221625	116243	94.9 (0.1)	36.21	0.52	315.82	53555.4	1.67	2

(1) Setiawan et al. (2004); (2) Massarotti et al. (2008); (3) Bluhm et al. (2016); (4) Wittenmyer et al. (2016)

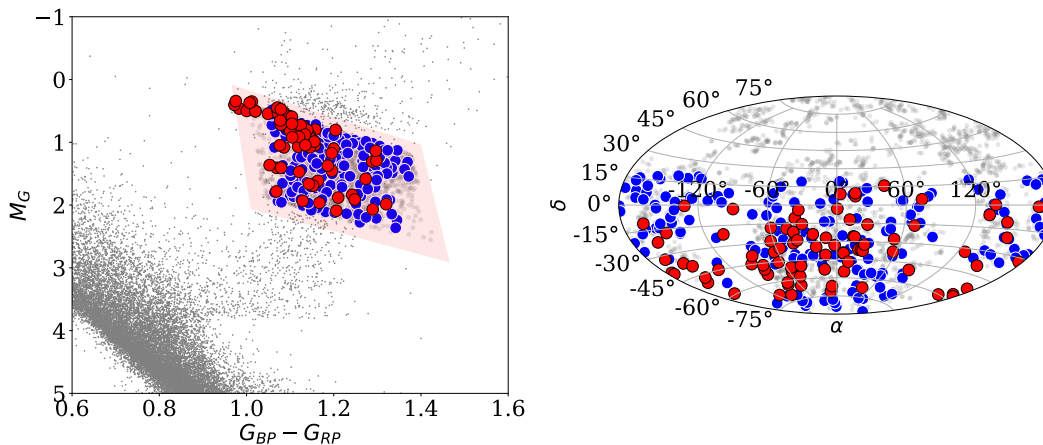


Figure 5.1: LEFT: the colour-magnitude diagram of all low-mass RG candidates within 200 pc (blue dots) from *Gaia* DR2 including only the southern hemisphere stars. As a comparison, the *Gaia* DR2 colour-magnitude diagram of 100 pc clean sample (Sample C in Lindegren et al., 2018a) is shown in grey. Filled red circles show the low-mass RG candidates that were observed with EULER/CORALIE. RIGHT: sky locations (Galactic coordinates, Aitoff projection) of the volume limited low-mass RG sample with respect to the galactic coordinate system using the same color coding.

Table 5.2: Binary systems that are found in DR3, including the name of star, the methods that have been used (astrometric + spectroscopic, astrometric and astrometric, respectively), the orbital period of the system, time of periastron (T_0) and eccentricity of the orbit.

Star	Solution type	Period (days)	T_0 (days)	e
HD2132	AstroSpectroSB1	773	369.636	0.04
HD8410	AstroSpectroSB1	304	30.240	0.22
HD9525	Orbital	582	46.125	0.16
HD36787	AstroSpectroSB1	257	108.608	0.42
HD116338	OrbitalTargetedSearch	248	-34.041	0.84
HD13423	OrbitalTargetedSearch	899	303.991	0.21
HD162049	OrbitalTargetedSearch	713	-83.897	0.45
HD190574	AstroSpectroSB1	552	-90.773	0.70
HD202470	AstroSpectroSB1	488	241.819	0.52

Table 5.3: Observing log of the spectroscopic data obtained for the low-mass red giant stars studied in this work.

Instrument	Date	Range (Å)	S/N
CORALIE	15-16-17 June 2019	3800-6800	30-80
CORALIE	18-19-20 November 2021	3800-6800	50-100
CORALIE	4 April 2022	3800-6800	40-60

cluding the instrument, date, spectral range and the signal-to-noise (S/N) ratio. The observed stars have a photometric G mean magnitude ranging from 5 to 9 with a median of 7.5. The observed sample is depicted in Fig. 5.1 (red dots). In total, we obtained 123 high-resolution CORALIE spectra for 82 stars. We reduced and analyzed the data using the customized CERES pipeline (Brahm et al., 2017), which performs all the extraction processes from basic bias, dark and flat-field corrections (including scattered light) to order tracing, wavelength calibration, and computation of precise radial velocities using the cross-correlation technique. For 38 objects, we obtained two epochs spectra and measured their RV shifts. The RV measurements from multi-epoch CORALIE observations are listed in the tables in the Appendix A. The difference between these two different epochs is defined as ΔCRV and is provided in Table 5.4.

5.3.1 ESO archival data

We used the ESO archive³ to search for high-resolution spectra of stars in our sample. We found a total of 8 stars observed with HARPS and 19 targets observed with FEROS. However, most of them (18 stars) were observed by the EXPRESS RV program (Jones et al., 2011; Soto et al., 2021), whose spectroscopic binaries were presented in Bluhm et al. (2016) and are listed in Table 5.1. One star is in a WD+AFGK binary system (Ren et al., 2020) and two objects are found to be single planet-host stars (Yılmaz et al., 2017; Wittenmyer et al., 2020), which are discarded from our analysis. Finally, our analysis includes six stars observed with FEROS. The CERES pipeline was used to reduce the FEROS spectra as it was for CORALIE data.

5.4 Classification Method

5.4.1 Astrometric excess noise

The high astrometric precision currently made possible by missions such as *Gaia* provides several important parameters. One of the most important parameters for this work is the *Gaia* DR2 astrometric excess noise (AEN), which is a measure of the residuals in the source’s 5-

³http://archive.eso.org/eso/eso_archive_main.html

parameter astrometric solution. It can be used in astrometric binary system classification since a higher AEN value might indicate the presence of unresolved companions. Gandhi et al. (2022) reviewed the details and feasibility of this method, as well as an effective way to use AEN to search for X-ray binaries.

For our study, we made use of AEN to search for low-mass RG binary candidates in our sample. Starting from the 33 known RG binaries (from the literature and DR3), we analyzed their AEN measurements. Out of 33 known binaries 31 have $\text{AEN} \geq 0.4 \text{ mas}$ (see Fig. 5.2 filled circles). Given that more than 90% of the known binaries have $\text{AEN} \geq 0.4 \text{ mas}$, we have chosen this value of AEN as a threshold to consider that a star is a potential binary candidate. In other words, these targets will be further followed up in order to confirm the binarity and finally obtain orbital periods.

5.4.2 The Renormalised Unit Weight Error (RUWE)

The *Gaia* data product known as the Renormalised Unit Weight Error (RUWE) is a measure used to filter out sources with potentially bad astrometry, in particular spurious parallaxes or proper motions (see for details, Lindegren et al., 2018b). The RUWE is expected to be around 1.0 for sources where the single-star model provides a good fit to the astrometric observations. If a value is significantly greater than 1.0, that could indicate that the source is not a single object or otherwise problematic for the astrometric solution. Therefore, we used RUWE to search for low-mass RG binary candidates in our sample. We examined the RUWE measurements of the known RG binaries, and we found that 93% of the known binary systems have RUWE bigger than 1.4. Therefore we used $\text{RUWE} \geq 1.4$ as a threshold to consider the object as a binary candidate.

To put this in a perspective, we have plotted known binary systems as well as observed stars with CORALIE and FEROS in AEN and RUWE parameters space indicating our selection threshold in Fig. 5.2. The gray shaded area depicts the systems that are potential binaries based on our selection criteria. As can be seen in Fig. 5.2, all known binaries fall on the grey shaded area.

5.4.3 Radial velocities from CORALIE, FEROS, DR2 and DR3

In order to define the binary fraction in our observed sample, we made use of the radial velocity measurements from CORALIE, FEROS, *Gaia* DR2 and DR3. The RV measurements from DR2 and DR3 are depicted in Fig. 5.2 (right panel), where we show known binaries with filled blue circles and observed stars with open blue circles. As can be seen in Fig. 5.2 (right panel), DR2 and DR3 measurements do not differ.

With CORALIE, we obtained two different epochs of spectra for 38 stars, which are re-

ported in Table 5.4 where we also listed the AEN value, ΔCRV and the corresponding uncertainty. If the difference between two CORALIE measurements is bigger or equal that 0.1 km s^{-1} ($\Delta\text{CRV} \geq 0.1 \text{ km s}^{-1}$), we consider that the object is a potential binary candidate. Out of these 38 observed objects, we found 17 stars that show ΔCRV above the threshold and, therefore, could be potential binary systems.

We obtained a single epoch CORALIE spectrum for 44 stars, which were combined with RV measurements from *Gaia* DR2 in order to measure RV differences. Likewise, a single epoch archival FEROS spectra for 6 stars were combined with RV measurements from *Gaia* DR2. In Table 5.5, we show the difference between the CORALIE/FEROS RV and the DR2 RV measurements (ΔRV) of all the single epoch observed stars from the ground together with their AEN and RUWE measurements. Given that the errors in *Gaia* DR2 measurements vary from 0.2 to 2.5 km s^{-1} , we have chosen to use the 3σ criteria as the threshold. In other words, if the RV difference between ground base and DR2 RV measurements is three times greater than its RV error, we consider the object as a potential binary candidate.

5.4.4 Classification

By combining three sets of measurements, AEN, RUWE and RV, we defined three categories that classify a star by its likelihood to be a binary candidate. The stars that have been observed from the ground are divided into three categories. The stars that have at least two of the parameters (AEN/RUWE and RV variation) larger than the threshold we classify as binary candidates and assign them a category 1. The stars that have one of the parameters above the threshold (AEN/RUWE or RV variation) we assign them category 2 as they are likely to be binary candidates. The third group (category 3) includes targets with no significant AEN, RUWE or RV variations.

In the observed set, we found that 24 stars show $\text{AEN} \geq 0.4$, out of which 18 stars also present significant radial velocity variations. It is these 18 stars that we assigned a category 1 as they are binary candidates which will be priority targets for follow-up observations. Furthermore, we found 18 stars that are potential binary candidates (category 2) out of which 13 targets show only significant RV variations, and 5 stars show solely astrometric excess noise above the threshold of 0.4 mas . These 18 stars are also added to the follow-up observations as additional observations are needed to confirm their binarity.

Furthermore, three stars (HD119483, HD149649 and CD-397574) that were observed with CORALIE in two epochs show RV variations of 0.061 , 0.046 and -0.046 km s^{-1} , respectively. As these variations are just below the RV threshold of 0.1 km s^{-1} we marked these stars as potential follow-up candidates. Moreover there is one target, HD120144, that has RUWE of 1.37 , while it does not show either AEN or RV variation. We consider this target as a possible binary candidate (category 2), which should also be observed in the future.

Lastly, using the same classification method, we classified 6 FEROS targets that were obtained from the ESO archive. One of them corresponds to a binary system listed in the *Gaia*

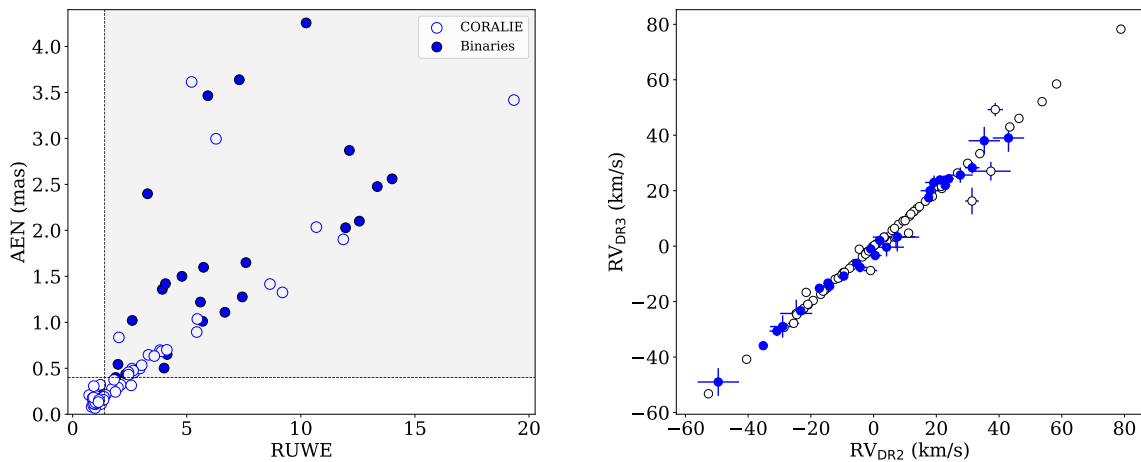


Figure 5.2: LEFT: AEN versus RUWE, including known binaries from the literature and DR3 (filled blue circles) and observed stars (open blue circles). AEN of 0.4 mas is represented by the horizontal black dashed line, and RUWE of 1.4 is represented by the vertical black dashed line. The gray-shaded area displays all the stars that are most likely in binary systems. RIGHT: Radial velocity measurements from DR3 (y-axis) as a function of radial velocity measurements from DR2 (x-axis) using the same color coding.

DR3 catalogue, and one more was classified in category 1, i.e., it is most likely a binary candidate.

5.5 Conclusion

Based on the *Gaia* DR2 color-magnitude diagram, we select a sample of 211 low-mass RG candidates within 200 pc in order to search for low-mass RGB + MS binary systems with orbital periods between 100 and 900 days, which are potential progenitors of wide binary sdB systems. From the literature, we found 24 such systems. Furthermore, nine long-period (248 to 898 days) binary systems were identified with orbital parameters from DR3. In addition, we obtained CORALIE spectroscopic data for the 82 stars and single-epoch FEROS archive spectra for 6 stars among this sample. We combined the resulting CORALIE and FEROS RVs with the DR2 and DR3 radial velocity measurements, as well as AEN and RUWE values, to search for potential binary candidates. From these combined datasets we defined three different categories based on their likelihood of being a binary candidate. The first group includes binary candidates since they have a large RV variation and a high AEN/RUWE. The second group contains likely binary candidates since they show either high RV or have AEN/RUWE values above the threshold. The third group includes the stars that do show neither RV nor AEN/RUWE variations, which accounts for 53% of the observed sample, or 47 stars. The ob-

Table 5.4: Binary classification of low-mass red giant stars reported in this paper with two CORALIE epochs spectra, including the name of the observed star, the astrometric excess noise (AEN) measurements from *Gaia* eDR3, the difference between two CORALIE RV measurements (Δ CRV), the errors on RV and the classification number.

Star	Δ CRV (km s^{-1})	eRV (km s^{-1})	AEN (mas)	RUWE	Category
HD112521	3.715	0.04	0.68	3.899	1
HD167936	-16.23	0.05	1.42	8.646	1
HD305357	4.276	0.1	0.46	2.447	1
HD214941	3.44	0.06	0.43	2.446	1
HD217614	-10.76	0.05	2.04	10.68	1
HD201013	-5.57	0.04	0.7	4.128	1
HD206005	-0.49	0.03	0.37	1.814	1
HD71464	22.710	0.04	0.15	1.285	2
HD116338	1.358	0.03	0.21	1.445	2
HD136350	-9.882	0.05	0.09	0.998	2
HD139137	0.955	0.06	0.31	2.567	2
HD204381	-0.012	0.04	0.84	2.027	2
HD85885	-0.198	0.04	0.24	1.872	2
HD102805	0.518	0.04	0.09	0.924	2
HD170105	1.067	0.04	0.1	0.897	2
HD157527	-0.306	0.04	0.21	0.724	2
HD99891	-0.136	0.04	0.17	1.352	2
HD120144	0.013	0.04	0.19	1.373	2
HD119483	0.061	0.04	0.15	1.207	3
HD149649	0.046	0.04	0.11	0.954	3
CD-397574	-0.046	0.05	0.08	0.984	3
CD-324787	-0.033	0.05	0.09	0.981	3
HD102216	-0.030	0.04	0.09	1.027	3
HD107045	-0.002	0.04	0.12	0.975	3
HD114430	0.003	0.04	0.12	0.966	3
HD116845	-0.007	0.04	0.1	0.924	3
HD122568	-0.018	0.04	0.11	1.253	3
HD124461	-0.008	0.04	0.14	1.097	3
HD162157	0.001	0.04	0.11	0.966	3
HD167768	0.001	0.05	0.18	0.872	3
HD168839	-0.022	0.04	0.08	0.828	3
HD171864	-0.015	0.04	0.13	1.041	3
HD176771	0.030	0.04	0.16	1.003	3
HD191716	-0.007	0.04	0.12	1.02	3
HD96627	-0.010	0.04	0.16	1.259	3
HD99783	-0.007	0.04	0.12	0.959	3
HD116948	0.013	0.04	0.11	-	3
HD162984	-0.035	0.04	0.11	0.945	3

Table 5.5: Binary classification of low-mass red giant stars reported in this paper with a single CORALIE or FEROS epoch spectra, including the name of the observed star, the astrometric excess noise (AEN) measurements from *Gaia* eDR3, the difference between the CORALIE/FEROS RV and the DR2 RV measurements (Δ RV), the RV error from *Gaia* DR2 (eRV) and the classification number.

Star	Δ RV (km s^{-1})	eRV (km s^{-1})	AEN (mas)	RUWE	Category
HD2259	1.36	0.50	0.45	2.695	1
HD2132	6.27	1.47	1.90	11.862	1 (Binary)
HD6254	-1.61	0.58	0.50	2.6	1
HD74686	10.23	2.45	3.42	19.337	1
HD83674	-2.99	0.27	0.48	2.651	1
HD8410	9.41	0.53	1.33	9.195	1 (Binary)
HD9525	-5.40	1.04	3.00	6.283	1 (Binary)
HD10537	-8.28	0.15	3.61	5.214	1
HD220864	1.82	0.15	0.63	3.578	1
HD29821	-8.29	0.27	0.53	3.027	1
HD21340	-0.53	0.18	0.50	2.95	1
HD169767	-11.6	0.7	0.907	2.618	1
HD4145	0.90	0.15	0.20	0.993	2
HD5676	4.18	0.43	0.32	2.104	2
HD6030	1.26	1.55	0.29	1.984	2
HD22792	-2.63	0.17	0.17	1.229	2
HD18278	-0.29	0.23	1.04	5.464	2
HD36787	-0.24	1.18	0.70	3.83	2 (Binary)
HD6019	-0.53	0.27	0.65	3.323	2
TYC5464-59-1	-0.22	2.09	0.89	5.437	2
HD10268	-0.22	0.15	0.28	1.719	2
HD193937	-0.18	0.18	0.16	1.354	2
HD93410	0.18	0.17	0.133	1.06	2
HD219263	0.11	0.18	0.32	1.212	3
HD745	0.08	0.18	0.17	1.05	3
HD3303	-0.04	0.17	0.15	0.888	3
HD16665	-0.36	0.17	0.15	1.154	3
HD27956	-0.24	0.12	0.16	1.089	3
HD192232	-0.06	0.13	0.15	0.986	3
HD213986	-0.13	0.16	0.18	0.914	3
HD220096	-0.35	0.17	0.31	0.926	3
HD179120	-0.37	0.13	0.11	0.995	3
HD187562	-0.87	0.25	0.07	0.982	3
HD188476	-0.35	0.14	0.11	0.987	3
HD189365	-0.12	0.14	0.11	0.96	3
HD193407	-0.08	0.15	0.12	1.013	3
HD195189	-0.09	0.15	0.13	0.966	3
HD197790	-0.21	0.14	0.13	1.033	3
HD202704	-0.17	0.18	0.14	1.027	3
HD203086	-0.23	0.15	0.13	1.044	3
HD205588	-0.18	0.17	0.12	1.005	3
HD207920	-0.38	0.16	0.12	0.937	3
HD209154	-0.33	0.15	0.13	0.997	3
HD219026	-0.30	0.14	0.16	1.149	3
HD223700	-0.20	0.14	0.13	1.13	3
HD4737	-0.30	0.15	0.16	1.093	3
HD102888	-0.08	0.15	0.107	0.889	3
HD221214	0.03	0.16	0.118	0.957	3
HD84257	-0.03	0.16	0.121	0.972	3
HD90317	0.01	0.18	0.128	0.991	3

served sample demonstrates that 47% of the observed stars (41 out of 88) most likely have binary signatures. This result is not unexpected considering that about half of low-mass main sequence stars are found in binary systems (Raghavan et al., 2010).

In future work, we will continue observing the selected binary candidates to confirm their binarity and constrain their orbital parameters. Furthermore, the spectra that we obtained will be used to derive accurate atmospheric parameters, including the effective temperature, surface gravity, rotational velocity, microturbulence and metallicity. Also, we will derive accurate radii and masses by deriving the radius from an SED fit for the stars that are presented in this work. We note that our sample might suffer from possible contamination from the red clump (RC) stars, and this contamination can be up to 30% as shown by Girardi (2016). Removing this contamination to define the low-mass RG stars is not easy since they cannot be distinguished by either color-magnitude diagrams or spectroscopic surveys (e.g. Masseron & Hawkins, 2017). The way to distinguish these two groups is to use asteroseismology. For instance, Bedding et al. (2011) showed that the seismic parameter called period spacings can be used to distinguish RGB stars, burning only hydrogen in the shell, from RC stars that also burn helium in their cores. In the future, we will make use of this advanced technique using high-precision photometry for the targets that have been observed during TESS and K2 missions. There are several ongoing large-scale, ground-based surveys focused on obtaining high-resolution spectroscopy, including GALAH ($12 \leq V \leq 14$), SDSS V ($11 \leq H \leq 14$) and *Gaia*-ESO (variable brightness ranges). These surveys will be important to constrain the orbital parameters of promising targets that are classified as 1 and 2 in this work.

Conclusions and future prospects

6.1 Summary and conclusions

Based on the unprecedented high-quality and contiguous photometric measurements from the spacecrafts coupled with low-to-high resolution spectroscopic measurements from the ground, this thesis reports on a detailed investigation of compact pulsating stars sdBs and GW Vir WDs. Furthermore, we compiled a sample of low-mass red giant stars in order to search for the progenitors of hot subdwarf B stars in long-period period binary systems. We summarize our new contributions to the field in this final chapter and offer some concluding thoughts on future research avenues opened up by this dissertation.

In Chapter 2, we present the analysis of data collected for five pulsating hot subdwarf B stars, observed with the TESS mission. Four of the five analyzed stars are new detections of long-period pulsating sdB (V1093 Her) stars. This high-duty cycle space photometry delivered by the TESS mission provides data of excellent quality for detection and identification of the pulsational modes in hot subdwarf stars. From the spectroscopic ground based data, we derived atmospheric parameters for all five stars by fitting synthetic spectra to the newly obtained low-resolution Dupont/B&C and NTT/EFOSC2 spectra. From the TESS light curves we detected 73 pulsating frequencies out of which 49 were identified as $l = 1$ modes based on the asteroseismic method of asymptotic period spacing. We did not detect p-modes in any of the stars analyzed in this thesis. We computed stellar evolution models with LPCODE stellar evolution code, and computed $l = 1$ g-mode frequencies with the adiabatic nonradial pulsation code LP-PUL. We compared the derived mean period spacings (ΔP) of dipole g-modes derived from TESS observations for the five sdBV stars of our sample and 33 more sdBV stars found in the literature with the predictions of the adiabatic pulsation computations performed on stellar evolutionary models. In agreement with expectations from theoretical arguments and previous asteroseismological works (e.g. Castellani et al., 1985), we find that models relying on a simplistic implementation of the Schwarzschild criterion lead to small convective cores and values of ΔP which are too low to match the observations. On the other hand, mod-

els with a standard treatment of convective boundary mixing at the convective core are able to match the observed values of ΔP , although more intense convective boundary mixing cannot be discarded.

In Chapter 3, we reported the discovery of two new GW Vir stars with TESS data, TIC333432673 and TIC095332541. Both stars are characterized by $T_{\text{eff}} = 120,000 \pm 10,000$ K and $\log g = 7.5 \pm 0.5$ K, and $M_{\star} = 0.58_{-0.08}^{+0.16} M_{\odot}$, only differing in their surface He/C composition. We presented observations from the extended TESS mission in both 120 sec short-cadence and 20 sec ultra-short-cadence for both targets. We applied the tools of asteroseismology with the aim of deriving their structural parameters and seismological distances. The asteroseismological analysis of TIC 333432673 allowed us to find a constant period spacing compatible with a stellar mass of $M_{\star} \sim 0.60 - 0.61 M_{\odot}$, and an asteroseismological model for this star with a stellar mass of $M_{\star} = 0.58 \pm 0.02 M_{\odot}$, as well as a seismological distance of $d = 459_{-156}^{+188}$ pc. For this star, there is an agreement between the different methods to infer the stellar mass, and also between the seismological distance and that measured with Gaia ($d_{\text{Gaia}} = 389_{-5.2}^{+5.6}$ pc). For TIC095332541, we find a possible period spacing that suggests a stellar mass of $M_{\star} \sim 0.55 - 0.57 M_{\odot}$. Unfortunately, we were not able to find an asteroseismological model for this star.

In Chapter 4, we presented the discovery of two additional GW Vir stars, TIC0403800675 and TIC1989122424 employing observations collected by TESS. Their TESS light curves reveal the presence of oscillations with periods in a narrow range between 400 and 410 s, which are associated with typical g-modes. The derived spectroscopic parameters demonstrate that TIC0403800675 and TIC1989122424 are identical in terms of surface temperature and surface gravity ($T_{\text{eff}} = 110,000 \pm 10,000$ K and $\log g = 7.5 \pm 0.5$) and they are only different regarding the surface C and He abundance. By performing a fit to the SEDs and parallaxes we found for both stars radii and luminosities of $R_{\star} = 0.019 \pm 0.002 R_{\odot}$ and $\log(L_{\star}/L_{\odot}) = 1.68_{-0.24}^{+0.15}$, respectively. Employing state-of-the-art evolutionary tracks of PG1159 stars, we found a stellar mass of $0.56_{-0.05}^{+0.15} M_{\odot}$ from the $\log g - T_{\text{eff}}$ diagram, and $0.60_{-0.09}^{+0.11} M_{\odot}$ from the Hertzsprung Russell diagram for both stars. Unfortunately, due to the fact that both stars exhibit only two periods each, it is not possible to perform an asteroseismological modeling, something that will have to wait for more periods to be detected in future observations. Unfortunately, because each star's power spectrum contains only two oscillation frequencies, we are unable to perform asteroseismic modeling. We hope to detect more periods in the future so that we can investigate the internal structure and evolutionary state of these stars using asteroseismological tools.

Finally, in Chapter 5, using data from *Gaia* DR2, we compiled a sample of low-mass red giant stars in order to search for the progenitors of hot subdwarf B stars in long-period binary systems. We looked for low-mass red giant + main sequence binary systems with long periods (100-900 days) in several ground-based spectroscopic surveys. We presented 33 low-mass red giant stars that are in long-period binary systems from both the ground base surveys and *Gaia* Data Release 3 (DR3). We used these systems as a calibrator for determining the most

efficient way to apply the binary selection method. The CORALIE echelle spectrograph was used to do spectroscopic observations for 88 low-mass RGB candidates. These measurements were coupled with the astroseismic excess noise measurements and RUWE from *Gaia* eDR3 to define the binary selection method. The observed sample shows that 41 out of 88 stars, or 47% of the sample, most likely have binary signatures. Given that about half of low-mass main sequence stars are found in binary systems (Raghavan et al., 2010), this outcome is not surprising.

6.2 Future prospects

The TESS space mission is demonstrating that it significantly contributes to pulsating sdBs and WDs asteroseismology. Ongoing surveys like TESS, *Gaia* and ZTF will continue to make data available to the general public. The possibility of discovering and characterizing even more pulsating sdBs and H-deficient WDs is only going to increase. With the future space missions, such as PLATO (PLANetary Transits and Oscillation of Stars), as well as ground based surveys such as LSST and SDDS-V, there will be an immense amount of data waiting to be analyzed which will inevitably lead to new discoveries in the near future.

Since none of the sdB pulsating stars in this thesis have been observed in multiple sectors by TESS, it is challenging to pinpoint rotational multiplets. In the case of GW Vir stars, we were able to set an upper limit for the rotation period of the core. Therefore, it is essential to look into every pulsating sdB and WD that are in the TESS continuous viewing zone. Better frequency resolution and lower noise levels can be attained with more data points and a longer baseline, as is the case for stars that have been observed by TESS in multiple sectors, making the detection of potential rotational multiples viable for a number of targets. I particularly believe that it will be possible to detect rotational multiplets and strengthen the mode identification for stars that are within the TESS continuing viewing zone. Five stars in the TESS continuing viewing zone have already been examined; one of them exhibits rotational multiplets that will be presented soon (Uzundag et al. 2022, in prep.).

In the case of GW Vir stars, they evolve quickly, resulting in a significant period change due to cooling and contraction, which should be detected in a few decades. It is possible to measure the rates of period change of pulsations in GW Vir stars over the course of several decades of observation, which is related to evolutionary (cooling) effects. The four stars that I discuss in this thesis are suitable candidates, and it is possible to check on them at least once a year to look for signs of evolution.

Concerning the volume limited sample of low-mass red giant sample, I will soon be able to calculate precise atmospheric parameters from the spectra I obtained, such as the effective temperature, surface gravity, rotational velocity, and metallicity. Additionally, by obtaining the radius from an SED fit for the stars that are discussed in this work, I will be able to calculate precise radii and masses.

The red clump stars may be a source of contamination for the RGB sample presented in Chapter 5, and this contamination can be as high as 30% as shown by Girardi (2016). Bedding et al. (2011) demonstrated how to distinguish between RC stars, which also burn helium in their cores, and RGB stars, which burn only hydrogen in their shells, using the seismic parameter known as period spacings. In our upcoming work, I will use this cutting-edge method with highly accurate photometry for the targets that have been observed by Kepler/K2 and TESS missions. Additionally, future space telescopes like the PLATO mission will provide continuous photometry, increasing the number of stars that can be observed. A number of large-scale ground-based surveys are currently being conducted with the goal of obtaining high-resolution spectroscopy including GALAH ($12 \leq V \leq 14$), SDSS-V ($11 \leq H \leq 14$) and *Gaia*-ESO (variable brightness ranges). These observations are crucial for constraining the orbital periods of the systems.

A

Radial velocity measurements

Table A.1: Radial velocity measurements for all stars that are presented in this work.

Star	JD -2450000	RV (km s ⁻¹)	RV Error (km s ⁻¹)	Instrument
HD201013	8650.86	-20.16	0.01	CORALIE
	9538.56	-25.73	0.01	CORALIE
HD204381	8650.82	-20.96	0.01	CORALIE
	9538.57	-20.99	0.01	CORALIE
HD206005	8650.85	-9.75	0.01	CORALIE
	9539.52	-9.26	0.01	CORALIE
HD214941	8650.91	5.07	0.01	CORALIE
	9538.57	1.63	0.01	CORALIE
HD217614	8650.79	-13.93	0.01	CORALIE
	9538.56	-24.69	0.01	CORALIE
CD-324787	8649.47	0.7677	0.0053	CORALIE
	9673.49	0.7348	0.0048	CORALIE
CD-397574	8650.60	6.0176	0.0043	CORALIE
	9673.67	5.9716	0.0039	CORALIE
HD102216	8649.58	17.9042	0.004	CORALIE
	9673.70	17.8746	0.0031	CORALIE
HD102805	8651.54	-11.5754	0.0039	CORALIE
	9673.64	-11.0578	0.0032	CORALIE
HD107045	8650.57	-11.6511	0.0033	CORALIE
	9673.68	-11.6529	0.0032	CORALIE
HD112521	8651.57	7.0568	0.0042	CORALIE
	9673.73	10.7717	0.0033	CORALIE
HD114430	8651.58	-15.8567	0.0045	CORALIE
	9673.72	-15.8535	0.0035	CORALIE

Table A.2: Radial velocity measurements for all stars that are presented in this work.

Star	JD -2450000	RV (km s ⁻¹)	RV Error (km s ⁻¹)	Instrument
HD116338	8651.59	-30.5275	0.0043	CORALIE
	9673.73	-29.1692	0.0031	CORALIE
HD116845	8650.63	-6.3724	0.0036	CORALIE
	9673.74	-6.3798	0.0038	CORALIE
HD116948	8651.56	-18.5105	0.0039	CORALIE
	9673.75	-18.4976	0.0032	CORALIE
HD119483	8649.55	11.7157	0.011	CORALIE
	9673.76	11.7758	0.003	CORALIE
HD120144	8650.65	-0.6528	0.0031	CORALIE
	9673.76	-0.6394	0.0032	CORALIE
HD122568	8651.61	17.9469	0.0042	CORALIE
	9673.78	17.9291	0.0031	CORALIE
HD124461	8650.67	-40.6677	0.0029	CORALIE
	9673.79	-40.6757	0.0032	CORALIE
HD136350	8649.64	3.7816	0.0048	CORALIE
	9673.81	-6.1007	0.0034	CORALIE
HD139137	8650.69	-39.984	0.0061	CORALIE
	9673.82	-39.0291	0.0068	CORALIE
HD149649	8651.64	7.936	0.005	CORALIE
	9673.82	7.9822	0.0035	CORALIE
HD157527	8649.60	-52.1753	0.0044	CORALIE
	9673.85	-52.4809	0.0034	CORALIE
HD162157	8651.68	-21.0394	0.0042	CORALIE
	9673.84	-21.0381	0.0032	CORALIE

Table A.3: Radial velocity measurements for all stars that are presented in this work.

Star	JD -2450000	RV (km s ⁻¹)	RV Error (km s ⁻¹)	Instrument
HD162984	8649.62	-9.9796	0.0046	CORALIE
	9673.85	-10.0147	0.0032	CORALIE
HD167768	8650.81	1.6223	0.0053	CORALIE
	9673.89	1.6237	0.0048	CORALIE
HD167936	8651.70	-21.1005	0.0065	CORALIE
	9673.86	-37.3306	0.0057	CORALIE
HD168839	8650.89	14.4398	0.0032	CORALIE
	9673.87	14.4181	0.0028	CORALIE
HD170105	8651.66	30.6076	0.0038	CORALIE
	9673.86	31.6746	0.0031	CORALIE
HD171864	8650.70	-17.2808	0.0027	CORALIE
	9673.87	-17.2956	0.0029	CORALIE
HD176771	8649.70	-10.2239	0.006	CORALIE
	9673.88	-10.1944	0.0036	CORALIE
HD191716	8650.80	-7.8355	0.0029	CORALIE
	9673.88	-7.8428	0.0031	CORALIE
HD305357	8650.52	-0.7367	0.0057	CORALIE
	9673.58	3.5397	0.0045	CORALIE
HD71464	8649.50	16.7708	0.0088	CORALIE
	9673.53	39.4804	0.0049	CORALIE
HD85885	8650.55	27.0625	0.0063	CORALIE
	9673.56	26.8646	0.0052	CORALIE
HD96627	8651.47	3.2028	0.0036	CORALIE
	9673.60	3.1933	0.0032	CORALIE
HD99783	8649.60	12.5647	0.005	CORALIE
	9673.61	12.5581	0.0034	CORALIE
HD99891	8651.50	-14.3367	0.004	CORALIE
	9673.62	-14.4727	0.0032	CORALIE

Bibliography

- Aerts C., 2019, arXiv e-prints, arXiv:1912.12300
- Aerts C., 2021, *Reviews of Modern Physics*, 93, 015001
- Aerts C., Christensen-Dalsgaard J., Kurtz D. W., 2010, *Asteroseismology*
- Aller A., Lillo-Box J., Jones D., Miranda L. F., Barceló Forteza S., 2020, *A&A*, 635, A128
- Althaus L. G., Córscico A. H., Isern J., García-Berro E., 2010a, *The Astronomy and Astrophysics Review*, 18, 471
- Althaus L. G., Córscico A. H., Isern J., García-Berro E., 2010b, *A&A Rev.*, 18, 471
- Althaus L. G., Serenelli A. M., Panei J. A., Córscico A. H., García-Berro E., Scóccola C. G., 2005a, *A&A*, 435, 631
- Althaus L. G., Serenelli A. M., Panei J. A., Córscico A. H., García-Berro E., Scóccola C. G., 2005b, *A&A*, 435, 631
- Andrae R., 2010, arXiv e-prints, arXiv:1009.2755
- Bachulski S., Baran A. S., Jeffery C. S., Østensen R. H., Reed M. D., Telting J. H., Kuutma T., 2016, *Acta*, 66, 455
- Bailer-Jones C. A. L., Rybizki J., Fouesneau M., Demleitner M., Andrae R., 2021, *VizieR Online Data Catalog*, I/352
- Baran A., Pigulski A., Koziel D., Ogłóza W., Silvotti R., Zoła S., 2005, *MNRAS*, 360, 737
- Baran A. S., 2012, *Acta*, 62, 179
- Baran A. S. et al., 2011, *MNRAS*, 414, 2871

- Baran A. S., Reed M. D., Østensen R. H., Telting J. H., Jeffery C. S., 2017, *A&A*, 597, A95
- Baran A. S., Sahoo S. K., Sanjayan S., Ostrowski J., 2021, *MNRAS*, 503, 3828
- Baran A. S., Telting J. H., Jeffery C. S., Østensen R. H., Vos J., Reed M. D., Vacković, M., 2019, *MNRAS*, 489, 1556
- Bedding T. R. et al., 2011, *Nature*, 471, 608
- Bell K. J. et al., 2019, *A&A*, 632, A42
- Bell K. J., Hermes J. J., Bischoff-Kim A., Moorhead S., Montgomery M. H., Østensen R., Castanheira B. G., Winget D. E., 2015, *The Astrophysical Journal*, 809, 14
- Bell K. J., Hermes J. J., Vanderbosch Z., Montgomery M. H., Winget D. E., Dennihy E., Fuchs J. T., Tremblay P.-E., 2017, *ApJ*, 851, 24
- Bianchi L., Conti A., Shiao B., 2014, *VizieR Online Data Catalog*, 2335, 0
- Bianchi L., Herald J., Efremova B., Girardi L., Zobot A., Marigo P., Conti A., Shiao B., 2011, *Ap&SS*, 335, 161
- Blöcker T., 2001, *Ap&SS*, 275, 1
- Bluhm P. et al., 2016, *A&A*, 593, A133
- Bognár Z., Kalup C., Sódor Á., 2021, *arXiv e-prints*, arXiv:2103.17192
- Bognár Z. et al., 2020, *A&A*, 638, A82
- Borucki W. J. et al., 2010a, *Science*, 327, 977
- Borucki W. J. et al., 2010b, *Science*, 327, 977
- Bossini D. et al., 2015, *MNRAS*, 453, 2290
- Brahm R., Jordán A., Espinoza N., 2017, *PASP*, 129, 034002
- Buzzoni B. et al., 1984, *The Messenger*, 38, 9
- Capitanio L., Lallement R., Vergely J. L., Elyajouri M., Monreal-Ibero A., 2017, *A&A*, 606, A65
- Castellani V., Chieffi A., Tornambe A., Pulone L., 1985, *ApJ*, 296, 204
- Castellani V., Giannone P., Renzini A., 1971, *Ap&SS*, 10, 340
- Chambers K. C. et al., 2016, *arXiv e-prints*, arXiv:1612.05560
- Charpinet S. et al., 2019, *A&A*, 632, A90

-
- Charpinet S., Brassard P., Van Grootel V., Fontaine G., 2014, in *Astronomical Society of the Pacific Conference Series*, Vol. 481, van Grootel V., Green E., Fontaine G., Charpinet S., eds, 6th Meeting on Hot Subdwarf Stars and Related Objects, p. 179
- Charpinet S., Fontaine G., Brassard P., Chayer P., Rogers F. J., Iglesias C. A., Dorman B., 1997, *ApJ*, 483, L123
- Charpinet S., Fontaine G., Brassard P., Dorman B., 1996, *ApJ*, 471, L103
- Charpinet S., Fontaine G., Brassard P., Dorman B., 2000, *ApJS*, 131, 223
- Charpinet S., Fontaine G., Brassard P., Dorman B., 2002, *ApJS*, 139, 487
- Charpinet S., Giammichele N., Zong W., Grootel V. V., Brassard P., Fontaine G., 2018, *Open Astronomy*, 27, 112
- Charpinet S. et al., 2011, *A&A*, 530, A3
- Chen X., Han Z., Deca J., Podsiadlowski P., 2013, *MNRAS*, 434, 186
- Choi J., Dotter A., Conroy C., Cantiello M., Paxton B., Johnson B. D., 2016, *ApJ*, 823, 102
- Clemens J. C., Crain J. A., Anderson R., 2004, in *Society of Photo-Optical Instrumentation Engineers (SPIE) Conference Series*, Vol. 5492, Moorwood A. F. M., Iye M., eds, *Ground-based Instrumentation for Astronomy*, p. 331
- Constantino T., Campbell S. W., Christensen-Dalsgaard J., Lattanzio J. C., Stello D., 2015, *MNRAS*, 452, 123
- Constantino T., Campbell S. W., Lattanzio J. C., van Duijneveldt A., 2016, *MNRAS*, 456, 3866
- Copperwheat C. M., Morales-Rueda L., Marsh T. R., Maxted P. F. L., Heber U., 2011a, *MNRAS*, 415, 1381
- Copperwheat C. M., Morales-Rueda L., Marsh T. R., Maxted P. F. L., Heber U., 2011b, *MNRAS*, 415, 1381
- Córsico A. H., 2020, *Frontiers in Astronomy and Space Sciences*, 7, 47
- Córsico A. H., Althaus L. G., 2005, *A&A*, 439, L31
- Córsico A. H., Althaus L. G., 2006a, *A&A*, 454, 863
- Córsico A. H., Althaus L. G., 2006b, *A&A*, 454, 863
- Córsico A. H., Althaus L. G., Miller Bertolami M. M., 2006, *A&A*, 458, 259
- Córsico A. H., Althaus L. G., Miller Bertolami M. M., Kepler S. O., 2019, *A&A Rev.*, 27, 7

- Córsico A. H., Althaus L. G., Miller Bertolami M. M., Werner K., 2007, *A&A*, 461, 1095
- Córsico A. H. et al., 2020, arXiv e-prints, arXiv:2011.03629
- Córsico A. H. et al., 2021a, *A&A*, 645, A117
- Córsico A. H. et al., 2021b, arXiv e-prints, arXiv:2111.15551
- Córsico A. H. et al., 2022, *A&A*, 659, A30
- Costa J. E. S. et al., 2008, *A&A*, 477, 627
- Cox A. N., 2000, *Allen's astrophysical quantities*
- Culpan R., Geier S., Pelisoli I., Reindl N., Gentile Fusillo N., Vorontseva A., 2022, arXiv e-prints, arXiv:2203.07938
- Córsico A. H., Althaus L. G., Miller Bertolami M. M., Kepler S. O., 2019, *The Astronomy and Astrophysics Review*, 27
- Dai M., Chen X., Wang K., Luo Y., Wang S., Deng L., 2022, arXiv e-prints, arXiv:2201.03721
- D'Cruz N. L., Dorman B., Rood R. T., O'Connell R. W., 1996, *ApJ*, 466, 359
- De Gerónimo F. C., Battich T., Miller Bertolami M. M., Althaus L. G., Córsico A. H., 2019, *A&A*, 630, A100
- Dorman B., Rood R. T., 1993, *ApJ*, 409, 387
- Dorsch M., Reindl N., Pelisoli I., Heber U., Geier S., Istrate A. G., Justham S., 2022, *A&A*, 658, L9
- Dziembowski W., 1977, *Acta*, 27, 203
- Edelmann H., Heber U., Altmann M., Karl C., Lisker T., 2005, *A&A*, 442, 1023
- Edelmann H., Heber U., Hagen H. J., Lemke M., Dreizler S., Napiwotzki R., Engels D., 2003, *A&A*, 400, 939
- Efron B., 1979, *Ann. Statist.*, 7, 1
- Feige J., 1958, *ApJ*, 128, 267
- Fitzpatrick E. L., 1999, *PASP*, 111, 63
- Fontaine G., Brassard P., Charpinet S., Green E. M., Chayer P., Billères M., Randall S. K., 2003, *ApJ*, 597, 518
- Foster H. M., Reed M. D., Telting J. H., Østensen R. H., Baran A. S., 2015, *ApJ*, 805, 94

Freytag B., Ludwig H. G., Steffen M., 1996, *A&A*, 313, 497

Fujimoto M. Y., 1977, *PASJ*, 29, 331

Gabriel M., Noels A., Montalbán J., Miglio A., 2014, *A&A*, 569, A63

Gaia Collaboration et al., 2018, *A&A*, 616, A10

Gaia Collaboration et al., 2021a, *A&A*, 649, A1

Gaia Collaboration et al., 2021b, *A&A*, 650, C3

Gaia Collaboration et al., 2016a, *A&A*, 595, A2

Gaia Collaboration et al., 2016b, *A&A*, 595, A2

Gaia Collaboration et al., 2022, arXiv e-prints, arXiv:2206.05870

Gandhi P. et al., 2022, *MNRAS*, 510, 3885

Gautschy A., 1997, *A&A*, 320, 811

Gautschy A., Althaus L. G., Saio H., 2005, *A&A*, 438, 1013

Geier S., Heber U., 2012, *A&A*, 543, A149

Geier S., Østensen R. H., Nemeth P., Gentile Fusillo N. P., Gänsicke B. T., Telting J. H., Green E. M., Schaffenroth J., 2017, *A&A*, 600, A50

Geier S., Raddi R., Gentile Fusillo N. P., Marsh T. R., 2019, *A&A*, 621, A38

Gentile Fusillo N. P. et al., 2019, *MNRAS*, 482, 4570

Ghasemi H., Moravveji E., Aerts C., Safari H., Vučković M., 2017, *MNRAS*, 465, 1518

Girardi L., 2016, *ARA&A*, 54, 95

Green E. M. et al., 2003, *ApJ*, 583, L31

Green E. M. et al., 2011, *ApJ*, 734, 59

Green R. F., Schmidt M., Liebert J., 1986, *ApJS*, 61, 305

Greenstein J. L., Sargent A. I., 1974, *ApJS*, 28, 157

Greiss S., Gänsicke B. T., Hermes J. J., Steeghs D., Koester D., Ramsay G., Barclay T., Townsley D. M., 2014, *MNRAS*, 438, 3086

Haas M. R. et al., 2014, in American Astronomical Society Meeting Abstracts, Vol. 223, American Astronomical Society Meeting Abstracts #223, p. 228.01

- Hagen H.-J., Groote D., Engels D., Reimers D., 1995, *A&AS*, 111, 195
- Han Z., Podsiadlowski P., Maxted P. F. L., Marsh T. R., 2003, *MNRAS*, 341, 669
- Han Z., Podsiadlowski P., Maxted P. F. L., Marsh T. R., Ivanova N., 2002, *MNRAS*, 336, 449
- Handler G. et al., 1997, *MNRAS*, 286, 303
- Haro G., Luyten W. J., 1962, *Boletin de los Observatorios Tonantzintla y Tacubaya*, 3, 37
- Heber U., 1986, *A&A*, 155, 33
- Heber U., 2016, *PASP*, 128, 082001
- Heber U., Hunger K., Jonas G., Kudritzki R. P., 1984, *A&A*, 130, 119
- Hermes J. J. et al., 2014, *ApJ*, 789, 85
- Hermes J. J. et al., 2017a, *ApJS*, 232, 23
- Hermes J. J. et al., 2017b, *ApJS*, 232, 23
- Hermes J. J., Kawaler S. D., Bischoff-Kim A., Provencal J. L., Dunlap B. H., Clemens J. C., 2017c, *ApJ*, 835, 277
- Herwig F., 2001, *ApJ*, 554, L71
- Herwig F., 2005, *ARA&A*, 43, 435
- Herwig F., Bloeker T., Langer N., Driebe T., 1999, *A&A*, 349, L5
- Herwig F., Bloeker T., Schoenberner D., El Eid M., 1997, *A&A*, 324, L81
- Hill P. W., Hill S. R., 1966, *MNRAS*, 133, 205
- Holdsworth D. L., Østensen R. H., Smalley B., Telting J. H., 2017, *MNRAS*, 466, 5020
- Hong K., Lee J. W., Koo J.-R., Park J.-H., Rittipruk P., Kim H.-Y., Kanjanasakul C., Han C., 2021, *AJ*, 161, 137
- Howell S. B. et al., 2014, *PASP*, 126, 398
- Hubeny I., Lanz T., 2017, *arXiv e-prints*, arXiv:1706.01859
- Humason M. L., Zwicky F., 1947, *ApJ*, 105, 85
- Iben I., Jr., Kaler J. B., Truran J. W., Renzini A., 1983, *ApJ*, 264, 605
- Jaidee S., Lyngå G., 1969, *Arkiv for Astronomi*, 5, 345

-
- Jenkins J. M. et al., 2016, in Society of Photo-Optical Instrumentation Engineers (SPIE) Conference Series, Vol. 9913, Chiozzi G., Guzman J. C., eds, Software and Cyberinfrastructure for Astronomy IV, p. 99133E
- Jones M. I., Jenkins J. S., Rojo P., Melo C. H. F., 2011, *A&A*, 536, A71
- Kawaler S. D., 1987, in Philip A. G. D., Hayes D. S., Liebert J. W., eds, IAU Colloq. 95: Second Conference on Faint Blue Stars, p. 297
- Kawaler S. D., 1988a, in IAU Symposium, Vol. 123, Christensen-Dalsgaard J., Frandsen S., eds, *Advances in Helio- and Asteroseismology*, p. 329
- Kawaler S. D., 1988b, in IAU Symposium, Vol. 123, Christensen-Dalsgaard J., Frandsen S., eds, *Advances in Helio- and Asteroseismology*, p. 329
- Kawaler S. D., Bradley P. A., 1994, *ApJ*, 427, 415
- Kawaler S. D. et al., 1995, *ApJ*, 450, 350
- Kawaler S. D. et al., 2010, *MNRAS*, 409, 1487
- Kawka A., Vennes S., O'Toole S., Németh P., Burton D., Kotze E., Buckley D. A. H., 2015, *MNRAS*, 450, 3514
- Kepler S. O., 1993, *Baltic Astronomy*, 2, 515
- Kepler S. O., Fraga L., Winget D. E., Bell K., Córscico A. H., Werner K., 2014, *Monthly Notices of the Royal Astronomical Society*, 442, 2278
- Kepler S. O. et al., 2019a, *MNRAS*, 486, 2169
- Kepler S. O. et al., 2019b, *MNRAS*, 486, 2169
- Kern J. W., Reed M. D., Baran A. S., Telting J. H., Østensen R. H., 2018, *MNRAS*, 474, 4709
- Ketzer L., Reed M. D., Baran A. S., Németh P., Telting J. H., Østensen R. H., Jeffery C. S., 2017, *MNRAS*, 467, 461
- Kilkenny D., Heber U., Drilling J. S., 1988a, *South African Astronomical Observatory Circular*, 12, 1
- Kilkenny D., Heber U., Drilling J. S., 1988b, *South African Astronomical Observatory Circular*, 12, 1
- Kilkenny D., Hill P. W., 1975, *MNRAS*, 173, 625
- Kilkenny D., Hill P. W., Brown A., 1977, *Monthly Notices of the Royal Astronomical Society*, 178, 123

- Kilkenny D., Koen C., O'Donoghue D., Stobie R. S., 1997, *MNRAS*, 285, 640
- Kilkenny D., Luvhimbi E., O'Donoghue D., Stobie R. S., Koen C., Chen A., 1995, *MNRAS*, 276, 906
- Kilkenny D., Worters H. L., O'Donoghue D., Koen C., Koen T., Hambly N., MacGillivray H., Stobie R. S., 2016, *MNRAS*, 459, 4343
- Kippenhahn R., Weigert A., Weiss A., 2013, *Stellar Structure and Evolution*
- Koen C., Green E. M., 2010, *MNRAS*, 406, 2701
- Koen C., Laney D., 2000, *MNRAS*, 311, 636
- Koester D., Kepler S. O., 2015, *A&A*, 583, A86
- Krziesinski J., Balona L. A., 2022, arXiv e-prints, arXiv:2204.01604
- Kupfer T. et al., 2015, *A&A*, 576, A44
- Kurtz D., 2022, arXiv e-prints, arXiv:2201.11629
- Lallement R. et al., 2018, *A&A*, 616, A132
- Lallement R., Vergely J. L., Valette B., Puspitarini L., Eyer L., Casagrande L., 2014, *A&A*, 561, A91
- Lamontagne R., Demers S., Wesemael F., Fontaine G., Irwin M. J., 2000, *AJ*, 119, 241
- Lei Z., Zhao J., Németh P., Zhao G., 2018, *ApJ*, 868, 70
- Lei Z., Zhao J., Nemeth P., Zhao G., 2019, *VizieR Online Data Catalog*, J/ApJ/868/70
- Lenz P., Breger M., 2005, *Communications in Asteroseismology*, 146, 53
- Lightkurve Collaboration et al., 2018, *Lightkurve: Kepler and TESS time series analysis in Python*
- Lindegren L. et al., 2018a, *A&A*, 616, A2
- Lindegren L. et al., 2018b, *A&A*, 616, A2
- Lutz R., Schuh S., Silvotti R., Kruspe R., Dreizler S., 2008, *Communications in Asteroseismology*, 157, 185
- Luyten W. J., 1953, *AJ*, 58, 75
- Lynas-Gray A. E., 2021, *Frontiers in Astronomy and Space Sciences*, 8, 19
- Magee H. R. M. et al., 1998, *A&A*, 338, 85

-
- Massarotti A., Latham D. W., Stefanik R. P., Fogel J., 2008, *AJ*, 135, 209
- Masseron T., Hawkins K., 2017, *A&A*, 597, L3
- Mathys G., Hubrig S., Mason E., Michaud G., Schöller M., Wesemael F., 2012, *Astronomische Nachrichten*, 333, 30
- Maxted P. F. L., Heber U., Marsh T. R., North R. C., 2001, *MNRAS*, 326, 1391
- McGraw J. T., Starrfield S. G., Liebert J., Green R., 1979, in van Horn H. M., Weidemann V., Savedoff M. P., eds, *IAU Colloq. 53: White Dwarfs and Variable Degenerate Stars*, p. 377
- Mickaelian A. M. et al., 2007, *A&A*, 464, 1177
- Miller Bertolami M. M., 2016, *A&A*, 588, A25
- Miller Bertolami M. M., Althaus L. G., 2006, *A&A*, 454, 845
- Miller Bertolami M. M., Althaus L. G., 2007a, *A&A*, 470, 675
- Miller Bertolami M. M., Althaus L. G., 2007b, *MNRAS*, 380, 763
- Miller Bertolami M. M., Althaus L. G., Serenelli A. M., Panei J. A., 2006, *A&A*, 449, 313
- Miller Bertolami M. M., Althaus L. G., Unglaub K., Weiss A., 2008, *A&A*, 491, 253
- Miller Bertolami M. M., Battich T., Córscico A. H., Althaus L. G., Wachlin F. C., 2022, *MNRAS*, 511, L60
- Miller Bertolami M. M., Córscico A. H., Althaus L. G., 2012, in *Astronomical Society of the Pacific Conference Series*, Vol. 452, Kilkenny D., Jeffery C. S., Koen C., eds, *Fifth Meeting on Hot Subdwarf Stars and Related Objects*, p. 175
- Moehler S., Landsman W. B., Lanz T., Miller Bertolami M. M., 2019, *A&A*, 627, A34
- Molina F., Vos J., Németh P., Østensen R., Vučković M., Tkachenko A., van Winckel H., 2021, *arXiv e-prints*, arXiv:2110.14339
- Murakami H. et al., 2007, *PASJ*, 59, S369
- Napiwotzki R., Karl C. A., Lisker T., Heber U., Christlieb N., Reimers D., Nelemans G., Heisterkamp D., 2004, *Ap&SS*, 291, 321
- Nather R. E., Winget D. E., Clemens J. C., Hansen C. J., Hine B. P., 1990, *ApJ*, 361, 309
- Németh P., Kawka A., Vennes S., 2012, *MNRAS*, 427, 2180
- Németh P., Vos J., Molina F., Bastian A., 2021, *A&A*, 653, A3

- Neugebauer G. et al., 1984, *ApJ*, 278, L1
- Newell E. B., 1973, *ApJS*, 26, 37
- O'Donoghue D., 1994a, *MNRAS*, 270, 222
- O'Donoghue D., 1994b, *MNRAS*, 270, 222
- Oreiro R., Pérez Hernández F., Ulla A., Garrido R., Østensen R., MacDonald J., 2005, *A&A*, 438, 257
- Østensen R. H., 2006, *Baltic Astronomy*, 15, 85
- Østensen R. H., 2010, *Astronomische Nachrichten*, 331, 1026
- Østensen R. H., Bloemen S., Vučković M., Aerts C., Oreiro R., Kinemuchi K., Still M., Koester D., 2011a, *ApJ*, 736, L39
- Østensen R. H. et al., 2020, *MNRAS*, 499, 3738
- Østensen R. H. et al., 2011b, *MNRAS*, 414, 2860
- Østensen R. H. et al., 2010, *MNRAS*, 409, 1470
- Østensen R. H., Telting J. H., Reed M. D., Baran A. S., Nemeth P., Kiaeerad F., 2014, *A&A*, 569, A15
- Østensen R. H., Van Winckel H., 2012, in *Astronomical Society of the Pacific Conference Series*, Vol. 452, Kilkenny D., Jeffery C. S., Koen C., eds, *Fifth Meeting on Hot Subdwarf Stars and Related Objects*, p. 163
- Ostrowski J., Baran A. S., Sanjayan S., Sahoo S. K., 2021, *MNRAS*, 503, 4646
- Otani T. et al., 2021, arXiv e-prints, arXiv:2109.05394
- Pablo H., Kawaler S. D., Green E. M., 2011, *ApJ*, 740, L47
- Paczynski B., 1976, in *IAU Symposium*, Vol. 73, Eggleton P., Mitton S., Whelan J., eds, *Structure and Evolution of Close Binary Systems*, p. 75
- Pelisoli I., Vos J., Geier S., Schaffenroth V., Baran A. S., 2020, *A&A*, 642, A180
- Politano M., Taam R. E., van der Sluys M., Willems B., 2008, *ApJ*, 687, L99
- Pych W., 2004, *PASP*, 116, 148
- Queloz D. et al., 2001, *The Messenger*, 105, 1
- Quirion P. O., Fontaine G., Brassard P., 2007, *ApJS*, 171, 219

-
- Raghavan D. et al., 2010, *ApJS*, 190, 1
- Reed M. D., Baran A., Østensen R. H., Telting J., O'Toole S. J., 2012, *MNRAS*, 427, 1245
- Reed M. D. et al., 2011, *MNRAS*, 414, 2885
- Reed M. D. et al., 2016, *MNRAS*, 458, 1417
- Reed M. D. et al., 2018, *Open Astronomy*, 27, 157
- Reed M. D., Foster H., Telting J. H., Østensen R. H., Farris L. H., Oreiro R., Baran A. S., 2014, *MNRAS*, 440, 3809
- Reed M. D. et al., 2020a, *MNRAS*, 493, 5162
- Reed M. D. et al., 2019, *MNRAS*, 483, 2282
- Reed M. D., Terndrup D. M., Eggen J. R., Unterborn C. T., 2007, *Communications in Asteroseismology*, 150, 269
- Reed M. D., Yeager M., Vos J., Telting J. H., Østensen R. H., Slayton A., Baran A. S., Jeffery C. S., 2020b, *MNRAS*, 492, 5202
- Reimers D., 1975, *Memoires of the Societe Royale des Sciences de Liege*, 8, 369
- Reindl N. et al., 2019, *MNRAS*, 482, L93
- Reindl N., Schaffenroth V., Filiz S., Geier S., Pelisoli I., Kepler S. O., 2021, *A&A*, 647, A184
- Ren J. J. et al., 2020, *ApJ*, 905, 38
- Ricker G. R. et al., 2014, *Society of Photo-Optical Instrumentation Engineers (SPIE) Conference Series*, Vol. 9143, *Transiting Exoplanet Survey Satellite (TESS)*. p. 914320
- Ricker G. R. et al., 2015a, *Journal of Astronomical Telescopes, Instruments, and Systems*, 1, 014003
- Ricker G. R. et al., 2015b, *Journal of Astronomical Telescopes, Instruments, and Systems*, 1, 014003
- Romero A. D. et al., 2022, *MNRAS*, 511, 1574
- Sahoo S. K. et al., 2020a, *MNRAS*, 495, 2844
- Sahoo S. K., Baran A. S., Sanjayan S., Ostrowski J., 2020b, *MNRAS*, 499, 5508
- Sahoo S. K., Baran A. S., Sanjayan S., Ostrowski J., 2020c, *MNRAS*, 499, 5508
- Saio H., 1996, in *Astronomical Society of the Pacific Conference Series*, Vol. 96, Jeffery C. S., Heber U., eds, *Hydrogen Deficient Stars*, p. 361

- Schaffenroth V. et al., 2019, *A&A*, 630, A80
- Schindler J.-T., Green E. M., Arnett W. D., 2015, *ApJ*, 806, 178
- Schlafly E. F., Finkbeiner D. P., 2011, *ApJ*, 737, 103
- Schoenberner D., 1979, *A&A*, 79, 108
- Schuh S., Huber J., Dreizler S., Heber U., O’Toole S. J., Green E. M., Fontaine G., 2006, *A&A*, 445, L31
- Schwarzschild K., 1906, *Astronomische Mitteilungen der Universitaets-Sternwarte zu Goettingen*, 13, 1
- Science Software Branch at STScI , 2012, PyRAF: Python alternative for IRAF
- Setiawan J., Pasquini L., da Silva L., Hatzes A. P., von der Luehe O., Girardi L., de Medeiros J. R., Guenther E., 2004, *A&A*, 421, 241
- Silvotti R. et al., 2019, *MNRAS*, 489, 4791
- Simpson G., Mayer-Hasselwander H., 1986, *A&A*, 162, 340
- Soker N., 1998, *AJ*, 116, 1308
- Soto M. G., Jones M. I., Jenkins J. S., 2021, *A&A*, 647, A157
- Sowicka P., Handler G., Jones D., van Wyk F., 2021a, arXiv e-prints, arXiv:2108.08167
- Sowicka P., Handler G., Jones D., van Wyk F., 2021b, *ApJ*, 918, L1
- Stanghellini L., Cox A. N., Starrfield S., 1991, *ApJ*, 383, 766
- Starrfield S., Cox A. N., Kidman R. B., Pesnell W. D., 1984, *ApJ*, 281, 800
- Starrfield S. G., Cox A. N., Hodson S. W., Pesnell W. D., 1983, *ApJ*, 268, L27
- Stassun K. G. et al., 2018, *AJ*, 156, 102
- Stobie R. S. et al., 1997, *MNRAS*, 287, 848
- Sweigart A. V., 1997, *ApJ*, 474, L23
- Tassoul M., 1980, *ApJS*, 43, 469
- Tassoul M., Fontaine G., Winget D. E., 1990, *ApJs*, 72, 335
- Taylor M. B., 2005, in *Astronomical Society of the Pacific Conference Series*, Vol. 347, Shopbell P., Britton M., Ebert R., eds, *Astronomical Data Analysis Software and Systems XIV*, p. 29

Telting J. H. et al., 2014, *A&A*, 570, A129

Telting J. H. et al., 2012, *A&A*, 544, A1

Udalski A. et al., 2016, *Acta*, 66, 433

Unglaub K., Bues I., 2000, *A&A*, 359, 1042

Unno W., Osaki Y., Ando H., Saio H., Shibahashi H., 1989, *Nonradial oscillations of stars*

Unno W., Osaki Y., Ando H., Shibahashi H., 1979, *Nonradial oscillations of stars*

Uzundag M., Baran A. S., Østensen R. H., Reed M. D., Telting J. H., Quick B. K., 2017, *MNRAS*, 472, 700

Uzundag M. et al., 2021, *A&A*, 655, A27

Van Grootel V., Charpinet S., Brassard P., Fontaine G., Green E. M., 2013, *A&A*, 553, A97

Van Grootel V. et al., 2021, *A&A*, 650, A205

Vos J., Bobrick A., Vučković M., 2020, *A&A*, 641, A163

Vos J., Østensen R. H., Marchant P., Van Winckel H., 2015, *A&A*, 579, A49

Vos J. et al., 2021, *A&A*, 655, A43

Vos J., Vučković M., Chen X., Han Z., Boudreaux T., Barlow B. N., Østensen R., Németh P., 2019, *MNRAS*, 482, 4592

Wang K., Zhang X., Dai M., 2020, *ApJ*, 888, 49

Webbink R. F., 1984, *ApJ*, 277, 355

Wegner G., 1980, *AJ*, 85, 538

Wegner G., Boley F. I., 1993, *AJ*, 105, 660

Wenger M. et al., 2000, *A&AS*, 143, 9

Werner K., Herwig F., 2006, *PASP*, 118, 183

Werner K., Rauch T., Kepler S. O., 2014, *A&A*, 564, A53

Werner K., Reindl N., Dorsch M., Geier S., Munari U., Raddi R., 2021, *arXiv e-prints*, arXiv:2111.13549

Werner K., Reindl N., Geier S., Pritzkeleit M., 2022, *MNRAS*, 511, L66

Winget D. E., Hansen C. J., van Horn H. M., 1983, *Nature*, 303, 781

APPENDIX A. RADIAL VELOCITY MEASUREMENTS

Winget D. E., Kepler S. O., 2008, *ARA&A*, 46, 157

Winget D. E. et al., 1991, *ApJ*, 378, 326

Wisotzki L., Koehler T., Groote D., Reimers D., 1996, *A&AS*, 115, 227

Wittenmyer R. A. et al., 2020, *MNRAS*, 491, 5248

Wittenmyer R. A., Endl M., Wang L., Johnson J. A., Tinney C. G., O'Toole S. J., 2011, *ApJ*, 743, 184

Wittenmyer R. A., Liu F., Wang L., Casagrande L., Johnson J. A., Tinney C. G., 2016, *AJ*, 152, 19

Wright E. L. et al., 2010, *AJ*, 140, 1868

Yilmaz M. et al., 2017, *A&A*, 608, A14

York D. G. et al., 2000, *AJ*, 120, 1579

Zhang X., Jeffery C. S., 2012, *MNRAS*, 419, 452

Zong W., Charpinet S., Vauclair G., 2016, *A&A*, 594, A46

Zong W., Charpinet S., Vauclair G., Giammichele N., Van Grootel V., 2016, *A&A*, 585, A22



Publication list

First author

- KIC10001893: a pulsating sdB star with multiple trapped modes
Uzundag, M., Baran, A. S., Østensen, R. H., et al. 2017, MNRAS, 472, 700
- Asteroseismic analysis of variable hot subdwarf stars observed with TESS: I. The mean g-mode period spacings in hot subdwarf B stars
Uzundag, Murat, Vuckovic Maja et al. 2021, 2021A&A...651.A121
- Pulsating hydrogen-deficient white dwarfs and pre-white dwarfs observed with TESS II. Discovery of two new GW Vir stars: TIC333432673 and TIC095332541
Uzundag, Murat, Córscico, A. H. et al. 2021, 2021A&A...655.A27
- Pulsating hydrogen-deficient white dwarfs and pre-white dwarfs observed with TESS – IV. Discovery of two new GW Vir stars: TIC 0403800675 and TIC 1989122424
Uzundag, Murat, Córscico, A. H. et al. 2022, 2022MNRAS.tmp..981U
- Volume limited sample of low mass red giant stars, the progenitors of hot subdwarf stars - I. Sample selection and binary classification method
Uzundag Murat, Jones I. Matias et al. 2022, Submitted to A&A

Second and third author

- High-degree gravity modes in the single sdB star HD 4539
Silvotti R., **Uzundag M.**, et al. 2019, MNRAS.489.4791S

- About the existence of warm H-rich pulsating white dwarfs
Althaus L., Corsico A., **Uzundag M.**, et al. 2020, A&A.633A.20A
- Pulsating hydrogen-deficient white dwarfs and pre-white dwarfs observed with TESS. I. Asteroseismology of the GW Vir stars RX J2117+3412, HS 2324+3944, NGC 6905, NGC 1501, NGC 2371, and K 1-16
Córscico, A. H.; **Uzundag, M.**, et al. 2021, 2021A&A...645A.117C
- Pulsating hydrogen-deficient white dwarfs and pre-white dwarfs observed with TESS: III. Asteroseismology of the DBV star GD 358
Córscico A., **Uzundag M.**, et al. 2021, 2021arXiv211115551C

Others

- TESS first look at evolved compact pulsators: Discovery and asteroseismic probing of the g-mode hot B subdwarf pulsator EC 21494-7018
Charpinet, S.; Brassard, P.; Fontaine, G.; (inc. **Uzundag, M.**) et al. 2019, A&A.632A.90C
- TESS first look at evolved compact pulsators: asteroseismology of the pulsating helium-atmosphere white dwarf TIC257459955
Bell, Keaton J.; Córscico, Alejandro H.; Bischoff-Kim, Agnès; (inc. **Uzundag, Murat**) et al. 2019, A&A.632A.42B
- TESS first look at evolved compact pulsators: Known ZZ Ceti stars of the southern ecliptic hemisphere as seen by TESS
Bognár, Zs.; Kawaler, S. D.; Bell, K. J.; (inc. **Uzundag, M.**) et al. 2020, A&A.638A.82B
- TESS observations of pulsating subdwarf B stars: extraordinarily short-period gravity modes in CD-28° 1974
Reed, M. D.; Shoaf, K. A.; Németh, P.; Vos, J.; **Uzundag, M.** et al. 2020, MNRAS.493.5162R
- Mode identification in three pulsating hot subdwarfs observed with TESS satellite
Sahoo, S. K.; Baran, A. S.; Heber, U.; (inc. **Uzundag, M.**) et al. 2020, MNRAS.495.2844S

-
- Looking into the cradle of the grave: J22564-5910, a young post-merger hot subdwarf?
Vos J; Pelisoli I.; Budaj J; (inc. **Uzundag, M.**), et al. 2021, 2021arXiv210603363V
 - Pulsating subdwarf B stars observed with K2 during Campaign 7 and an examination of seismic group-properties.
Reed, M. D.; Slayton, A.; (inc. **Uzundag, M.**) et al. 2021, 2021MNRAS.tmp.2194R
 - Orbital Characteristics of the AQ Col (EC 05217-3914) System
T. Otani, A. E. Lynas-Gray, D. Kilkenney, C. Koen, T. von Hippel, **Uzundag, M.**, M. Vuckovic, C. M. Pennock, R. Silvotti 2021, 2021arXiv210905394O
 - Discovery of 74 new bright ZZ Ceti stars in the first three years of *TESS*
Alejandra D. Romero, S. O. Kepler, Larissa Antunes Amaral, **Uzundag, Murat**, et al., 2022MNRAS.511.1574R

Conference proceedings

- Asteroseismic analysis of subdwarf B variable stars of KIC10001893 and EPIC220641886
Uzundag M., Vuckovic M., Silvotti R, Baran A., R.H. Ostensen, BAAA, Vol. 61A, 2019
- Asteroseismic analysis of subdwarf B variable stars: what we have learned from the recent space missions
Uzundag M., Vuckovic M., 2020BAAA..61C...78U

Posters

- Detection of trapped modes in the pulsating subdwarf B star KIC10001893 9-15 July 2017
8th Meeting on Hot Subdwarf Stars and Related Objects/Pedagogical University of Cracow, Poland
- The High-Degree Gravity (g)-modes Sequences in HD 4539
<https://doi.org/10.5281/zenodo.1761148> 2-7 Sep 2018
PHysics of Oscillating STars (PHOST) Oceanographic Observatory/France
- Volume limited sample of low mass red giant stars, the progenitors of hot subdwarf stars

APPENDIX B. PUBLICATION LIST

<https://k-poster.kuoni-congress.info/eas2020/poster/58f935ed-02ca-444f-aa30-ef859acbe899>

European Astronomical Society Annual Meeting 2020 29 Jun–3 Jul 2020

- Pulsating hydrogen-deficient white dwarfs and pre-white dwarfs observed with TESS: Discovery of two new GW Vir stars

https://zenodo.org/record/5122978#.YS_d2XWYXg4

TASOC

August 2 - 6, 2021

- Asteroseismology of hot subdwarf B stars observed with TESS: discovery of two new gravity mode pulsating stars

10TH MEETING ON HOT SUBDWARFS AND RELATED OBJECTS June 13 - 17, 2022